COLLEGES SCIENCES
BRETAGNE POUR L'INGENIEUR
LOIRE ET LE NUMERIQUE

IMT Atlantique
Bretagne-Pays de la Loire
École Mines-Télécom

THÈSE DE DOCTORAT DE

L'ÉCOLE NATIONALE SUPÉRIEURE MINES-TÉLÉCOM ATLANTIQUE BRETAGNE PAYS-DE-LA-LOIRE - IMT ATLANTIQUE

ÉCOLE DOCTORALE N° 648
Sciences pour l'Ingénieur et le Numérique
Spécialité : *Télécommunications*

Par
Anouar JERBI

Non-Coherent Detection of Continuous Phase Modulation for Low Earth Orbit Satellite IoT Communications Affected by Doppler Shift

Thèse présentée et soutenue à l'IMT Atlantique à Brest, le 14 mars 2023
Unité de recherche : Lab-STICC
Thèse N° : 2023IMTA0354

Rapporteurs avant soutenance :

Jérôme LE MASSON	Professeur, Institut d'Electronique et des Technologies du numérique
Jean-François DIOURIS	Professeur, Ecole polytechnique de l'université de Nantes

Composition du Jury :

Président :	Guillaume FERRÉ	Professeur, Université de Bordeaux
Examinateur :	Giulio COLAVOLPE	Professeur, Université de Parme
Rapporteurs :	Jérôme LE MASSON	Professeur, Institut d'Electronique et des Technologies du numérique
	Jean-François DIOURIS	Professeur, Ecole polytechnique de l'université de Nantes
Dir. de thèse :	Frédéric GUILLOUD	Professeur, IMT Atlantique
Co-dir. de thèse :	Karine AMIS	Professeur, IMT Atlantique
Encadrant :	Tarik BENADDI	Ingénieur R&D, Thales Alenia Space

ACKNOWLEDGEMENT

I would like to start by expressing my sincere gratitude to my supervisors in this PhD, Prof. Frédéric GUILLOUD and Prof. Karine AMIS. This work would not have been accomplished without their support. Their advice, guidance, comments, and criticisms have helped me improve on both professional and personal level and their kindness and patience during these last three years have made the work easier especially during tough moments. They have given me the ability to enrich my scientific background thanks to their profound knowledge and experience as well as their great insight. I consider myself lucky to have had the opportunity to work with them and it was a real pleasure sharing some unforgettable moments.

Special thanks also goes to my third supervisor, Tarik BENADDI that has accompanied me mostly in my first year. His welcoming me in Toulouse have without a doubt helped me starting my thesis and I really appreciate the discussions that we have had during our time together.

Moreover, I would also wish to thank Prof. Guillaume FERRÉ for being the president of my PhD jury, and also thank the rest of the committee members, Prof. Giulio COLAVOLPE, and also Prof. Jérôme LE MASSON, and Prof. Jean-François DIOURIS for taking time to review this manuscript. Special thanks to Prof. Giulio COLAVOLPE and Prof. Guillaume FERRÉ for their comments and feedback during our annual small committee meetings.

Many thanks to all my friends and colleagues who have helped creating a nice and enjoyable work environment all these years, in Brest and Toulouse, especially during the outbreak of the COVID-19 crisis in the beginning of my PhD. Their help, whether from near or far, has been essential in overcoming difficult situations.

Last but absolutely not least, a sincere acknowledgement goes to my parents for believing in me in the first place, for their encouragement, tenderness, kindness, patience in this journey and most importantly, for their unconditional love and support. Many thanks also goes to my brother and sisters for their support as well.

RÉSUMÉ EN FRANÇAIS

Motivations

L'internet des objets (IoT) est un concept dans lequel de nombreux objets sont dotés de capacités de transmissions ou de communications via une connexion au réseau internet. Desservies essentiellement par des réseaux terrestres, des applications IoT peuvent également concerner les opérateurs satellites, par exemple dans les zones peu couvertes, ce qui ouvre ainsi des problématiques intéressantes au niveau de la couche physique de ces objets communicants.
L'approche qui nous intéresse dans le but d'avoir une couverture globale du réseau IoT est le *Direct-to-Satellite* IoT [1]. Il s'agit d'une approche où aucune passerelle terrestre intermédiaire n'est requise, ce qui facilite et accélère le déploiement du réseau. Dans ce cadre, le satellite collecte directement les données des objets communicants et les traite. Il devrait également être capable de communiquer avec l'objet si une liaison descendante est envisagée. Cette approche pose certains problèmes en termes de couche physique. Le grand défi ici est de pouvoir créer une liaison de communication longue portée fiable ayant des ressources limitées à la fois dans le satellite et dans l'objet communicant tout en faisant face aux problèmes d'une liaison satellite. Cela peut être réalisé soit en révisant et en adaptant des technologies IoT existantes pour prendre en charge les communications directes avec un satellite, soit en fournissant de nouvelles couches MAC et physiques spécifiquement dédiées à cette application. Nous nous focalisons plutôt sur la deuxième approche.
Lors du choix d'une forme d'onde pour n'importe quelle application de communication sans fil, trois éléments majeurs doivent être étudiés ; performances, complexité et bande passante. En général, la forme d'onde choisie est celle qui offre le meilleur compromis entre ces trois éléments. Pour les applications de communication par satellites en orbites basses, plusieurs dégradations majeures affectant les performances doivent être prises en compte. Les instabilités de phase, le décalage Doppler élevé, les interférences dans un scénario multi-utilisateurs, les amplificateurs non linéaires généralement utilisés des deux côtés de la transmission, au niveau des objets communicants et à bord du satellite, etc.
En termes de complexité, il est important qu'elle soit la plus faible possible car dans l'application visée, les objets communicants utilisent de petites piles et le satellite n'est pas qu'un simple relais, mais au contraire, il effectue une partie du traitement et compte tenu des ressources limitées à bord, la complexité est une contrainte majeure. La bande passante dans l'application ciblée peut également être un problème. Que ce soit des bandes de fréquences sous licence ou non, la

bande passante disponible est limitée.
La modulation de phase continue (CPM) est une classe de modulation qui englobe plusieurs familles de formes d'onde de modulation de phase. Elle possède différents paramètres qui peuvent être ajustés pour répondre aux besoins de l'application. Les travaux de recherche portant sur la conception de formes d'onde CPM avec des systèmes de communication par satellites pour obtenir de bonnes performances du point de vue spectre et énergie ont montré des résultats prometteurs. Le problème de l'efficacité énergétique a été discuté dans [2] et [3]. Une étude sur la manière de choisir des schémas CPM spectralement efficaces a été présentée dans [4]. L'interférence du canal adjacent (ACI) a également été évaluée dans [5] et la possibilité d'utiliser des schémas de codage pour résoudre certains des problèmes mentionnés en utilisant la bande de fréquence Ka peut être trouvée dans [6]. Bien que les travaux cités ne s'appliquent peut-être pas spécifiquement à l'application Satellite IoT, ils fournissent cependant de bonnes bases fondatrices pour dériver des solutions adaptées à notre problème.
Certains standards basés sur les communications par satellite utilisent déjà un format CPM. On peut citer le standard de diffusion vidéo numérique DVB-RCS2 [7] qui a été éditée par le consortium international *DVB project*. Plus récemment, un schéma GFSK a également été adopté par Semtech comme candidat pour la technique *Long Range Frequency Hopping Spread Spectrum* (LR-FHSS) [8].
Compte tenu de tous ces détails, nous avons choisi de nous concentrer sur la forme d'onde CPM dans ce travail pour exploiter son potentiel dans l'application considérée et nous avons particulièrement étudié sa réception du point de vue du satellite (lien montant).

Objectifs

Dans cette thèse, nous considérons un objet communicant transmettant vers le satellite. Le satellite doit alors décoder les informations et ne se contente pas d'agir comme un système de relais. La puissance disponible limitée à bord fait de la complexité un problème important. Nous ne nous concentrons pas non plus sur les technologies LPWAN existantes. Dans ce travail, nous exploitons le potentiel de la modulation de phase continue (CPM) qui est relativement nouveau pour ce type d'applications. Le problème auquel nous nous attaquons est l'effet Doppler très présent dans la liaison satellite. En effet, le décalage Doppler affecte fortement la détection et nous présentons plusieurs détecteurs avec différents niveaux de complexité pour pallier ce problème. Le décalage de phase est également pris en compte dans le modèle de transmission. Cela est dû au retard temporel de la propagation du signal et à la faible précision des oscillateurs locaux utilisés dans la transmission des objets pour permettre des terminaux à faible coût. Un autre aspect sur lequel nous nous sommes concentrés est que la détection doit se faire de manière aveugle par rapport au Doppler chaque fois que cela est possible car dans les communications

IoT à trame courte, nous ne pouvons pas autoriser de longues séquences pilotes (le cas échéant) pour préserver la puissance des terminaux et d'utiliser efficacement la bande de fréquence.

Contributions

Les contributions de la thèse sont les suivantes :

- Tout d'abord, nous introduisons une nouvelle détection non cohérente CPM basée sur l'application directe du principe du maximum de vraisemblance généralisé avec l'insertion du principe d'estimation Doppler aveugle de [9] dans l'algorithme proposé également comme dans la détection non cohérente CPM de [10]. Partant de cela, nous dérivons deux détecteurs avec différents niveaux de complexité.
- Deuxièmement, nous présentons l'extension théorique de l'algorithme de détection différentielle CPM usuel pour considérer un retard supérieur à une période de symbole (y compris la description du treillis de phase et la dérivation des équations de la branche et de la métrique cumulée)
- Troisièmement, nous donnons une méthode pour déterminer systématiquement une valeur de retard optimisée basée sur l'application du critère de distance Euclidienne minimale entre deux signaux différentiels CPM et nous présentons les valeurs de retard optimisées pour différents formats CPM (indice de modulation , longueur d'impulsion de fréquence, type d'impulsion de fréquence).
- Quatrièmement, nous comparons le détecteur différentiel à retard optimisé en présence de décalages Doppler avec les premiers détecteurs introduits en termes de performances/complexité et discutons de leurs avantages et inconvénients.

Détection non cohérente des modulations CPM avec estimation aveugle du Doppler

La contrainte de puissance dans le cadre de l'Internet des Objets par Satellite (Satellite IoT) impose l'utilisation de trames courtes. Cela peut être un problème pour la détection où le signal est fortement affecté par la présence de Doppler puisque les séquences pilotes dans la trame peuvent être trop courtes pour aider au problème d'estimation de fréquence ou peuvent même être omises pour plus d'efficacité spectrale. Notre objectif est de concevoir un détecteur CPM capable de supporter le fort décalage Doppler rencontré en aveugle. Nous devons également garder à l'esprit les incertitudes de phase à la réception. Par conséquent, nous partons du critère de détection non cohérente appliqué au CPM et nous l'employons avec le principe de vraisemblance généralisée pour dériver deux détecteurs possibles ; le premier utilise la décomposition linéaire du CPM et le second utilise l'expression exacte du signal.

Strategie de détection

Nous commençons par considérer un décalage Doppler constant. Cette hypothèse sera ensuite assouplie. En présence d'un décalage Doppler constant f_D, le signal reçu se traduit par :

$$r(t) = s(t, \mathbf{a}) e^{j(2\pi f_D t + \psi)} + n(t) \tag{1}$$

Partant du critère de détection de séquences non cohérente, la stratégie de détection proposée est alors basée sur le maximum de vraisemblance généralisé [11] que nous allons rappeler maintenant. Soit T_0 l'intervalle d'observation du signal $r(t)$ et soit $\mathcal{A}$ l'ensemble des séquences de symboles possibles, $\mathcal{F}$ l'intervalle de variation de f_D et I_0 la fonction de Bessel modifiée du premier ordre. La méthode du maximum de vraisemblance généralisée [11] est utilisée pour une estimation de décalage Doppler aveugle en conjonction avec la détection de symboles et consiste à maximiser la fonction de coût suivante :

$$\Gamma(\tilde{\mathbf{a}}, \widetilde{f_D}) = \log \mathrm{I}_0 \left(\frac{1}{N_0} \left| \int_{T_0} r(t, \mathbf{a}) s^*(t, \tilde{\mathbf{a}}) e^{-j2\pi \widetilde{f_D} t} dt \right| \right) - \frac{1}{2N_0} \int_{T_0} |s(t, \tilde{\mathbf{a}})|^2 dt \tag{2}$$

sur $\mathcal{A} \times \mathcal{F}$.
Cela équivaut selon cette méthode à trouver la séquence $\tilde{\mathbf{a}}$ qui maximise Γ par rapport à $\tilde{\mathbf{a}}$ et une estimation de f_D basée sur sur $\tilde{\mathbf{a}}$. Mathématiquement parlant, on cherche la suite $\tilde{\mathbf{a}}$ vérifiant :

$$\max_{\tilde{\mathbf{a}} \in \mathcal{A}} \Gamma(\tilde{\mathbf{a}}, \widehat{f}_D(\tilde{\mathbf{a}})) \tag{3}$$

avec

$$\widehat{f}_D(\tilde{\mathbf{a}}) = \arg \max_{\widetilde{f_D} \in \mathcal{F}} \left| \int_{T_0} r(t) s^*(t, \tilde{\mathbf{a}}) e^{-j2\pi \widetilde{f_D} t} dt \right|. \tag{4}$$

Dans ce qui suit, nous appliquons le critère (3) selon deux algorithmes alternatifs. La première (notée A), basée sur une décomposition linéaire du CPM, est une combinaison des méthodes décrites dans [10] (notée algorithme NSD) et [9]. Le second (appelé B) est un algorithme sous-optimal pour dériver le critère directement à partir de l'équation du signal CPM.

Détecteur A

Ce récepteur combine l'algorithme de détection CPM non cohérent [10] avec l'algorithme d'estimation Doppler et de détection conjointe appliqué à une modulation linéaire [9]. Pour cela, nous considérons la décomposition linéaire de la modulation CPM où nous considérons également K_c le nombre de composantes principales uniquement.
Le récepteur consiste en une cascade d'un banc de filtres où les filtres sont adaptés à $h_k(t)$, suivi d'un échantillonneur à la période T_e et d'un filtre de blanchiment. T_e doit être suffisamment petit pour supposer que les échantillons sont une statistique suffisante pour la détection [12].

Cependant, pour un décalage de fréquence modéré ($f_D T_s \ll 1$), $T_e = T_s$ est suffisamment petit. Les sorties de l'échantillonneur sont données par :

$$x_{k,n} = r(t, \mathbf{a}) \otimes h_k(-t)|_{t=nT_s} \simeq s_{k,n} e^{j(2\pi f_D n T_s + \phi)} + \eta_{k,n}$$

où

$$s_{k,n} = \sum_{m=0}^{K_c-1} \sum_i \alpha_{m,i} p_{m,k}((n-i)T_s), \tag{5}$$

avec $p_{m,k}(t) = h_m(t) \otimes h_k(-t)$ et $\eta_{k,n} = \eta(t) \otimes h_k(-t)|_{t=nT_s}$. Nous introduisons la notation $\mathbf{x}_n = (x_{0,n}, x_{1,n}, ..., x_{K-1,n})^T$ et définissons $\mathbf{s}_n$, $\boldsymbol{\alpha}_n$ et $\boldsymbol{\eta}_n$ de même. Nous utiliserons également les matrices de réponse impulsionnelle discrète $\mathbf{P}_n = [p_{i,j}(nT)]$ pour $i, j = 0, 1, ..., K-1$. Avec ces notations, le vecteur d'observation s'écrit :

$$\mathbf{x}_n \simeq e^{j(2\pi f_D n T + \phi)} \sum_{l=-L_w}^{L_w} \mathbf{P}_l^T \boldsymbol{\alpha}_{n-l} + \boldsymbol{\eta}_n, \tag{6}$$

où L_w est un paramètre qui dépend de L.
Comme les échantillons de bruit $\eta_{k,n}$ sont corrélés, un filtre de blanchiment multidimensionnel (WMF) est implémenté [10]. Il est spécifié par la séquence de matrices $\{\mathbf{W}_l\}_{0 \le l \le L_w}$. Le vecteur d'observation de sortie WMF, noté $\mathbf{z}_n$, est donné par :

$$\begin{aligned} \mathbf{z}_n &= \sum_{l=0}^{L_w} \mathbf{W}_l \mathbf{x}_{n-l} \\ &= e^{j(2\pi f_D n T_s + \phi)} \sum_{l=0}^{L_w} \mathbf{W}_l \mathbf{s}_{n-l} e^{-j2\pi l f_D T_s} + \mathbf{w}_n, \end{aligned} \tag{7}$$

où $\mathbf{w}_n = \sum_{l=0}^{L_w} \mathbf{W}_l \boldsymbol{\eta}_{n-l}$.
Pour en revenir au critère de détection, nous appliquons deux approximations. La première consiste à considérer $\log I_0(x) \simeq x$. La seconde dépend du contexte : on suppose que $f_D T_s$ est petit et que $e^{-j2\pi l f_D T_s} \simeq 1$ dans l'expression (7) de $\mathbf{z}_n$. Étant donné une séquence $\tilde{\mathbf{a}}$ de symboles dans $\mathcal{A}$, on définit $\tilde{\mathbf{s}}_n$ avec (5) et enfin $\tilde{\mathbf{y}}_n = \sum_{l=0}^{L_w} \mathbf{W}_l \tilde{\mathbf{s}}_{n-l}$ qui sont les échantillons qui seront utilisés pour l'estimation de la fréquence ainsi que pour la détection.
La fonction de vraisemblance calculée dans l'algorithme conjoint de détection de symboles et d'estimation Doppler est donc donnée par :

$$\Gamma_N(\tilde{\mathbf{a}}, \widehat{f}_D(\tilde{\mathbf{a}})) = \left| \sum_{k=0}^{K_c-1} \sum_{n=0}^{N-1} z_{k,n} \tilde{y}_{k,n}^* e^{-j2\pi n \widehat{f}_D(\tilde{\mathbf{a}}) T_s} \right| - \frac{1}{2} \sum_{k=0}^{K_c-1} \sum_{n=0}^{N-1} |\tilde{y}_{k,n}|^2. \tag{8}$$

Si la deuxième approximation ne tient pas, les échantillons $\tilde{\mathbf{y}}_n$ ne peuvent pas être définis correctement et par conséquent, la détection à l'aide de ce modèle ne peut pas être reportée. Une solution consiste à utiliser le suréchantillonnage, mais nous en discuterons dans le prochain détecteur.

Maximiser (8) implique une complexité prohibitive en pratique. Nous adaptons la procédure utilisée dans [9] pour traiter les modulations linéaires. Un algorithme de Viterbi est appliqué associé à un fenêtrage de taille N_v pour la détection de symboles, un fenêtrage de taille $N_D \geq N_v$ pour l'estimation aveugle du décalage Doppler et une approximation de $\Gamma_N(\tilde{\mathbf{a}}, \widehat{f}_D(\tilde{\mathbf{a}})$ par $\Delta_N(\tilde{\mathbf{a}})$ qui est calculé de manière itérative façon comme suit :

$$\Delta_n(\tilde{\mathbf{a}}_n) = \Delta_{n-1}(\tilde{\mathbf{a}}_{n-1})) + \lambda_n(\tilde{\mathbf{a}}_\mathbf{n}) \tag{9}$$

avec la métrique de branche étant

$$\begin{aligned}
\lambda_n(\tilde{\mathbf{a}}_\mathbf{n}) &= \left| \sum_{k=0}^{K_c-1} \sum_{i=0}^{N_v-1} z_{k,n-i} \tilde{y}^*_{k,n-i} e^{-j2\pi(n-i)\widehat{f}_D(\tilde{\mathbf{a}}^n_{n-N_D}))T_s} \right| \\
&- \left| \sum_{k=0}^{K_c-1} \sum_{i=1}^{N_v-1} z_{k,n-i} \tilde{y}^*_{k,n-i} e^{-j2\pi(n-i)\widehat{f}_D(\tilde{\mathbf{a}}^n_{n-N_D}))T_s} \right| \\
&- \left| \sum_{k=0}^{K_c-1} \tilde{y}_{k,n} \right|^2 .
\end{aligned}$$

L'état à l'instant $n-1$ est défini par le vecteur $\left(\tilde{\mathbf{y}}^T_{n-1} \quad \dots \quad \tilde{\mathbf{y}}^T_{n-N_v+1}\right)^T$, ce qui implique un total de $S = M^{N_v+L_w-1}$ états. Comme dans [9], une approche *per-survivor processing* (PSP) permet d'estimer $\widehat{f}_D(\tilde{\mathbf{a}}^n_{n-N_D})$ basé sur $\tilde{a}_n$ et la séquence partielle $\tilde{\mathbf{a}}^{n-1}_{n-N_D} = (\tilde{a}_{n-1} \ \dots \ \tilde{a}_{n-N_D})$ associé au chemin survivant au niveau de l'état à l'instant $n-1$.

Le calcul de $\lambda_n(\tilde{\mathbf{a}}_\mathbf{n})$ implique qu'il faut attendre le $N_v^{\text{ème}}$ symbole pour lancer le décodage. Une question peut être posée ici concernant la phase d'initiation de l'estimation du décalage Doppler dans le cas $N_D > N_v$. Ici, la solution que nous avons utilisée est de faire l'estimation du décalage Doppler sur une fenêtre de longueur N_v (puisque les symboles sur cette fenêtre sont les seuls symboles disponibles jusqu'à présent) puis nous étendons la longueur de cette fenêtre à $N_v + 1$ basé sur le premier symbole décidé. On fait ensuite l'estimation sur une fenêtre plus étendue et on continue donc la même étape jusqu'à atteindre la longueur désirée N_D.

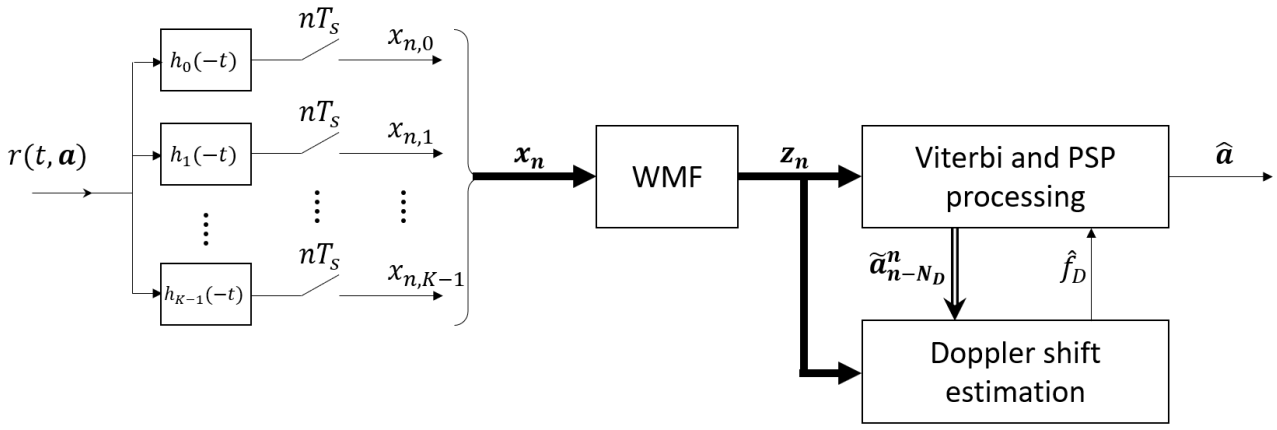

Figure 1 – Architecture du détecteur A

Pour résumer, le détecteur A est constitué d'un banc de filtres adaptés aux composantes principales de la décomposition linéaire du signal, suivi d'un échantillonneur au débit symbole puis d'un filtre blanchissant multidimensionnel dont les sorties sont utilisées comme entrée du processeur de Viterbi comme représenté sur la Figure 1.

Détecteur B

Le but de ce récepteur est de continuer à fonctionner à des taux de décalage de fréquence beaucoup plus élevés car l'application que nous visons pourrait présenter une plage Doppler substantielle. En considérant l'enveloppe constante de la forme d'onde CPM, la fonction de vraisemblance (3) devient :

$$\Lambda(\tilde{\mathbf{a}}) = \Gamma(\tilde{\mathbf{a}}, \widehat{f}_D(\tilde{\mathbf{a}})) = \left| \int_{T_0} r(t, \mathbf{a}) s^*(t, \tilde{\mathbf{a}}) e^{-j2\pi \widehat{f}_D(\tilde{\mathbf{a}})t} dt \right|$$

Soit $t_k = kT_s$ et soit $v_n(t, \tilde{\mathbf{a}}) = r(t, \mathbf{a}) e^{-j2\pi \widehat{f}_D(\tilde{\mathbf{a}}^n_{n-N_D})t}$. Pour réduire la complexité, nous appliquons l'approximation itérative de $\Lambda(\tilde{\mathbf{a}})$ avec les mêmes principes de fenêtrage et de définition des métriques cumulatives et de branche :

$$\lambda_n(\tilde{\mathbf{a}}) = \Gamma_n(\tilde{\mathbf{a}}) - \left| \int_{(n-N_v)T_s}^{(n-1)T_s} v_n(t, \mathbf{a}) s^*(t, \tilde{\mathbf{a}}) dt \right| \tag{10}$$

où $\Gamma_n(\tilde{\mathbf{a}}) = \left| \int_{t_{n-N_v}}^{t_n} v_n(t, \tilde{\mathbf{a}}) s^*(t, \tilde{\mathbf{a}}) dt \right|$. Avec le même raisonnement, la recherche de la suite maximisant la fonction de vraisemblance (2) se fait à l'aide d'un algorithme de Viterbi exécuté sur un treillis dont les états au temps n correspondent à toutes les réalisations possibles de $s(t, \tilde{\mathbf{a}}^n_{n-N_v+1})$. L'estimation $\widehat{f}_D(\tilde{\mathbf{a}}^n_{n-N_D})$ se fait comme pour le récepteur A en utilisant l'approche PSP sur une

fenêtre de longueur N_D.
Le développement du premier terme de l'équation (10) conduit à :

$$\Gamma_n(\tilde{\mathbf{a}}) = \sqrt{\frac{2E_s}{T_s}} \left| \sum_{m=0}^{N_v-1} \int_{t_{n-m-1}}^{t_{n-m}} v_n(t, \tilde{\mathbf{a}}) e^{-j\theta(t,\tilde{\mathbf{a}})} dt \right|. \tag{11}$$

Le terme dépendant de $\theta(t, \tilde{\mathbf{a}})$ dans l'intervalle $[t_{n-m-1}, t_{n-m}]$ peut être simplifié :

$$\theta(t, \tilde{\mathbf{a}}) = 2\pi h \sum_{u=0}^{n-m-1} \tilde{a}_u q(t - uT_s) = \Theta(t, \tilde{\mathbf{a}}) + \pi h \sum_{u=0}^{n-m-L-1} \tilde{a}_u \tag{12}$$

avec

$$\Theta(t, \tilde{\mathbf{a}}) = 2\pi h \sum_{u=n-m-L}^{n-m-1} \tilde{a}_u q(t - uT_s) \tag{13}$$

En remplaçant (12) dans (11), et après quelques calculs simples, on obtient :

$$\Gamma_n(\tilde{\mathbf{a}}) = \sqrt{\frac{2E_s}{T_s}} \left| \sum_{m=0}^{N_v-1} e^{-j\pi h \sum_{u=n-N_v-L+2}^{n-m-L-1} \tilde{a}_u} I_m(\tilde{\mathbf{a}}) \right| \tag{14}$$

avec

$$I_m(\tilde{\mathbf{a}}) = \int_{t_{n-m-1}}^{t_{n-m}} v_n(t, \tilde{\mathbf{a}}) e^{-j\Theta(t,\tilde{\mathbf{a}})} dt \tag{15}$$

On en déduit que le calcul de $\lambda_n(\tilde{\mathbf{a}})$ ne dépend que de $[\tilde{a}_{n-1}, .., \tilde{a}_{n-N_v-L+2}]$. L'algorithme de Viterbi s'applique donc à un treillis à $S = M^{N_v+L-2}$ états (nombre de réalisations de $[\tilde{a}_{n-1}, .., \tilde{a}_{n-N_v-L+2}]$).

Ainsi, le détecteur B est une série d'intégrateurs suivis de détecteurs d'enveloppe qui calcu-

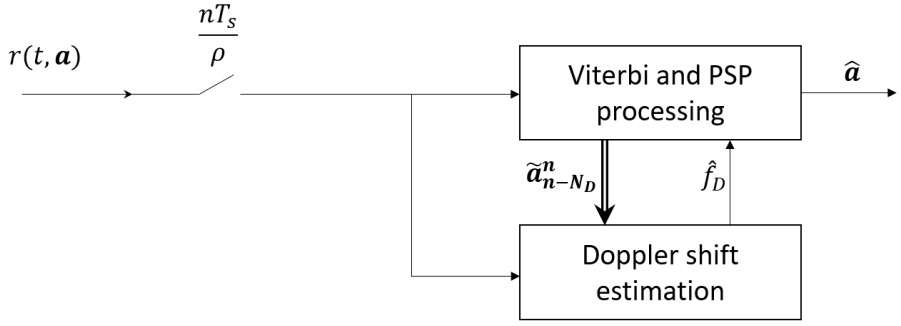

Figure 2 – Architecture du détecteur B

lent les grandeurs que nous allons utiliser en entrée du processeur de Viterbi. L'architecture du détecteur B est représentée sur la Figure 2.

Nous voulons par la suite comparer les performances des détecteurs A et B dans différents ordres du Doppler. On commence par considérer le schéma 3RC avec $h = 0.75$ sur la Figure 3.

Dans ce schéma, nous avons approximé le signal reçu dans le détecteur A uniquement par ses premières composantes principales résultant de sa décomposition linéaire avec $L_w = 2$. Pour un petit décalage Doppler $f_D T_s = 0,075$, les détecteurs A et B fonctionnent presque de la même manière avec une perte de 1 à 1,5 dB par rapport aux performances NSD qui correspondent aux performances sans aucun décalage Doppler. Lorsque le décalage Doppler est augmenté à $f_D T_s = 0,125$, les performances du détecteur A sont dégradées et un écart de 3 dB par rapport au NSD est observé à un BER de 10^{-3}.

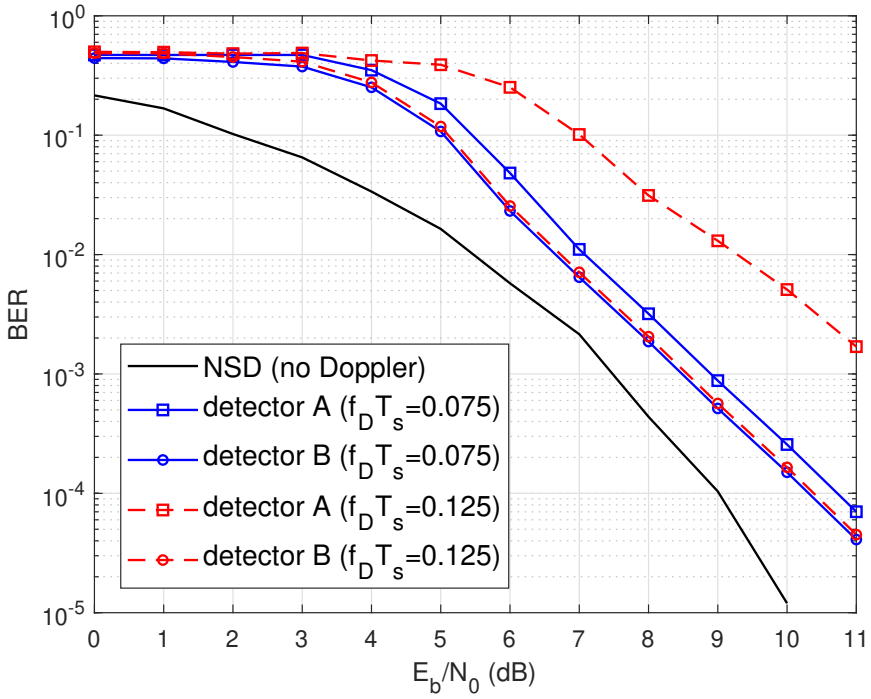

Figure 3 – Comparaison du TER entre les détecteurs A ($\rho = 1$, $N_{\text{FFT}} = 32$) et B ($\rho = 8$, $N_{\text{FFT}} = 256$) pour 3RC avec $h = 0.75$, $N_v = 5$ et $N_D = 8$

Bien qu'initialement nous ayons fait l'hypothèse que le décalage Doppler est constant, cela pourrait être relâché pour les deux détecteurs A et B puisque l'utilisation d'une fenêtre glissante pour estimer ce dernier tout au long du treillis permet aux récepteurs de suivre sa variation à condition qu'il varie peu sur cette fenêtre, condition bien remplie étant donné, non seulement le profil du Doppler, mais aussi le fait que la taille de la fenêtre glissante est relativement petite (8 symboles) selon les résultats des simulations.
Pour évaluer les performances des détecteurs A et B dans le cas du Doppler variable, on considère le format 4RC avec $h = \frac{2}{3}$. La taille des fenêtres est conservée avec $N_v = 5$ et $N_D = 8$. Dans la simulation, nous avons considéré $f_D T_s = 0,05$ tout en ayant également un taux Doppler $f_R = 250$ Hz/s qui est à nouveau le taux théorique maximum rencontré dans notre application.

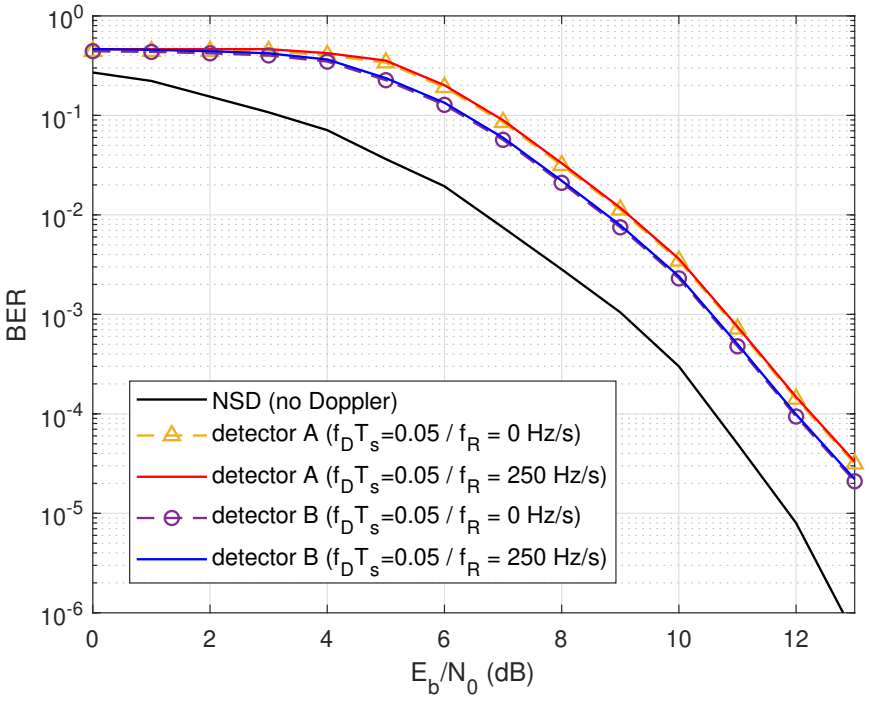

Figure 4 – Comparaison du TER entre les détecteurs A et B pour 4RC avec $h = \frac{2}{3}$ où $f_D T_s = 0,05$ en présence de dérive Doppler $f_R = 250$ Hz/s avec $N_v = 5$ et $N_D = 8$

Nous pouvons voir sur la Figure 4 que même pour le taux du dérive Doppler le plus élevé rencontré, les performances des deux détecteurs restent exactement les mêmes sans aucune dégradation. Nous pouvons conclure que la dérive Doppler n'est pas un problème pour les deux détecteurs.

Optimization du délai dans un détecteur CPM différentiel

La détection différentielle offre certains avantages qui sont sollicités dans notre application considérée. Pour cela, nous nous sommes intéressés à ce type de récepteurs et avons cherché à améliorer les performances de la technique de réception différentielle classique des CPM pour se rapprocher le plus possible des performances optimales de détection non cohérente. Certains travaux de la littérature suggèrent que l'utilisation de plusieurs symboles de retard donne de meilleures performances en général, nous avons donc cherché une méthode pour optimiser la valeur de retard utilisée.
Nous présentons d'abord notre stratégie de détection, puis exploitons le critère de distance euclidienne minimale pour dériver la stratégie d'optimisation du délai. La performance de la détection différentielle de certains schémas CPM est analysée à travers des simulations de taux

d'erreur binaire pour différentes valeurs de délai à titre de comparaison. Nous donnons ensuite les valeurs de retard optimisées obtenues pour certains schémas CPM. Enfin, nous évaluons les performances de notre détecteur différentiel en présence d'effet Doppler.

Récepteur différentiel basé sur le délai K

Côté récepteur, un signal différentiel noté $R_K(t)$ est obtenu en multipliant le signal reçu $r(t)$ et le conjugué de sa version retardée $r(t - KT_s)$. Il peut être décomposé comme la somme de deux signaux :

$$R_K(t) = \frac{1}{2} r(t) r^*(t - KT_s) = S_K(t, \mathbf{a}) + N_K(t), \tag{16}$$

où le premier terme ne comprend aucune contribution au bruit :

$$S_K(t, \mathbf{a}) = \frac{1}{2} s(t, \mathbf{a}) s^*(t - KT_s, \mathbf{a}) = \frac{E_s}{T_s} \mathrm{e}^{j\Theta_K(t, \mathbf{a})} \tag{17}$$

avec $\Theta_K(t, \mathbf{a}) = \theta(t, \mathbf{a}) - \theta(t - KT_s, \mathbf{a})$.
Le deuxième terme, noté $N_K(t)$, est constitué de composantes dépendantes uniquement du bruit. Il se décompose en $N_K(t) = U_K(t) + W_K(t)$ avec

$$\begin{aligned} U_K(t) &= \frac{1}{2} \left(s(t, \mathbf{a}) e^{j\psi} n^*(t - KT_s) + n(t) s^*(t - T_s, \mathbf{a}) e^{-j\psi} \right), \\ W_K(t) &= \frac{1}{2} \left(n(t) n^*(t - KT_s) \right). \end{aligned} \tag{18}$$

Le calcul de son autocorrélation conduit à l'expression suivante :

$$E[N_K(t) N_K^*(t - \tau)] = (N_0^2 + A^2 N_0) \delta(\tau) \tag{19}$$

avec $A = |s(t, \mathbf{a})| = \sqrt{\frac{2E_s}{T_s}}$ et $\delta(t)$ est la fonction de Dirac. Les détails de ce calcul se trouvent à l'annexe C.1. Par conséquent, nous concluons que le processus aléatoire $N_K(t)$ est stationnaire au sens large avec une moyenne nulle et une densité spectrale de puissance constante (DSP) égale à $(N_0^2 + A^2 N_0)$. Désormais, on la supposera suivre une distribution gaussienne comme dans [13].

Description du treillis de phase

Soit $t = \tau + nT_s$, avec $0 \leq \tau < T_s$ et $n \in \{0, 1, \ldots, N-1\}$. Compte tenu des propriétés de l'impulsion de fréquence, la phase introduite dans (17) peut être décomposée comme la somme d'un terme indépendant du temps et d'un terme dépendant du temps :

$$\Theta_K(\tau + nT_s, \mathbf{a}) = \phi_n + 2\pi h a_n q(\tau) + \varphi_n(\tau), \tag{20}$$

avec $\phi_n = \pi h \sum_{i=0}^{K-1} a_{n-L-i}$ et

$$\varphi_n(\tau) = \quad 2\pi h \sum_{i=1}^{L-1} (a_{n-i} - a_{n-K-i}) q(\tau + iT_s) - a_{n-K} q(\tau). \tag{21}$$

$\varphi_n(\tau)$ représente une contribution dépendante du temps qui correspond aux L derniers symboles de mémoire à la fois du signal et de sa version retardée. Le terme ϕ_n représente la partie indépendante du temps. $\varphi_n(\tau)$ et ϕ_n sont entièrement déterminés par l'ensemble des symboles $(a_{n-i})_{1 \leq i \leq L+K-1}$. Par conséquent, ϕ_n n'a pas besoin d'être stocké, contrairement à la description originale du treillis CPM qui comprend la phase cumulative comme paramètre de définition de l'état. On peut ainsi définir l'état $\Sigma_n = [a_{n-L-K+1}, ..., a_{n-1}]$ pour la n-ième section de la représentation en treillis de $\Theta_K(t, \mathbf{a})$. Notez qu'il existe M^{K+L-1} différents états possibles.

Détection basée sur le maximum de vraisemblance (ML)

Le critère ML est appliqué pour détecter les symboles d'information de $R_K(t)$. Compte tenu de la propriété d'amplitude constante de CPM, cela consiste à maximiser la corrélation entre $R_K(t)$ et toutes les réalisations possibles de $S_K(t, \mathbf{a})$. Le produit interne entre $R_K(t)$ et une réalisation spécifique $S_K(t, \tilde{\mathbf{a}})$, noté $\Gamma_N(\tilde{\mathbf{a}})$, est défini comme :

$$\Gamma_N(\tilde{\mathbf{a}}) = \Re \left[\int_0^{NT_s} R_K(t) S_K^{\star}(t, \tilde{\mathbf{a}}) dt \right], \tag{22}$$

avec $\Re(.)$ désignant l'opérateur de la partie réelle et qui peut être calculé récursivement :

$$\Gamma_n(\tilde{\mathbf{a}}) = \Gamma_{n-1}(\tilde{\mathbf{a}}) + \Lambda_n(\tilde{\mathbf{a}}) \tag{23}$$

avec

$$\Lambda_n(\tilde{\mathbf{a}}) = \Re \left[\int_{(n-1)T_s}^{nT_s} R_K(t) S_K^{\star}(t, \tilde{\mathbf{a}}) dt \right]. \tag{24}$$

L'algorithme de Viterbi est appliqué sur le treillis. A la $n^{\text{ème}}$ section, il calcule pour chaque état la métrique cumulative maximale (23) parmi tous les chemins arrivant à cet état. Le nombre total d'états est donné par $S = M^{K+L-1}$. La Figure 5 montre l'architecture du récepteur différentiel.

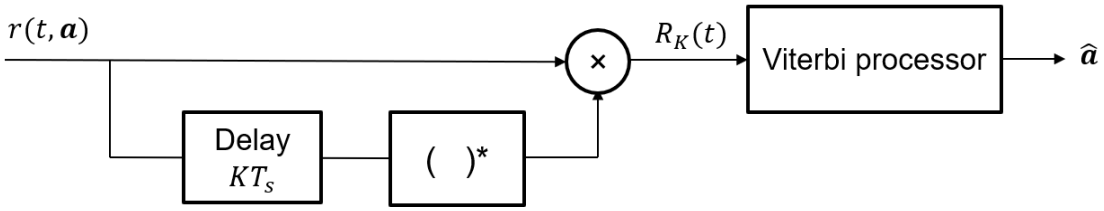

Figure 5 – Architecture du détecteur differentiel

Optimisation du délai

Nous voulons bien choisir le paramètre K pour améliorer la probabilité d'erreur de détection. Considérons l'événement d'erreur suivant: $s(t, \mathbf{a})$ est transmis, $s(t, \tilde{\mathbf{a}})$ est détecté et $\mathbf{a} \neq \tilde{\mathbf{a}}$. Compte tenu du critère de détection ML et de l'indépendance entre R_K et N_K, cela signifie que :

$$\int_0^{NT_s} |R_K(t) - S_K(t, \tilde{\mathbf{a}})|^2 dt \leq \int_0^{NT_s} |R_K(t) - S_K(t, \mathbf{a})|^2 dt \tag{25}$$

qui peut être reformulé comme suit :

$$Z_K \geq \frac{1}{2}\Delta_K^2(\mathbf{a}, \tilde{\mathbf{a}}), \tag{26}$$

où

$$Z_K = \int_0^{NT_s} \Re\big((S_K(t, \mathbf{a}) - S_K(t, \tilde{\mathbf{a}}))\, N_K^*(t)\big) dt, \tag{27}$$

et

$$\Delta_K(\mathbf{a}, \tilde{\mathbf{a}}) = \sqrt{\int_0^{NT_s} |S_K(t, \mathbf{a}) - S_K(t, \tilde{\mathbf{a}})|^2 \, dt}, \tag{28}$$

$\Delta_K(\mathbf{a}, \tilde{\mathbf{a}})$ est la distance euclidienne entre les deux signaux différentiels $S_K(t, \mathbf{a})$ et $S_K(t, \tilde{\mathbf{a}})$ correspondant aux séquences de symboles $\mathbf{a}$ et $\tilde{\mathbf{a}}$. Les détails de ce calcul se trouvent également à l'annexe C.2. Z_K a une moyenne nulle. En supposant que Z_K est gaussien, la probabilité d'un événement d'erreur est donnée par

$$P_e(\mathbf{a}; \tilde{\mathbf{a}}) = Q\left(\sqrt{\frac{\varepsilon_b}{2(N_0^2 + A^2 N_0)} d_K^2(\mathbf{a}, \tilde{\mathbf{a}})}\right) \tag{29}$$

où Q est la *Q-function* et $d_K(\mathbf{a}, \tilde{\mathbf{a}}) = \frac{\Delta_K(\mathbf{a}, \tilde{\mathbf{a}})}{\sqrt{2\varepsilon_b}}$ est la distance euclidienne normalisée, ε_b désignant l'énergie moyenne par bit d'information dans la séquence de symboles différentiels. En procédant comme dans [14, Chapitre 2, Paragraphe 2.1.2], une approximation de la probabilité d'erreur est obtenue à SNR raisonnablement élevé. La probabilité d'erreur est donc approximée par :

$$P_e \propto Q\left(\sqrt{\frac{\varepsilon_b}{2(N_0^2 + A^2 N_0)} d_{\min}^2(K)}\right) \tag{30}$$

où

$$d^2_{\min}(K) = \min_{\substack{\mathbf{a},\tilde{\mathbf{a}} \\ a_0 \neq \tilde{a}_0}} \left(d^2_K(\mathbf{a}, \tilde{\mathbf{a}}) \right) \tag{31}$$

En appliquant le même raisonnement que dans [14], on obtient :

$$d^2_K(\mathbf{a}, \tilde{\mathbf{a}}) = \frac{\log_2(M)}{T_s} \int_0^{NT_s} [1 - \cos(\Theta_K(t, \mathbf{e}))] dt \tag{32}$$

où $\mathbf{e} = \mathbf{a} - \tilde{\mathbf{a}}$ est la séquence de symboles de différence telle que définie dans le premier chapitre. De plus amples détails sur ce calcul de cette formule se trouvent dans l'annexe C.3.
La recherche de la distance euclidienne minimale se fait en recherchant toutes les paires possibles de séquences $\mathbf{a}$ et $\tilde{\mathbf{a}}$. En pratique, ces couples sont ceux dont les chemins respectifs sur un arbre de phase divergent à l'instant 0 et se rejoignent dès que possible. En procédant comme dans [14], l'arbre de différence de phase est une bonne méthode pour déterminer les séquences de symboles de différence à considérer et les paires de séquences de symboles correspondantes. Trouver les paires de séquences $\mathbf{a}$ et $\tilde{\mathbf{a}}$ à considérer dans le calcul de la distance minimale équivaut à trouver leur séquence différence $\mathbf{e} = \mathbf{a} - \tilde{\mathbf{a}}$. Les séquences de différence à considérer sont celles présentant une erreur au début ($e_0 \neq 0$) puis se confondant avec l'axe de phase 0 après quelques symboles. Pour chaque valeur du retard, nous obtenons un arbre de phase différent et ainsi, nous sélectionnons les paires de séquences à considérer en conséquence. Ainsi, une valeur correspondante de la distance euclidienne minimale $d_{\min}$ est obtenue pour chaque valeur du retard considérée dans le processus d'optimisation. Puisque nous cherchons à minimiser la probabilité d'erreur, le meilleur choix de délai est la valeur qui donne le $d_{\min}$ le plus élevé.

Le détecteur différentiel pourrait être particulièrement intéressant dans les applications où le décalage Doppler affecte la communication. Supposons dans notre modèle que nous ayons un décalage de fréquence constant dû à Doppler qui est noté f_D, ainsi le signal reçu sera donné par l'équation (1).
Cela se traduira par un terme de phase constant dans le signal différentiel $R_K(t)$ qui est donné par $\Psi = 2\pi K f_D T_s$. Notez que dans ce terme, le produit $f_D T_s$ est ce qui détermine réellement l'impact de la rotation (puisque finalement $K = K_{opt}$). Pour cette raison, nous avons choisi de présenter les résultats dans cette section en fonction de $f_D T_s$.

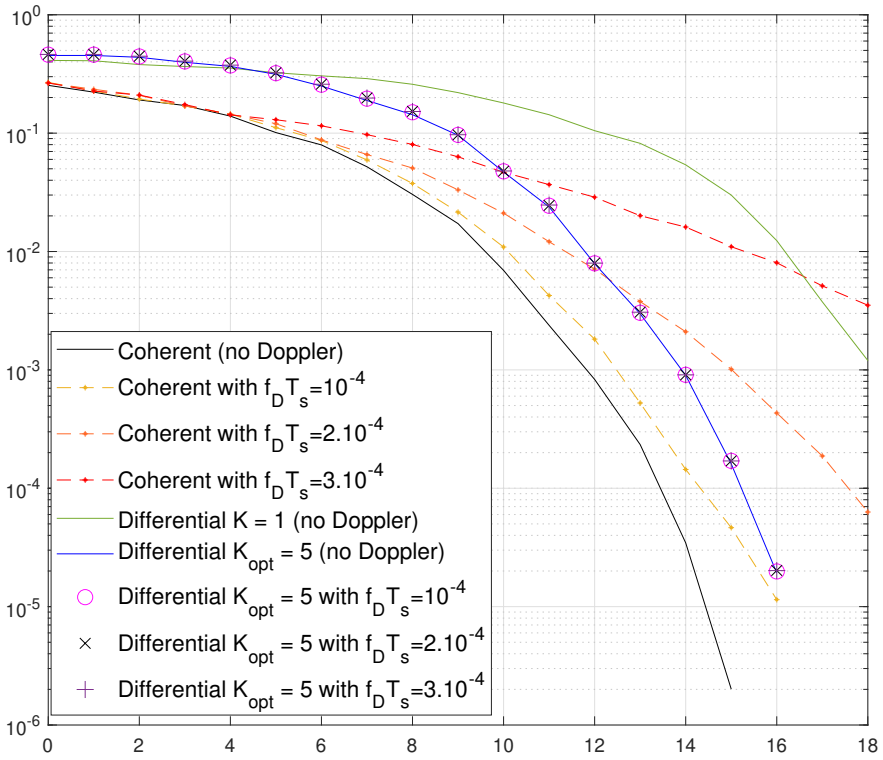

Figure 6 – Comparaison du TER entre détection cohérente et différentielle pour 5REC avec $h = 0.5$ en présence d'un décalage Doppler

Il est connu que la détection cohérente est très sensible au décalage de fréquence et ce que nous voulons souligner ici, c'est la robustesse de notre détecteur différentiel au décalage Doppler. À cette fin, une comparaison des performances entre le détecteur différentiel et le détecteur cohérent en termes de BER est illustrée à la Figure 6 pour l'impulsion rectangulaire avec $h = 0,5$ et $L = 5$ en présence d'un petit décalage Doppler. Nous constatons une énorme dégradation des performances du détecteur cohérent alors que le détecteur différentiel n'est pas affecté pour les valeurs de décalage Doppler considérées.
Pour approfondir cette robustesse, dans la Figure (7), nous considérons le format GMSK et nous montrons les performances du détecteur différentiel à 11 dB en présence d'un décalage Doppler par rapport à la détection différentielle de référence ($K = 1$) et celle cohérente. On voit que le récepteur est robuste au décalage Doppler jusqu'à un ordre de 0.1 de $f_D T_s$ puis les performances commencent lentement à décroître alors que les performances du détecteur non optimisé commencent à décroître plus tôt et la dégradation se produit pour de très petites valeurs de $f_D T_s$ pour le détecteur cohérent. Le même comportement est observé dans le cas d'un

autre format de modulation lorsque $f_D T_s$ augmente.

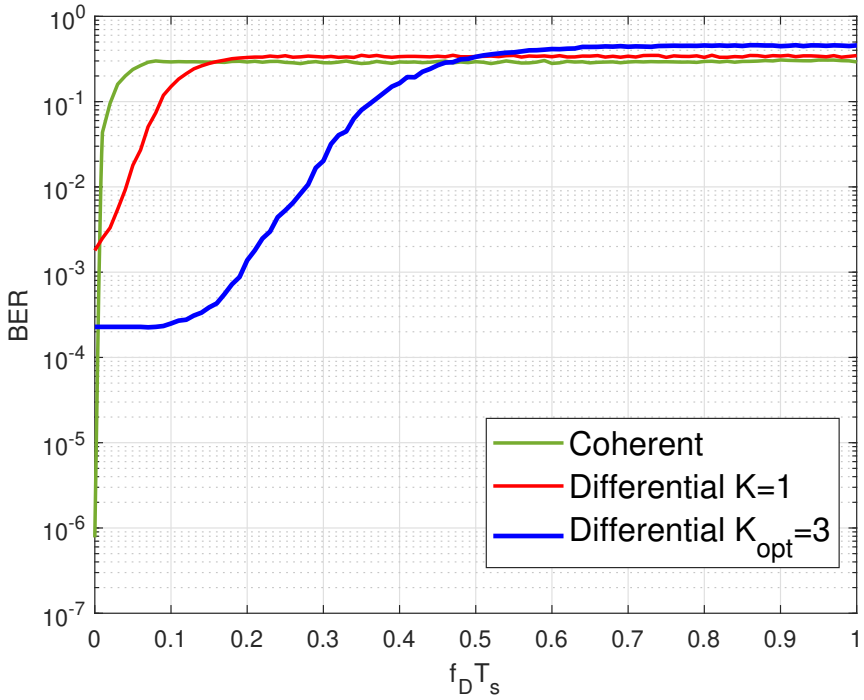

Figure 7 – Comparaison de l'évolution du TER avec $f_D T_s$ pour GMSK pour le détecteur cohérent, le détecteur différentiel pour $K = 1$ et $K_{opt} = 3$ à 11 dB de RSB

Table of Contents

List of acronyms

ACI	Adjacent Channel Interference
AWGN	Additive White Gaussian Noise
BCJR	Bahl, Cocke, Jelinek and Raviv
BER	Bit Error Rate
CPM	Continuous Phase Modulation
CRDSA	Contention Resolution Diversity Slotted ALOHA
DA	Data-Aided
DVB-RCS2	Digital Video Broadcasting - Return Channel via Satellite - Second Generation
FEC	Forward Error Correction
FFT	Fast Fourier Transform
GEO	Geostationary Earth Orbit
GFSK	Gaussian Frequency Shift Keying
GMSK	Gaussian Minimum Shift Keying
GNSS	Global Navigation Satellite System
GSM	Global System for Mobile communication
IoT	Internet of Things
ISM	Industrial, Scientific and Medical
LEO	Low Earth Orbit
LO	Local Oscillator
MAP	Maximum A Posteriori
MEO	Medium Earth Orbit
ML	Maximum Likelihood
MLSD	Maximum Likelihood Sequence Detection
MSK	Minimum Shift Keying
NRMSE	Normalized Root Mean Square Error
NSD	Noncoherent Sequence Detector
PAM	Pulse Amplitude Modulation
PDF	Probability Density Function
PLL	Phase Locked Loop

PSD	Power Spectral Density
PSK	Phase-Shift Keying
PSP	Per Survivor Processing
RC	Raised Cosine
REC	Rectangular
SIC	Successive Interference Cancellation
SNR	Signal-to-Noise Ratio
TFM	Tamed Frequency Modulation
WMF	Multidimensional Whitening Filter

List of Figures

List of Tables

INTRODUCTION

The Internet of Things

Internet of Things (IoT) is a term that appeared in newspapers in the early 2000s [16]. It is a concept describing new digital communications field: objects can access the Internet without requiring human intervention. One can hence speak of connected objects. These objects have their own utility: measure a temperature, open a window or detect a person or an animal, etc. They see their use extended by Internet access. This allows users to control them remotely, recover data, or receive alerts in the event of a problem. Many markets, such as home automation, are seeing their appeal grow. The number of users is constantly increasing, and this keeps pushing actors in the market to develop more efficient solutions.

The IoT has been defined by the International Telecommunication Union (ITU) as a "global infrastructure for the information society, which makes it possible to have advanced services by interconnecting objects (physical or virtual) thanks to technologies of information existing or evolving inter-operable information and communication systems" [17]. I find in this definition the notion of the establishment of an infrastructure which aims to increase the usefulness of objects through communications between them. Thus, when talking about the Internet of Things, one have to think of objects, but also of everything related to their interconnection: servers, routers, and data management platforms.

The term "machine" is also used in the context of radiocommunications, designating an object or a server. One is talking about machine-to-machine communication, or M2M (Machine-to-Machine), simply when objects communicate autonomously through a wired or wireless network. M2M communications are part of the Internet of Things, providing communication links on a homogeneous network.

In this Thesis, I focus on the same communication context of IoT networks. These networks are called Low Power Wide Area Networks (LPWAN) and their goal is to connect huge number of communicating objects within a very long range. A brief summary of the main LPWAN technologies can be found in Appendix A.

IoT and satellite communications

In light of increasing number of IoT applications, LPWAN operators are seeking global coverage to reach the greatest possible number of potential customers, while minimizing the costs of implementing the service. This can be granted using satellites in two different manners.

The first approach is *Indirect-to-Satellite* IoT. In this context, the satellite plays the role of a backhauling system. Each communicating object in the network may communicate with the satellite through an intermediate gateway in rural or less inhabited area. The satellite then collects the data from this gateway when the latter is in its field of view and relays it later to the network by sending back the collected data to a base transceiver station. Indirect approaches essentially leverage an existing satellite and LPWAN protocols and extend the coverage of an existing network. This extension principle is similar to what has been proposed for the GSM network [18] in the framework of the European Space Agency (ESA) study to extend the coverage of this network.

The second approach, the one which interests us the most is the *Direct-to-Satellite* IoT [1]. This is the preferred approach since no intermediate ground gateway is required, facilitating and speeding up the deployment of wide coverage IoT. In this context, the satellite collects the data directly from the communicating objects and processes them. It should also be able to communicate back with the object if downlink is considered. This approach pushes the range of the network further than LPWAN while still requiring the same available bandwidth [1] as presented in Figure 8 and this rises some issues in terms of physical layer. The big challenge here is to be able to create a reliable long range communication link having limited resources in both the satellite and the object while facing the problems of a satellite link. This can be achieved either by using the existing LPWAN technologies to transmit to the satellite, or by providing new MAC and physical layers specifically dedicated to this application.

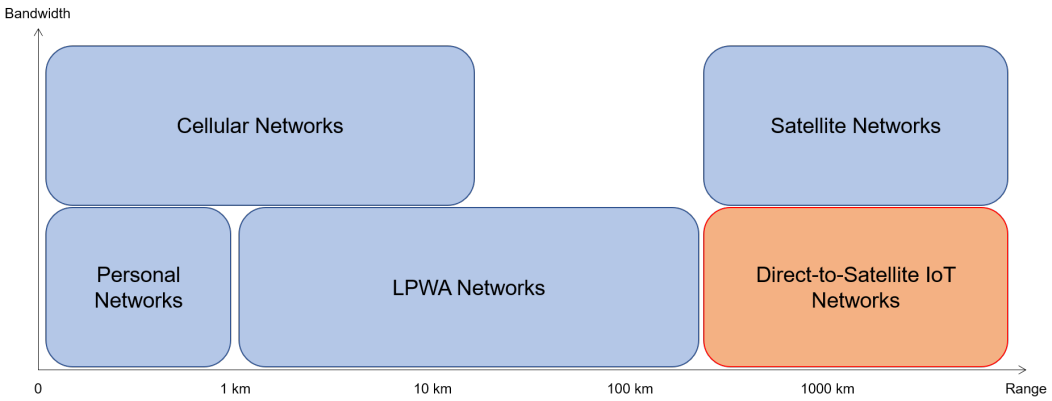

Figure 8 – Bandwidth versus range for different types of networks [1]

Scope of the Thesis

In this Thesis, I consider a communicating object transmitting to the satellite (uplink). The satellite then has to decode the information and doesn't just act as a relay system. Limited available power onboard makes the complexity an important issue. Considering cost and energy constraints at the transmission side, I want to consider constant amplitude modulations and more specifically Continuous Phase Modulations (CPM)

The issue I am tackling is the Doppler effect highly present in the satellite link. Indeed, the Doppler shift heavily affects the detection and I present multiple detectors with different levels of complexity to mitigate this problem. The phase mismatch is also considered in the transmission model. It is due to time delay of the propagation of the signal and low precision of the local oscillators used in transmitting objects to allow for low cost terminals. Another aspect I focused on is that the detection has to be in a blind way in relation with Doppler whenever it is possible since in short frame IoT communications, it can not allow for long pilot symbols (if any) to preserve the power of the terminals and to efficiently use the frequency band.

The PhD contributions are the following :

- First, I introduce a novel CPM non-coherent detection based on the direct application of the generalized maximum likelihood principle with the insertion of blind Doppler estimation principle of [9] in the proposed algorithm as well as in the CPM non-coherent detection of [10]. From this, I derive two detectors with different levels of complexity.
- Second, I present the theoretical extension of the usual CPM differential detection algorithm to consider a delay higher than one symbol period (including the description of the phase trellis and the derivation of the equations of the branch and cumulative metrics).
  The different results of this work were published in :
  - A. Jerbi, K. Amis, F. Guilloud, and T. Benaddi, "Non-Coherent CPM Detection Under Gaussian Channel Affected With Doppler Shift," IEEE 33rd Annual International Symposium on Personal, Indoor and Mobile Radio Communications (PIMRC): IEEE PIMRC, 2022.
  - A. Jerbi, K. Amis, F. Guilloud, and T. Benaddi, " Détection non-cohérente des modulations CPM en présence d'un décalage Doppler," XXVIIIème Colloque Francophone de Traitement du Signal et des Images, GRETSI'22, 2022.

- Third, for the improved differential detection, I give a method to systematically determine an optimized delay value based on the application of the minimum Euclidean distance criterion between two CPM differential signals and I present the optimized delay values for different CPM formats (modulation index, frequency pulse length, frequency pulse type).

  The different results of this work were published in :

  — A. Jerbi, K. Amis, F. Guilloud, and T. Benaddi, "Delay Optimization of Conventional Non-Coherent Differential CPM Detection," IEEE Communications Letters, 2022, doi: 10.1109/LCOMM.2022.3220326.

- Fourth, I compare the delay-optimized differential detector in presence of Doppler shifts with the first two introduced detectors in terms of performance/complexity and discuss the advantages and drawbacks of them.

Outline of the Thesis

This document is organized as follows:

Chapter 1 is dedicated first to defining some key elements to describe the satellite link especially in terms of Doppler orders encountered in the channel. I then present the Continuous Phase Modulation and the motivations to consider this kind of modulation.

In Chapter 2 starts from the non coherent sequence detection criterion - as it can mitigate the problem of phase instabilities to come up two detectors robust to Doppler shifts with different complexity levels.

In Chapter 3, the goal is to reduce complexity while still being robust to Doppler as much as possible. Hence, the focus shifts towards differential reception which can offer reduced complexity. I present a method to enhance the performance of a multiple symbol differential detection technique by optimizing the delay used and then assess its robustness to Doppler as well. A comparison with detectors developed in Chapter 2 is then presented.

In Chapter 4, in addition to Doppler, I consider a multiuser case scenario where multiple communicating objects are randomly accessing the channel and the current packet of interest is corrupted by interference. I detail the reception conditions in the first place and then present the performance of our detectors in such conditions.

Finally, I provide some conclusion on the results achieved as well as some perspectives and remarks.

Chapter 1

CPM for Satellite IoT

Contents

This chapter first presents the aspects of the satellite channel and some basic principles on LEO satellites that impacts the communication (visibility, link budget, Doppler). Then, we present Continuous Phase Modulation (CPM) motivations, principles, transmitter and detection.

1.1 Low Earth Orbit Satellite link

Satellite communications have started since early sixties of the past century. This technology offers some great advantages and made it possible the existence of some unique applications like the Global Navigation Satellite Systems (GNSS) for instance [19]. Satellites travel around the Earth following a given orbit. These orbits are classified according to the satellite altitude resulting in three types: Low Earth Orbit (LEO), Medium Earth Orbit (MEO) and Geostationary Earth Orbit (GEO). We are interested in the first one since most of the artificial objects in outer space are in LEO. The fact that the satellite in this orbit is closer to the Earth compared to other orbits allows for low transmission power, better link budget and narrower field of view which can limit the interference. Given these properties, this orbit is more adapted to the IoT application.

A Low Earth Orbit is generally defined as one with an altitude between 500 and 2000 km [20]. Unlike GEO satellites, satellites in Low Earth orbit do not remain fixed with respect to a single location on the Earth's surface. Rather, these objects move around the planet at very high speeds. Since the satellites in this orbit are constantly moving, it would be impossible to depend on a single satellite to provide any form of global coverage. This leads to the concept of satellite constellation, which refers to a large number of communicating satellites on different LEO orbits working in synergy to ensure seamless coverage. One of the most famous LEO constellations is the Iridium satellite constellation [21].

1.1.1 Satellite visibility

As stated, LEO satellites do not remain fixed with respect to a single location on the Earth surface. Therefore, the knowledge of the satellite visibility range and period is needed. The visibility of the satellite is usually specified by a minimum elevation angle $\gamma_{\min}$ as illustrated in Figure 1.1. This angle indicates the minimum elevation of the satellite over the horizon from the object's point of view to enable communication. In Figure 1.1, the point T represents the communicating object (or Terminal), the point S_{sat} represents the satellite and the point S_{sub} is the sub-satellite point that is the orthogonal projection of the satellite on the Earth surface. The minimum elevation angle varies from an application to another and it depends on various parameters. The power and the antenna type for instance used by both the satellite and the communicating object affects the minimum elevation angle. It generally varies between 5° and 15°. For IRIDIUM satellite system, the minimum elevation angle is 8.2° [22]. We also define the maximum elevation angle $\gamma_{\max}$. It corresponds to the scenario where the sub-satellite point S_{sub} is the closest to the terminal point T. The elevation angle from the object's point of view ranges from 0° to 90°, where the limit 90° is the case where the sub-satellite point is exactly the point T. The maximum elevation angle depends on the inclination of satellite orbit ξ with respect to

the Earth equator as presented in Figure 1.1.
Considering the parameters illustrated in Figure 1.1, the angle β between the object and the sub-satellite point is related to the elevation angle γ and can be expressed by:

$$\beta = \cos^{-1}\left(\frac{R_e}{R_e + H}\cos(\gamma) - \gamma\right) \tag{1.1}$$

Thus, when γ varies between $\gamma_{\min}$ and $\gamma_{\max}$, then β correspondingly varies between $\beta_{\min}$ and $\beta_{\max}$. In [23], an algorithm is presented to obtain an estimate of the satellite visibility time. It is is related to the satellite in-view period $\tau(\gamma_{\max})$ that is given by :

$$\tau(\gamma_{\max}) \approx \frac{2}{\omega_S - \omega_E \cos(\xi)} \times \cos^{-1}\left(\frac{\cos(\beta_{\min})}{\cos(\beta_{\max})}\right) \tag{1.2}$$

where ω_S and ω_E are the angular velocity of the satellite (in the Earth centered inertial reference frame) and the Earth respectively. More details on the derivation of this equation can be found in [23]. In short, depending on different scenarios and configurations, the visibility time expected with LEO satellites ranges from about 5 to almost 20 minutes [24] depending on the satellite's altitude and the elevation angle.

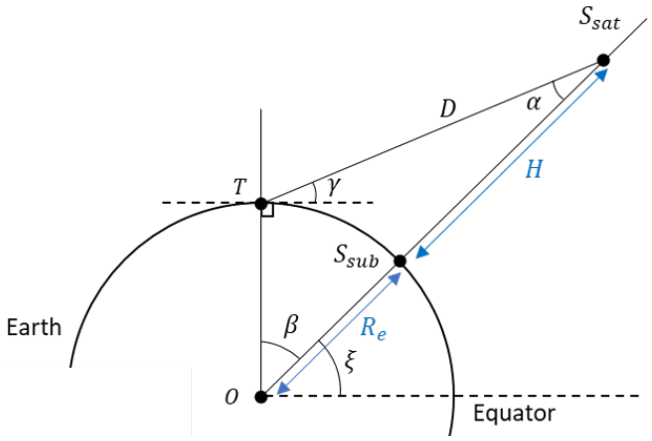

Figure 1.1 – Geometry of the link between the object T and the satellite S_{sat}

1.1.2 Link budget

Calculation of the available link budget is an important step when designing a communication link. The goal is to explicit the signal to noise ratio (SNR) using the different parameters that affect power levels throughout the transmission. The SNR at receiver input in general is given by [25]:

$$\text{SNR} = \frac{\text{Signal power level at reception}}{\text{Noise power level at reception}} \tag{1.3}$$

The signal power level depends on various parameters :

— Equivalent Isotropic Radiated Power (EIRP) : it is related to the transmitting object and is given by :

$$\text{EIRP} = \frac{P_{Tx} G_{Tx}}{L_{line}} \tag{1.4}$$

where P_{Tx} is the transmitted power, G_{Tx} is the transmitter antenna gain and L_{line} is the transmission line loss.

— Free Space Loss L_{space}: it is a loss related to line of sight path between the object and the satellite. It is related to the distance D and the wavelength of the carrier λ_0 and is given by :

$$L_{space} = \left(\frac{4\pi D}{\lambda_0}\right)^2 \tag{1.5}$$

— Polarization Loss L_{pol}: it is due to polarization mismatch between the transmitter and receiver antennas.

— Antenna gain at the receiver G_{Rx}: it is characteristic to the satellite's antenna.

— Various other losses that can be modeled by L_o. This includes the atmospheric loss (that affects K, Ku and Ka band much more than sub 1 GHz bands [26]), depointing losses due to imperfect alignment of the transmitting and receiving antennas and also some losses from components imperfections.

The noise power level at reception is given by :

$$\text{Noise power level at reception} = k_B T_A B \tag{1.6}$$

where T_A is the antenna's noise temperature, B is the received signal's bandwidth and $k_B = 1.38 \times 10^{-23}$ J/K is the Boltzmann constant. Ultimately, the SNR is given by :

$$\text{SNR} = \frac{\text{EIRP}\ G_{Rx}}{k_B\ T_A\ B\ L_{space}\ L_{pol}\ L_o} \tag{1.7}$$

In general, a minimum signal to noise ratio (threshold) is set to guarantee a reliable communication. This threshold depends on the sensitivity of the receiver. Studies providing an estimate of the link budget using NB-IoT with satellites are available in [27] and [28]. Our interest is not the NB-IoT systems but similar available link budget is expected in our context.

1.1.3 Doppler effect

The typical velocity of a LEO satellite is around 7.6 km/s. The satellite movement at such velocity is the cause of a very high Doppler effect. The Doppler effect is a change in the frequency of the transmitted signal observed by the receiver in case of motion of one in relation to the

other. The frequency change is called *Doppler shift*, and this shift can also change in time at a certain rate which is called *Doppler rate*. The Doppler effect is one of the main issues in LEO satellite communications. Therefore, we need to estimate typical Doppler shifts and rates in a LEO satellite scenario to have an information about the orders that we are dealing with. To this end, and without loss of generalities, we consider a typical scenario in Figure 1.2 where the object is designated by the point T and the satellite by S_{sat}. The satellite is moving from point W to the north pole point N. The object T is located with a latitude l and a longitude L. First step is to determine the distance $D(t)$ between the satellite and the transmitting object. This distance will be expressed as a function of the angle $\varphi(t) = Vt$ where V is the angular velocity of the satellite.

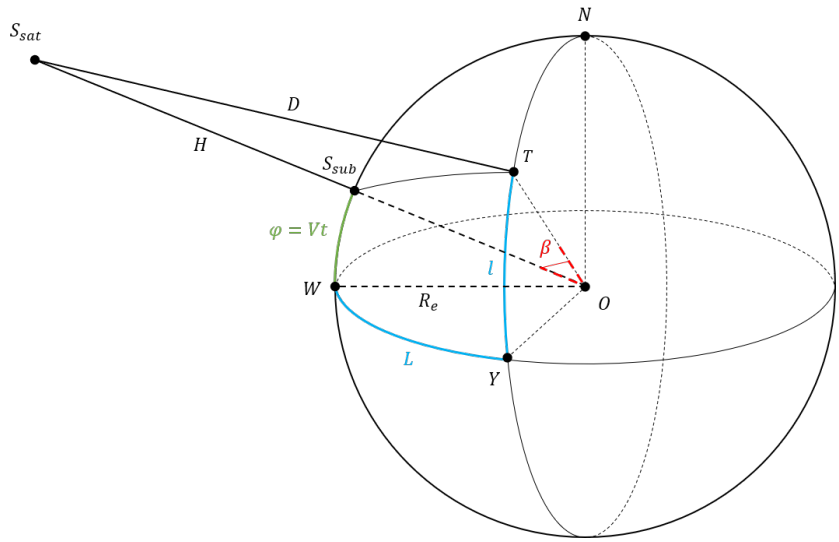

Figure 1.2 – Space geometry of the link between the object and the satellite

From [26], the distance D as function of time is given by:

$$D(t) = \sqrt{R_e^2 + (R_e + H)^2 - 2R_e(R_e + H).\left(\cos(L)\cos(Vt)\cos(l) + \sin(Vt)\sin(l)\right)} \tag{1.8}$$

We then define the satellite velocity as $V_s(t) = \frac{\mathrm{d}D(t)}{\mathrm{d}t}$. In this Satellite IoT application, we consider a non moving object. Hence, the Doppler shift $f_D(t)$ and the Doppler rate $f_R(t)$ are given by :

$$f_D(t) = -\frac{f_0}{c}V_s(t) \tag{1.9}$$

$$f_R(t) = -\frac{f_0}{c}\frac{\mathrm{d}V_s(t)}{\mathrm{d}t} \tag{1.10}$$

where f_0 is the carrier frequency and c is the light speed in vacuum. The exact expressions of $f_D(t)$ and $f_R(t)$ can be found in [29]. This Doppler model is still valid for a moving object since

its movement is very slow compared to satellite and thus it can be considered immobile from the satellite perspective.
From Equations (1.9) and (1.10), it is obvious that the Doppler effect depends on the carrier frequency and the LEO orbit altitude H. To highlight this dependence, we present the Doppler shift profile obtained according to Equation (1.9) for multiple altitudes in the LEO range and considering the visibility window of the satellite. The satellite velocity is adjusted accordingly as in [30] from 7.604 km/s in the lowest altitude to 6.704 km/s at the highest altitude. The curves are given in Figure 1.3.

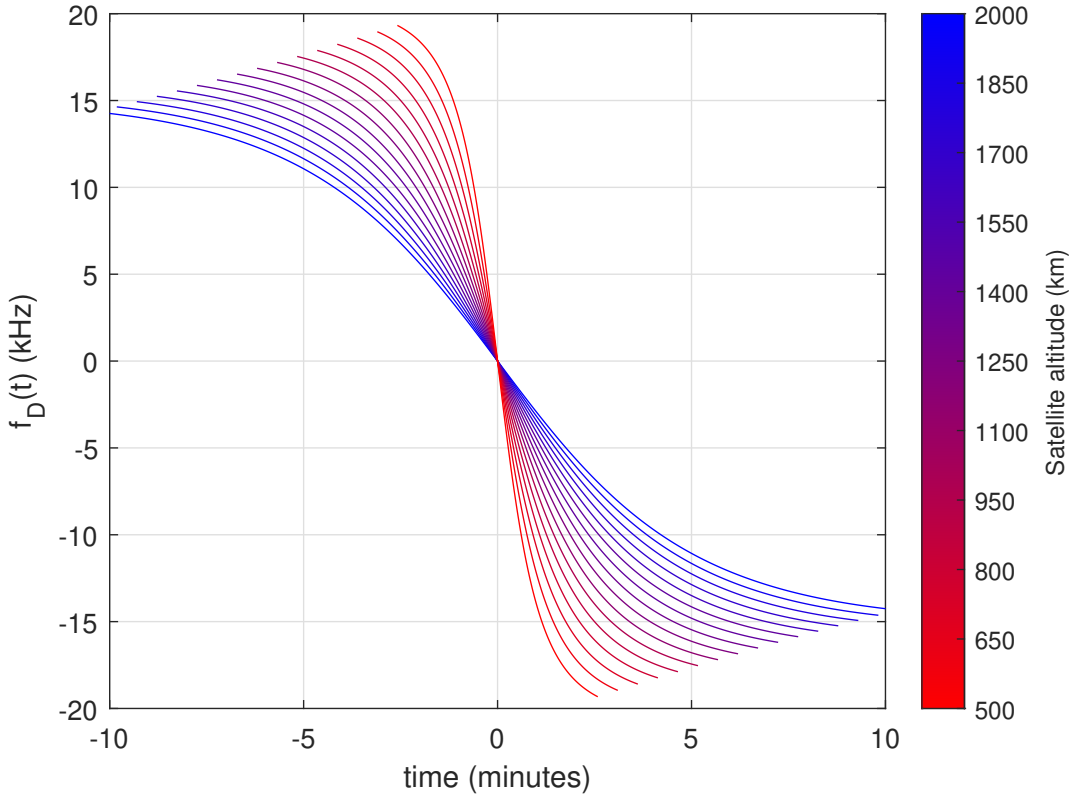

Figure 1.3 – Doppler shift profile with $f_0 = 868$ MHz at multiple altitudes considering the visibility window of the satellite where $W = T$ ($l = 0$, $L = 0$) and when $t = 0$, then $T = S_{sub}$

In Figure 1.3, we considered the case where the satellite passes above the object (the case where $\beta = 0$) since this case provides maximum visibility window and with no loss of generalities, the object is placed at latitude $l = 0$ and longitude $L = 0$. The carrier frequency is chosen in ISM band at $f_0 = 868$ MHz. Time axis is represented relative to the zero Doppler instant. The zero Doppler instant is the time during the visibility window at which the elevation angle from the terminal to the satellite is at its maximum value and the satellite is at its closest approach

to the terminal. The corresponding Doppler rate profiles are plotted in Figure 1.4.

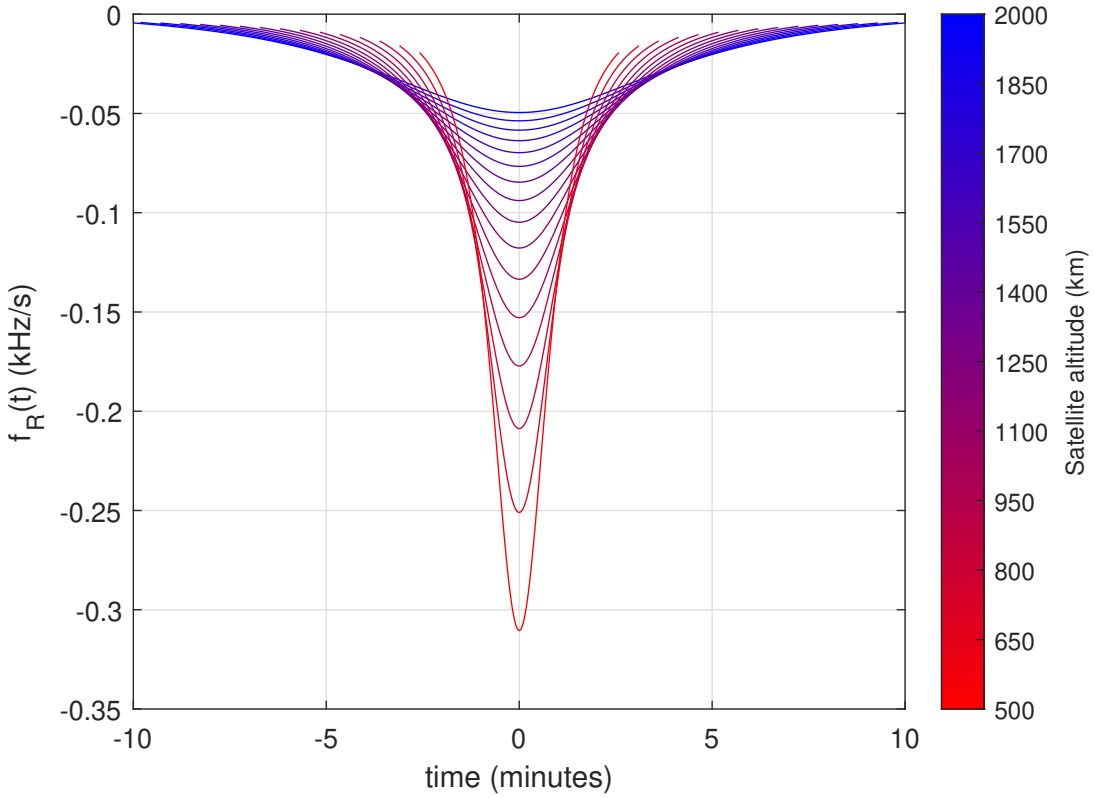

Figure 1.4 – Doppler rate profile with $f_0 = 868$ MHz at multiple altitudes considering the visibility window of the satellite where $W = T$ ($l = 0$, $L = 0$) and when $t = 0$, then $T = S_{sub}$

From Figures 1.3 and 1.4, we can see that Doppler shift orders decrease with higher altitudes going from a maximum of 20 kHz down to about 14 kHz, and the variation tends to slow in time as altitude increases as well. Similar profiles can be found for Eutelsat nano-satellites [31]. Another method to estimate the maximum theoretical Doppler shift that could occur when the satellite is at the horizon is provided in [26] using the following formula :

$$f_{D\max} \cong \pm 1.54 \times 10^{-6} f_0 m \qquad \text{(Hz)} \tag{1.11}$$

where f_0 is the carrier frequency, and m is the number of revolutions per day of the satellite. For example, let us take the scenario of a LEO satellite with an altitude of 600 km traveling at 7.6 km/s. This satellite makes around m=15 revolutions per day. For this scenario, the maximum Doppler shift expected according to Equation (1.11) is around 20 kHz. This is in adequation with the Doppler shift profile presented in Figure 1.3 but one has to keep in mind that this formula is for the extreme case in which the satellite is at the horizon and not exactly within the

minimum elevation angle range which explains the small difference with the presented profile. Thus, this formula is used to compute the theoretical maximum.
The aforementioned Doppler shift orders correspond to the case of maximum visibility whereas in practice, it can get a bit less since satellite orbit is often inclined. This limits the maximum elevation angle which in return further shortens the visibility time. The Doppler shift profile as a function of the maximum elevation angle is given in [32] where we can see that for a maximum elevation angle of 11.4°, Doppler order can get as low as 5 kHz for the considered scenario of Figures 1.3 at 1000 km of altitude.
More Doppler profiles for different frequency bands and different configurations can be found in [30], in [33], in [34] and in [35]. All of these works confirms the presented profiles.
In summary, if we are considering the 868 MHz ISM frequency band for the Satellite IoT application, a Doppler shift ranging from about 5 to 20 kHz is expected and *slowly* varies in time for a short frame communication according to Doppler rate.
After presenting essential elements concerning the LEO satellite link, we will present in the next section the waveform that we will be focusing on in this thesis.

1.2 Continuous Phase Modulation

Continuous Phase Modulation (CPM) is a type of non linear modulation where the transmitted information is embedded within the phase of the signal. It uses memory in order to ensure that the phase transition between transmitted symbols is continuous in time. It is a constant envelope modulation which grants it power efficiency. This modulation technique was formalized by T. Aulin and C. Sundberg in 1981 ([36],[37]). Throughout this section we will describe it in details.

1.2.1 Motivations

When choosing a waveform for any wireless communication application, three major elements need to be investigated; performance, complexity and bandwidth. In general, the chosen waveform is the one that gives the best trade-off between these three elements.
For LEO satellite applications, major impairments affecting the performance are taken into account. The phase instabilities, the high Doppler shift, the interference in a multiuser scenario, the non-linear amplifiers generally used at both transmission sides, at the communicating objects and aboard the satellite, etc.
In terms of complexity, it is important to be as low as possible since in the targeted application, communicating objects use small batteries and the satellite is not just a simple relay, but instead, it does some of the processing and considering the limited resources onboard, complexity is a major constraint. The bandwidth in the targeted application may also be an issue. Whether it

operates in licensed or unlicensed frequency bands, the available bandwidth is limited.
Continuous Phase Modulation (CPM) is a class of modulation that encompasses several families of phase modulation waveforms. It has different parameters that can be adjusted to meet the application needs. Research works investigating the design of CPM waveforms with satellite systems to yield good performance from power and spectral point of view showed some promising results. The energy efficiency problem has been discussed in [2] an [3]. Study on how to chose spectrally-efficient CPM schemes has been presented in [4]. Adjacent channel interference (ACI) has also been assessed in [5] and the possibility of using coding schemes to solve some of the mentionned problems using Ka frequency band can be found in [6]. While the cited works may not specifically apply to the Satellite IoT application, they provide however good founding backgrounds towards deriving solutions adapted to our problem.
Some standards based on satellite communications already use a CPM format. We can mention the digital video broadcasting standard DVB-RCS2 [7] which was published by the international consortium *DVB project*. More recently, a GFSK scheme has also been adopted by Semtech as a candidate for the *Long Range Frequency Hopping Spread Spectrum* (LR-FHSS) technique [8]. Given all these details, we chose to focus on CPM waveform in this work to exploit its potential in the considered application and we particularly studied its reception from the satellite's point of view (uplink).

1.2.2 Signal model

Let $\mathbf{a}$ be a sequence of N independent and identically distributed (i.i.d.) information symbols to be transmitted denoted by $\mathbf{a} = \{a_i\}_{0 \leq i \leq N-1}$. Given M an even positive integer, a_i takes on values in the M-ary alphabet $\mathcal{M} = \{\pm 1, \pm 3, .. \pm (M-1)\}$ with equal probabilities. M is called the modulation order. The complex envelope of the CPM-modulated signal is given by:

$$s(t, \mathbf{a}) = \sqrt{\frac{2E_s}{T_s}} \mathrm{e}^{j\theta(t,\mathbf{a})}, \tag{1.12}$$

where E_s is the average symbol energy, T_s is the symbol duration and $\theta(t, \mathbf{a})$ is the signal phase which depends on the information symbols. It is defined by :

$$\theta(t, \mathbf{a}) = 2\pi h \sum_{i=0}^{N-1} a_i q(t - iT_s), \tag{1.13}$$

where h is called the modulation index and $q(t)$ is called the *phase shaping* pulse.
h is usually taken as a constant rational number smaller than 1 and can be written as $h = \frac{r}{p}$ with r and p being relatively prime integers. The modulation index affects the spectral occupancy; the smaller it is, the narrower the occupied bandwidth is. It should be mentioned that there exist some CPM implementations using a modulation index that varies in a cyclic manner ([38],

[39]) in which case we are talking about *multi-h* CPM. However, throughout our work, we only consider constant h CPM schemes.
The phase shaping pulse $q(t)$ is given by:

$$q(t) = \int_{-\infty}^{t} g(u)du \tag{1.14}$$

where $g(t)$ is called the *normalized frequency pulse*. In practice, $g(t)$ has a finite duration LT_s ($L \in \mathbb{N}$) and it must satisfy the following conditions:

$$\begin{cases} g(t) = g(LT_s - t), & 0 \leq t < LT_s \\ \int_{-\infty}^{t} g(\tau)\mathrm{d}\tau = q(LT_s) = \frac{1}{2}, & \forall t \geq LT_s \end{cases} \tag{1.15}$$

L refers to the CPM memory and verifies $L \geq 1$. When $L = 1$, the scheme is said *full response* CPM, otherwise, it's called *partial response* CPM. Increased CPM memory means much smoother phase transition which leads to smaller spectrum side lobes. However, this comes at the cost of increased complexity at the receiver as we shall see later on.
$g(t)$ defines the phase trajectory shape and affects the spectral occupancy as well. Several formats are available in the literature; the rectangular (REC), the Raised-cosine (RC), and the Gaussian are the most popular shapes used. Table 1.1 summarizes the analytical expression of $g(t)$ for different formats.
As it is noted in Table 1.1, CPM schemes having a finite frequency pulse support $[0, LT_s]$ are

Table 1.1 – Frequency pulse shape examples

Notation	**Frequency pulse**	**Support**
LREC	$g(t) = \begin{cases} \frac{1}{2LT_s}, & 0 \leq t < LT_s \\ 0, & \text{otherwise} \end{cases}$	$[0, LT_s]$
LRC	$g(t) = \begin{cases} \frac{1}{2LT_s}\left[1 - \cos(\frac{2\pi t}{LT_s})\right], & 0 \leq t < LT_s \\ 0, & \text{otherwise} \end{cases}$	$[0, LT_s]$
GMSK	$g(t) = \frac{1}{2T_s}\left[Q\left(\frac{2\pi B}{\sqrt{\ln(2)}}\left(t - \frac{T_s}{2}\right)\right) - Q\left(\frac{2\pi B}{\sqrt{\ln(2)}}\left(t + \frac{T_s}{2}\right)\right)\right]$ with $Q(t) = \frac{1}{\sqrt{2\pi}}\int_t^{+\infty} e^{-\frac{\tau^2}{2}} d\tau$	infinite

usually denoted by "L *pulse shape*" (like LREC or LRC). For CPM schemes with infinite frequency pulse support, it is necessary to do a truncation. GMSK refers to *Gaussian Minimum Shift Keying* and for the scheme, the parameter BT_s is called the 3 dB bandwidth time product and usually verifies $0 \leq BT_s \leq 1$. In practice, the GMSK frequency pulse support is truncated

to $[0, LT_s]$ and will be referred to as LGMSK. Note that the choice of L should depend on BT_s. For example, the GMSK used in the GSM specification sets $L = 3$ with $BT_s = 0.3$ [40].
Figure 1.5 shows the plot in time domain of the above mentioned frequency pulses $g(t)$ and their corresponding phase pulses $q(t)$.

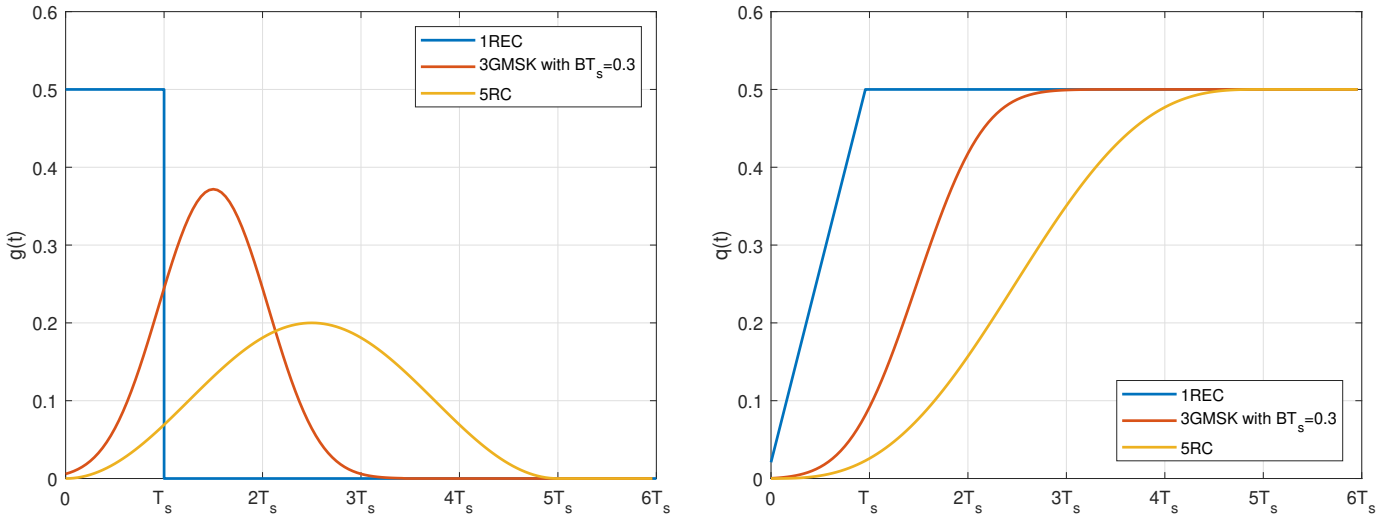

(a) Frequency pulses

(b) Phase pulses

Figure 1.5 – Examples of $g(t)$ and their corresponding $q(t)$

CPM is a modulation that uses memory, and unlike memoryless modulation schemes, symbols cannot be presented on a mapping graph at one symbol period. In the CPM case, the past symbols (memory symbols) need to be known as the CPM phase in a given symbol interval depends on them and the current input symbol. We use a trellis representation which gives all realizations of the CPM phase that carries the information throughout the transmission. With that said, any trellis is defined by a vector that describes its states and by a recursion formula that describes the relation between those states (it's the phase transition in our case). In order to define the trellis representation, we need to examine the phase of the CPM signal.

For $t \in [nT_s, (n+1)T_s[$, the phase of the signal can be written as:

$$\begin{aligned}\theta(t, \mathbf{a}) &= 2\pi h \sum_{i=0}^{n} a_i q(t - iT_s) \\ &= 2\pi h \sum_{i=n-L+1}^{n} a_i q(t - iT_s) + 2\pi h \sum_{i=0}^{n-L} a_i q(t - iT_s) \\ &= 2\pi h a_n q(t - nT_s) + 2\pi h \sum_{i=n-L+1}^{n-1} a_i q(t - iT_s) + \pi h \sum_{i=0}^{n-L} a_i \\ &= 2\pi h a_n q(t - nT_s) + \Theta_n(t) + \theta_n\end{aligned} \tag{1.16}$$

Hence we have now three terms in the expression of $\theta(t, \mathbf{a})$, the first term is the current symbol contribution to the phase, the second term $\Theta_n(t)$ describes the contribution of the last $(L-1)$ symbols and the third term θ_n which is independent of the current symbol interval, describes the contribution of the rest of the past symbols. If h is rational, the phase evolution can be represented by a trellis whose states are given by the state vector :

$$\sigma_n = [\theta_n, a_{n-L+1}, ..., a_{n-1}] \tag{1.17}$$

and the transmitted signal is easily deduced by the equation of the CPM signal in the $[nT_s, (n+1)T_s[$ symbol interval and the values of $[\sigma_n, a_n]$. The next state is simply given by:

$$\sigma_{n+1} = \left[[\theta_n + \pi h a_{n-L+1}]_{2\pi}, a_{n-L+2}, ..., a_{n-1}, a_n\right] \tag{1.18}$$

where $[.]_{2\pi}$ is the modulo 2π operator. Figure 1.6 shows an illustration of the transition between two trellis states.

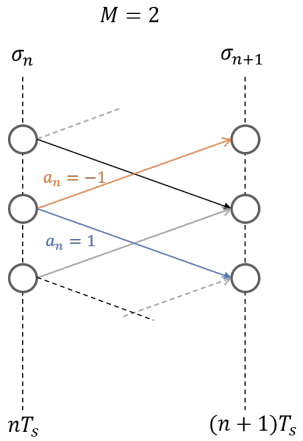

Figure 1.6 – Transition between two trellis states

The number of trellis states depends on $h = \frac{r}{p}$ and more precisely, on the parity of the numerator r of h, hence if:

— r is even $\Rightarrow \theta_n$ takes p values; $\theta_n \in \left\{0, \frac{\pi r}{p}, \frac{2\pi r}{p}, .., \frac{(p-1)\pi r}{p}\right\}$

— r is odd $\Rightarrow \theta_n$ takes $2p$ values; $\theta_n \in \left\{0, \frac{\pi r}{p}, \frac{2\pi r}{p}, .., \frac{(2p-1)\pi r}{p}\right\}$

Hence, we end up with a trellis having:

— pM^{L-1} states and pM^L transitions if r is even.

— $2pM^{L-1}$ states and $2pM^L$ transitions if r is odd.

To every possible realization of the vector $[\sigma_n, a_n]$ corresponds a phase realization or what otherwise is called a phase trajectory and the set of all possible phase trajectories forms a phase tree. Figure 1.7a shows the phase tree of the MSK scheme (binary 1REC with h=0.5). When we perform the modulo-2π operation on this phase tree, it collapses into a section of the whole trellis structure of the MSK as depicted in Figure 1.7b.

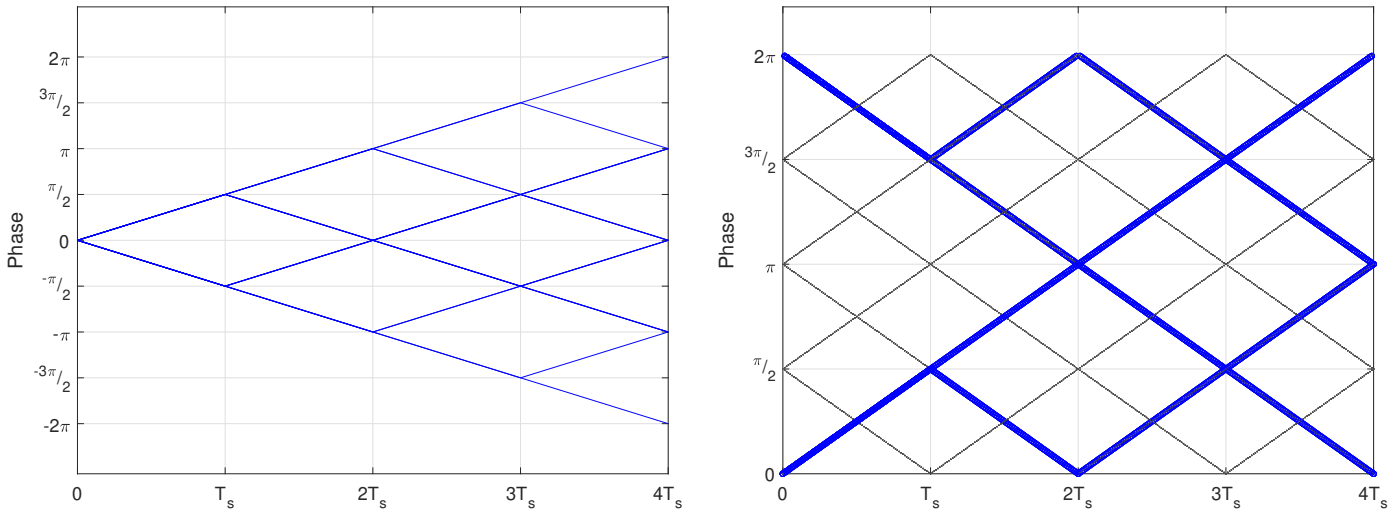

(a) Phase tree

(b) Modulo 2π of the phase tree as part of the phase trellis

Figure 1.7 – Phase tree and trellis of the MSK

1.2.3 Linear decomposition of the CPM

In general, good CPM schemes are those having long enough memory and small enough modulation index [41]. This results into increased complexity receivers as we have seen from the previous section that the number of phase states increases with these parameters. Some CPM schemes for instance require a detector operating with 512 or more states [42]. This was the motivation behind searching for alternative *methods* to represent the CPM signal that are easier to implement and can reduce the receiver's complexity.
Many decompositions of the CPM have been proposed in the literature. We can cite the Rimoldi decomposition [43] which creates time-invariant trellis of the CPM, there is the orthogonal decomposition [44] and the non-orthogonal exponential expansion [45] and also decompositions for multi-h CPM schemes using different approaches as in [46] and in [47].
The most used decomposition of the CPM however, is probably the linear decomposition that was initially introduced by Laurent in 1986 for the binary schemes [48] and later extended to the multilevel case in 1995 by Mengali and Morelli [49]. The main idea of this extension is to express the M-ary data sequence $\mathbf{a}$ in terms of binary subsequences and then use Laurent's decomposition .
The linear decomposition makes it possible to interpret the CPM as a sum of Pulse Amplitude Modulated (PAM) components which enables the derivation of efficient low complexity receivers. The signal $s(t, \mathbf{a})$ of the Equation 1.12 is decomposed as [49]:

$$s(t, \mathbf{a}) = \sqrt{\frac{2E_s}{T_s}} \sum_{k=0}^{K_T-1} \sum_{i=0}^{N-1} \alpha_{k,i} h_k(t - iT_s) \tag{1.19}$$

with $K_T = Q^P(2^P - 1)$ and $Q = 2^{L-1}$. As for P, it is the integer that verifies :

$$2^{P-1} < M \leq 2^P \tag{1.20}$$

If M is a power of 2, then $P = \log_2(M)$.
The functions $h_k(t)$ are called the linear components and the terms $\{\alpha_{k,i}\}_{\substack{0 \leq k \leq K_T-1 \\ 0 \leq i \leq N-1}}$ are called the pseudo symbols. They are respectively given by:

$$h_k(t) = \prod_{l=0}^{P-1} c_{d_{j,l}}^{(l)}(t + e_{j,l}^{(m)} T_s) \tag{1.21}$$

$$\alpha_{k,i} = \prod_{l=0}^{P-1} b_{d_{j,l}, i - e_{j,l}^{(m)}}^{(l)} \tag{1.22}$$

Table 1.2 – Pulse duration of the components $h_k(t)$

Components	**Duration**
first component	$L+1$
next 2^P-2 components	L
next $(2^P-1)^2$ components	$L-1$
next $2^P(2^P-1)^2$ components	$L-2$
next $2^{2P}(2^P-1)^2$ components	$L-3$
.	.
.	.
last $2^{(L-2)P}(2^P-1)^2$ components	1

The analytical expressions of $h_k(t)$ and $\{\alpha_{k,i}\}$ and the explanation of all the terms can be found in the Appendix B. In short, the type of frequency pulse $g(t)$ and the modulation index h are the main factors that control the linear component's shapes while the pseudo symbols are dependent on the symbols sequence **a**.
By analysing the obtained components $h_k(t)$, we get some interesting results. First, these components have different duration lengths as showed by Laurent in [48] for the binary case and by Mengali and Morelli in [49] for multilevel case and presented in Table 1.2.

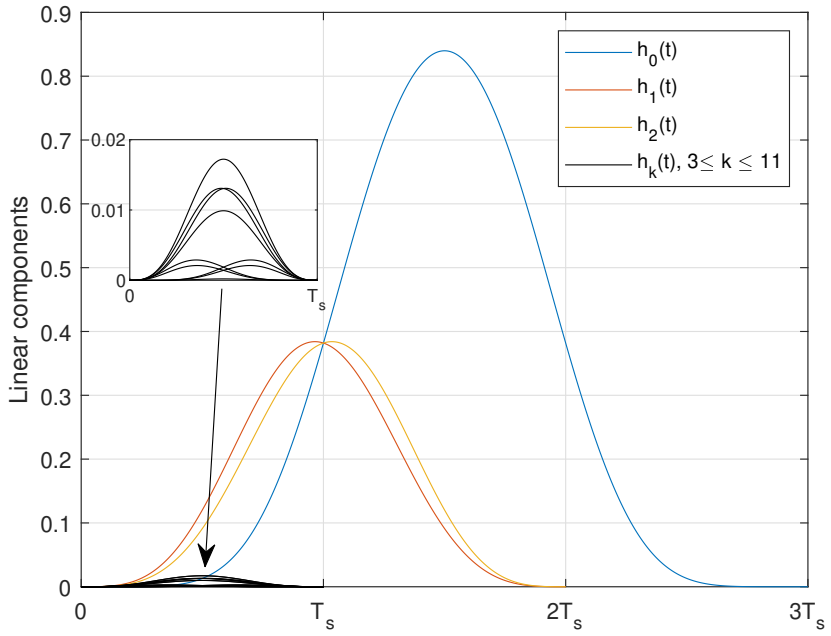

Figure 1.8 – Linear components of the Quaternary 2RC with $h = 0.25$

Second, the energy distribution between all these components is not uniform since most of it is conveyed within the first few components (generally, the first $L+1$ components at most convey almost 99% of the signal energy). This allows for the derivation of some low complexity receivers since the signal at the reception could be approximated by these few components only. For some CPM formats, approximating the signal to only the first component is sufficient as it is the case for the GMSK scheme.
Figure 1.8 plots the linear components of the Quaternary CPM scheme 2RC with $h = 0.25$. In this figure, we can notice that from the twelve components that compose this CPM scheme, only the first three components actually matters and the rest can be neglected. In Figure 1.9, we took the same scheme and plotted the real part alongside the phase trajectory of the exact signal against its linear approximation using only the first 3 main components presented in Figure 1.8.

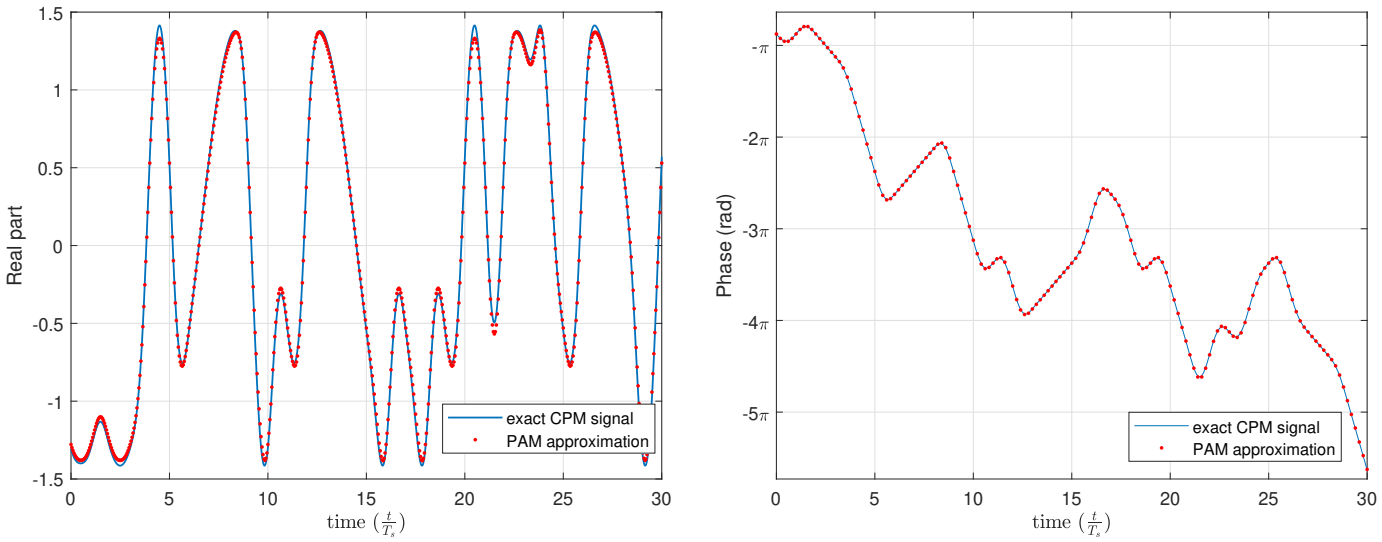

(a) Real part of the signal

(b) Phase of the signal

Figure 1.9 – Comparison between the exact signal of the Quaternary 2RC with $h = 0.25$ and its linear approximation using only the first 3 main components, in terms of real signal part and phase trajectory

From this example, we can see that the signal generated using the 3 main components makes for a very good approximation of the signal and especially its phase trajectory. This approximation highly simplifies the receiver structure since signal detection can be done using filters matched to only main pulses as we will see later in the next chapter.

1.2.4 Coherent detection

After the CPM signal description, the next step is to present how to actually demodulate it and detect the information sequence. In this section, we will present the coherent mode and in the next section the non coherent mode.
Coherent detection refers to detection mode where all signal and channel parameters are perfectly known to the receiver. Since we are interested in the Satellite IoT application, the first step in deriving the detection strategy is to consider the Gaussian channel since it is the most commonly used model for this type of communications and then gradually add various impairments in order to polish the transmission model and make it closer to the practical one.
Hence, for coherent detection, we assume that the CPM signal is transmitted over a Gaussian channel. The equivalent baseband received signal, denoted by $r(t)$, is given by:

$$r(t) = s(t, \mathbf{a}) + n(t) \tag{1.23}$$

with $n(t)$ being the realization of a zero-mean wide sense stationary complex circularly symmetric Gaussian noise, independent of the signal, and with double-sided power spectral density $2N_0$ over the bandwidth of $s(t, \mathbf{a})$.
Optimum coherent detection of the received CPM signal is done using the Maximum Likelihood Sequence Detector (MLSD). This receiver selects the most likely transmitted signal, given the received waveform $r(t)$. In other words, the receiver tries to find the transmitted signal $s_i(t)$ that maximizes the conditional probability $p(s_i|r)$. Maximizing that probability in the case of the CPM, with i.i.d information data is equivalent to finding the sequence $\widehat{\mathbf{a}}$ minimizing the Euclidean distance between $s(t, \widehat{\mathbf{a}})$ and the received signal $r(t)$ which is defined by:

$$\widehat{\mathbf{a}} = \arg\min_{\tilde{\mathbf{a}}} \|r(t) - s(t, \tilde{\mathbf{a}})\|^2 \tag{1.24}$$

Taking into account the constant envelope of the CPM, the previous detection criterion is equivalent to maximizing the correlation between the two signals, i.e.:

$$\widehat{\mathbf{a}} = \arg\max_{\tilde{\mathbf{a}}} \left(\Re \left(\int r(t) s^*(t, \tilde{\mathbf{a}}) dt \right) \right) \tag{1.25}$$

where $(.)^*$ is the complex conjugate and $\Re(.)$ is the real part. This means that we now have to calculate the correlation between the received signal and all possible transmitted sequences. In practice, it is not feasible due to the large number of possible sequences which increases exponentially with the sequence length. We can solve this problem thanks to the Viterbi algorithm [50] running over the trellis of the CPM.

The branch metric is the correlation between the portion of the received signal at a symbol interval $[nT_s, (n+1)T_s)$ and a possible generated signal at the receiver, it is defined by:

$$\delta_n(\tilde{a}) = \Re\left(\int_{nT_s}^{(n+1)T_s} r(t)s^*(t,\tilde{a})dt\right) \tag{1.26}$$

The Viterbi algorithm is based on the recursive computation of the accumulated metric at each state. In Figure 1.10, we illustrate the Viterbi algorithm on an example of trellis section. For every branch, we compute the metric given by Equation 1.25 and add it to the accumulated metric of the previous state.

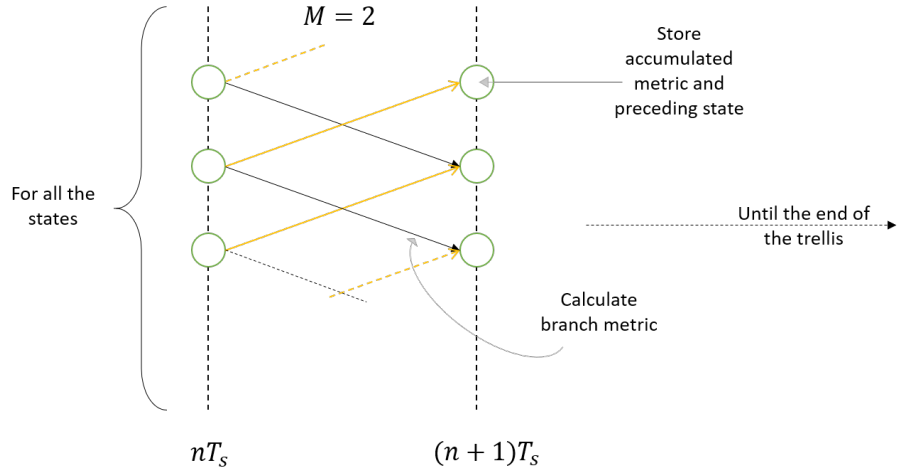

Figure 1.10 – Viterbi algorithm on a trellis section

When two branches coincide, we keep the branch with the highest accumulated metric. At the end, the decision is taken by selecting the sequence $\hat{\mathbf{a}}$ yielding the maximum correlation.
It is worth to mention that coherent detection of CPM can also be done using the BCJR algorithm [51], but in this work we mainly focused on the Viterbi algorithm.

1.2.5 Non coherent detection of CPM

In any type of wireless communications, signals are generally received with phase shifts. This is due to the time delay of the propagation of the signal in the first place. The second reason is the use of 2 local oscillators (LO) which are not phase synchronized. Phase Locked Loops (PLL) may solve this issue but both at the transmitting and the receiving side, LOs used may exhibit poor phase or frequency stability which leads to phase synchronization problems. The uncertainty of the phase of the received signal transmitted over a Gaussian channel can thus be modeled as :

$$r(t) = s(t,\mathbf{a})e^{j\psi} + n(t) \tag{1.27}$$

where ψ is a random phase and that is supposed to be uniformly distributed in $[0, 2\pi)$ and $n(t)$ is the same noise term from Equation 1.23.
Detection of such received signal without preliminary estimation of ψ is called *non coherent detection*. Study of the non coherent case is also interesting in the sense that it can a priori work without phase synchronization circuits which may leads to "simpler" receivers.

1.2.5.1 Non coherent sequence detection

Starting from the posterior probability of a signal knowing a received one and averaging over the phase parameter in the computation, the non coherent detection strategy is given by [52]:

$$\widehat{\mathbf{a}} = \arg\max_{\widehat{a}} \left\{ \log I_0 \left(\frac{1}{N_0} \left| \int_{T_0} r(t) s^*(t, \tilde{\mathbf{a}}) dt \right| \right) - \frac{1}{2N_0} \int_{T_0} |s(t, \tilde{\mathbf{a}})|^2 dt \right\} \tag{1.28}$$

Details on how to derive this likelihood function can be found in [52]. This detection strategy refers to *Non coherent Sequence Detection* (NSD) and it applies to any modulation. The development of Equation (1.28) for CPM modulation has been presented in [10].
The authors in [10] uses Laurent's decomposition in order to simplify the detection problem and then switch to the sampled model of the signal at the rate $\frac{1}{T_s}$ since one sample per symbol proves to be sufficient statistics for detection [12]. By doing so, the signal is processed by filters adapted to the principal components of the decomposition. The samples in the set $\mathbf{x}_n = (x_{0,n}, x_{1,n}, ..., x_{K-1,n})^T$ are given by :

$$x_{k,n} = r(t, \mathbf{a}) \otimes h_k(-t)|_{t=nT_s} \tag{1.29}$$

This causes both ISI and the resulting noise samples to be correlated, hence the need to perform a whitening procedure transforming $\mathbf{x}_n$ into new *whitened* samples $\mathbf{z}_n$. These samples are then used for detection and with the approximation $\log I_0(x) \simeq x$, the likelihood function becomes:

$$\Gamma_N(\tilde{\mathbf{a}}) = \left| \sum_{k=0}^{K_T-1} \sum_{i=0}^{N-1} z_{k,i} \tilde{y}^*_{k,i} \right| - \frac{1}{2} \sum_{k=0}^{K_T-1} \sum_{i=0}^{N-1} |\tilde{y}_{k,i}|^2 \tag{1.30}$$

where $\mathbf{y}_n$ are the samples afters noise whitening and corresponding to the signal contribution. Deriving an incremental metric to maximize this function involves prohibitive complexity since it increases in size with time. Thus, the authors in [53] propose the truncation of this metric to only a fixed number of last observations. Then, a trellis structure is defined based on the truncated metric and a Viterbi algorithm is used to search for the sequence that maximizes the likelihood function.
Figure 1.11 shows the architecture of the NSD receiver for CPM. The performance of this receiver compared to the coherent one is presented in Figure 1.12 for the GMSK scheme.

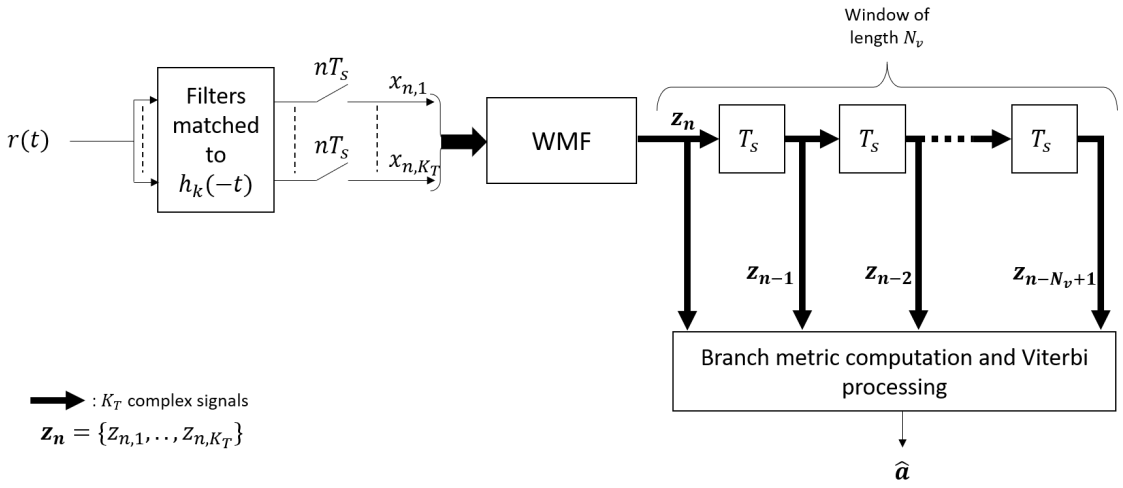

Figure 1.11 – NSD receiver for CPM presented in [10]

We can see in Figure 1.12 the influence of the truncation window on the detection performance. Performance loss compared to the coherent detector is less than 1 dB for a window of 5 symbols. The performance of NSD receiver approaches even more that of the coherent receiver when a larger window is used.

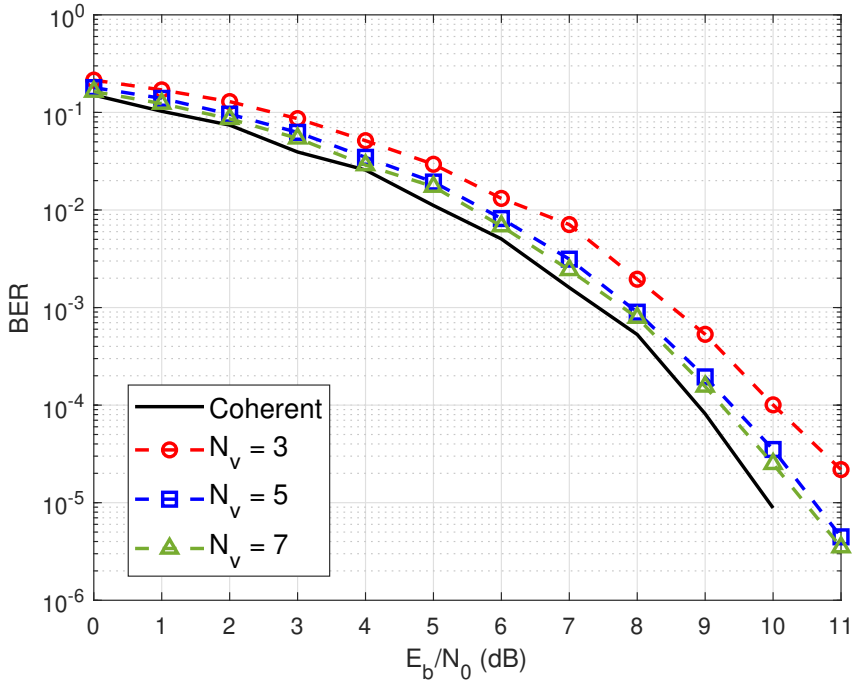

Figure 1.12 – Performance of NSD receiver for the GMSK for different values of the estimation window compared to coherent detector

1.2.5.2 Differential detection

The differential approach in general for any reception technique is to combine the received signal with a delayed version of itself (often multiply one by the complex conjugate of another) and then use the resultant signal for the detection. This process simplifies the detection problem by eliminating the phase shift. The major drawback of the differential approach however, is the increased noise in the resultant signal.
Most common differential approach with CPM is the conventional use of one symbol delay since it can *simplify* the detection rule. The idea as presented in [54] is that when using one symbol delay, we can eliminate the memory effect in the obtained signal. This makes the decision on the transmitted symbol dependent only on one symbol. The polar representation of $r(t)$ is given by :

$$r(t) = A(t)e^{j(\theta(t,\mathbf{a})+\eta(t))} \tag{1.31}$$

where $A(t)$ is the time-varying signal envelope due to signal distortion and $\eta(t)$ is phase noise. Using this form, the differential signal $R(t)$ is given by :

$$\begin{aligned} R(t) &= \frac{r(t)r^*(t-T_s)}{2} \\ &= \frac{A(t)A(t-T_s)}{2} e^{j(\Delta\theta(t,T_s,\mathbf{a}))} \end{aligned} \tag{1.32}$$

where the phase difference $\Delta\theta(t, T_s, \mathbf{a})$ is given by :

$$\Delta\theta(t, T_s, \mathbf{a}) = \theta(t, \mathbf{a}) - \theta(t - T_s, \mathbf{a}) + \eta(t) - \eta(t - T_s) \tag{1.33}$$

$R(t)$ is then sampled at instants $t_n = t_0 + nT_s$ when the ensemble of phase differences has an open eye which means at multiples of T_s [14]. The receiver then decides on the transmitted symbol at t_0 based on the sign of the real quantity of $R(t_n)$ or equivalently $\sin(\Delta\theta(t_n, T_s, \mathbf{a}))$. For the binary case, the decision rule is $\widehat{a} = 1$ if $\sin(\Delta\theta(t_n, T_s, \mathbf{a})) > 0$ and $\widehat{a} = -1$ if $\sin(\Delta\theta(t_n, T_s, \mathbf{a})) \leq 0$.

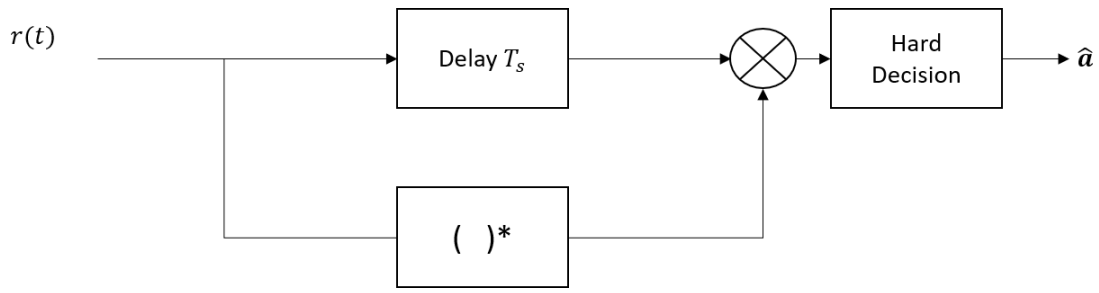

Figure 1.13 – Differential receiver architecture presented in [15]

For the multilevel case, the phase interval is divided into different decision regions depending on the symbol alphabet and the *a priori* probabilities and then the symbol is decided accordingly [15]. Figure 1.13 depicts the architecture of the differential receiver as presented in [15] and its performance for the GMSK scheme with $BT_s = 1$ is presented in Figure 1.14.

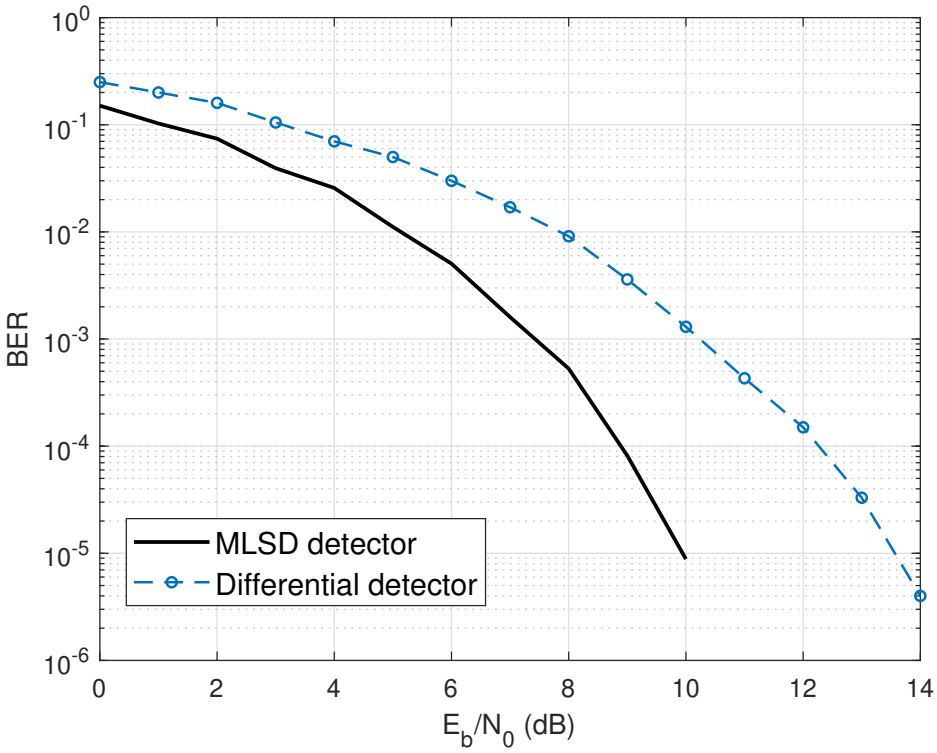

Figure 1.14 – Performance of the differential receiver from [15] for GMSK with $BT_s = 1$

Some CPM schemes can be approximated by only one main component in the linear decomposition and notably, binary schemes with modulation index $h = 0.5$. Thus, the author in [55] takes advantage of this and tries to apply the same differential detection strategy of BPSK signals with these schemes.

The use of multiple symbols delay is also an alternative differential detection approach. In [56], the author considers the TFM scheme [57] and combines a set of multiple differential signal versions with different delays to define a detection metric and in [13], he generalizes his approach to any CPM scheme. Another multiple symbols differential reception strategy is presented in [58] for the GMSK scheme and also in [59] but for mobile communications. In general, when using multiple symbols delay, the resultant signal may exhibit a trellis structure but we will see this thoroughly in Chapter 3.

1.3 Conclusion

In this chapter, we first presented some key elements of the LEO satellite link notably the Doppler profile which we will need later. Second, we described the CPM waveform and some relevant coherent and non coherent detection techniques. We also illustrated the performance of these detectors on a the GMSK which is a very common CPM format in the case of Gaussian channel.
The next step is to consider the Doppler effect in the channel. If the Doppler is not taken into account in the detection metric, the error rate may severely increase. In the next chapter, we forcus on non coherent detection. Based on the non coherent ML criterion described in this chapter, we will try to take the Doppler shift into account.

Chapter 2

Non coherent CPM detection with Doppler estimation

Contents

The power constraint in the context of Satellite Internet of Things (Satellite IoT) imposes the use of short frames. This can be a problem for the detection where the signal is highly affected by the presence of Doppler since pilot sequences in the frame might be too short too help in the frequency estimation problem or might be even omitted for more spectral efficiency. In this chapter, our objective is to conceive a CPM detector able to withstand the high Doppler shift that is encountered in a blind way. We also have to keep in mind the phase uncertainties at the reception as well. Therefore, we start from the non coherent detection criterion applied to CPM and we couple it with the generalized likelihood principle to derive two possible detectors; the first uses the linear decomposition of the CPM and the second uses the exact expression of the signal.

2.1 Detection strategy

To begin with, we start by considering a constant Doppler shift. This assumption will later be relaxed. In presence of a constant Doppler shift f_D, the received signal given by Equation (1.27) translates into :

$$r(t) = s(t, \mathbf{a})e^{j(2\pi f_D t + \psi)} + n(t) \tag{2.1}$$

Starting from the non coherent sequence detection criterion that was presented in the first chapter, the detection strategy proposed is then based on the generalized maximum-likelihood [11] that we shall recall now. Let T_0 be the observation interval of the signal $r(t)$ and let $\mathcal{A}$ designate the set of possible symbol sequences, $\mathcal{F}$ the variation interval of f_D and I_0 the modified first-order Bessel function.
The generalized maximum-likelihood method [11] is used for a blind Doppler shift estimation in conjunction with symbol detection and consists in maximizing the following cost function

$$\Gamma(\tilde{\mathbf{a}}, \widetilde{f_D}) = \log \mathrm{I}_0 \left(\frac{1}{N_0} \left| \int_{T_0} r(t, \mathbf{a}) s^*(t, \tilde{\mathbf{a}}) e^{-j2\pi \widetilde{f_D} t} dt \right| \right) - \frac{1}{2N_0} \int_{T_0} |s(t, \tilde{\mathbf{a}})|^2 dt \tag{2.2}$$

over $\mathcal{A} \times \mathcal{F}$.
This is equivalent according to this method to finding the sequence $\tilde{\mathbf{a}}$ that maximizes Γ with respect to $\tilde{\mathbf{a}}$ and an estimation of f_D based on $\tilde{\mathbf{a}}$. Mathematically speaking, we are looking for the sequence $\tilde{\mathbf{a}}$ verifying :

$$\max_{\tilde{\mathbf{a}} \in \mathcal{A}} \Gamma(\tilde{\mathbf{a}}, \widehat{f}_D(\tilde{\mathbf{a}})) \tag{2.3}$$

with

$$\widehat{f}_D(\tilde{\mathbf{a}}) = \arg \max_{\widetilde{f_D} \in \mathcal{F}} \left| \int_{T_0} r(t) s^*(t, \tilde{\mathbf{a}}) e^{-j2\pi \widetilde{f_D} t} dt \right|. \tag{2.4}$$

In the following, we apply criterion (2.3) according to two alternative algorithms. The first (denoted A), based on a linear decomposition of the CPM, is a combination of the methods described in [10] (denoted NSD algorithm) and [9]. The second (called B) is a sub-optimal algorithm for deriving the criterion directly from (1.12).

2.1.1 Receiver A based on the linear decomposition of CPM

This receiver combines the non-coherent CPM detection algorithm [10] with the Doppler estimation and joint detection algorithm applied to a linear modulation [9]. To this end, we consider the linear decomposition of the CPM modulation presented in Chapter 1 and given by equation (1.19) where we also consider K_c the number of principal components only.
The receiver consists of a cascade of a filter bank where filters are adapted to $h_k(t)$, followed by a sampler at period T_e, and a whitening filter. T_e should be small enough to assume that the samples are a sufficient statistic [12]. However, for a moderate frequency offset ($f_D T_s \ll 1$),

$T_e = T_s$ is small enough.
The sampler outputs are given by:

$$x_{k,n} = r(t, \mathbf{a}) \otimes h_k(-t)|_{t=nT_s} \simeq s_{k,n} e^{j(2\pi f_D n T_s + \phi)} + \eta_{k,n}$$

where

$$s_{k,n} = \sum_{m=0}^{K_c-1} \sum_i \alpha_{m,i} p_{m,k}((n-i)T_s), \tag{2.5}$$

with $p_{m,k}(t) = h_m(t) \otimes h_k(-t)$ and $\eta_{k,n} = \eta(t) \otimes h_k(-t)|_{t=nT_s}$. We introduce the notation $\mathbf{x}_n = (x_{0,n}, x_{1,n}, ..., x_{K-1,n})^T$ and define $\mathbf{s}_n$, $\boldsymbol{\alpha}_n$ and $\boldsymbol{\eta}_n$ likewise. We will also use the discrete impulse response matrices $\mathbf{P}_n = [p_{i,j}(nT)]$ for $i, j = 0, 1, ..., K-1$. With these notations, the observation vector reads:

$$\mathbf{x}_n \simeq e^{j(2\pi f_D n T + \phi)} \sum_{l=-L_w}^{L_w} \mathbf{P}_l^T \boldsymbol{\alpha}_{n-l} + \boldsymbol{\eta}_n, \tag{2.6}$$

where L_w is a parameter that depends on L.
As the noise samples $\eta_{k,n}$ are correlated, a multidimensional whitening filter (WMF) is implemented [10]. It is specified by the sequence of matrices $\{\mathbf{W}_l\}_{0 \le l \le L_w}$. The WMF output observation vector, denoted by $\mathbf{z}_n$, is given by:

$$\begin{aligned} \mathbf{z}_n &= \sum_{l=0}^{L_w} \mathbf{W}_l \mathbf{x}_{n-l} \\ &= e^{j(2\pi f_D n T_s + \phi)} \sum_{l=0}^{L_w} \mathbf{W}_l \mathbf{s}_{n-l} e^{-j2\pi l f_D T_s} + \mathbf{w}_n, \end{aligned} \tag{2.7}$$

where $\mathbf{w}_n = \sum_{l=0}^{L_w} \mathbf{W}_l \boldsymbol{\eta}_{n-l}$.
Going back to the detection criterion, we apply two approximations. The first one is to consider $\log I_0(x) \simeq x$. The second one depends on the context: we assumes that $f_D T_s$ is small and that $e^{-j2\pi l f_D T_s} \simeq 1$ in the expression (2.7) of $\mathbf{z}_n$. Given a sequence $\tilde{\mathbf{a}}$ of symbols in $\mathcal{A}$, we define $\tilde{\mathbf{s}}_n$ with (2.5) and finally $\tilde{\mathbf{y}}_n = \sum_{l=0}^{L_w} \mathbf{W}_l \tilde{\mathbf{s}}_{n-l}$ which are the samples that will be used for the frequency estimation and for detection as well.
The likelihood function calculated in the joint symbol detection and Doppler estimation algorithm is therefore given by:

$$\Gamma_N(\tilde{\mathbf{a}}, \widehat{f}_D(\tilde{\mathbf{a}})) = \left| \sum_{k=0}^{K_c-1} \sum_{n=0}^{N-1} z_{k,n} \tilde{y}_{k,n}^* e^{-j2\pi n \widehat{f}_D(\tilde{\mathbf{a}}) T_s} \right| - \frac{1}{2} \sum_{k=0}^{K_c-1} \sum_{n=0}^{N-1} |\tilde{y}_{k,n}|^2. \tag{2.8}$$

If the second approximation does not hold, the samples $\tilde{\mathbf{y}}_n$ can not be defined properly and therefore, detection using this model can not be carried over. One solution is to employ over-sampling, but we will discuss that in the next detector.
Maximizing (2.8) involves prohibitive complexity in practice. We adapt the procedure used in [9] to deal with linear modulations. A Viterbi algorithm is applied associated with a windowing of size N_v for the detection of symbols, a windowing of size $N_D \geq N_v$ for the blind estimation of the Doppler shift and an approximation of $\Gamma_N(\tilde{\mathbf{a}}, \widehat{f}_D(\tilde{\mathbf{a}}))$ by $\Delta_N(\tilde{\mathbf{a}})$ which is calculated in an iterative way as follows:

$$\Delta_n(\tilde{\mathbf{a}}_n) = \Delta_{n-1}(\tilde{\mathbf{a}}_{n-1})) + \lambda_n(\tilde{\mathbf{a}}_\mathbf{n}) \tag{2.9}$$

with the branch metric being

$$\begin{aligned}
\lambda_n(\tilde{\mathbf{a}}_\mathbf{n}) &= \left| \sum_{k=0}^{K_c-1} \sum_{i=0}^{N_v-1} z_{k,n-i} \tilde{y}^*_{k,n-i} e^{-j2\pi(n-i)\widehat{f}_D(\tilde{\mathbf{a}}^n_{n-N_D}))T_s} \right| \\
&- \left| \sum_{k=0}^{K_c-1} \sum_{i=1}^{N_v-1} z_{k,n-i} \tilde{y}^*_{k,n-i} e^{-j2\pi(n-i)\widehat{f}_D(\tilde{\mathbf{a}}^n_{n-N_D}))T_s} \right| \\
&- \left| \sum_{k=0}^{K_c-1} \tilde{y}_{k,n} \right|^2 .
\end{aligned}$$

The state at time $n-1$ is defined by the vector $\left(\tilde{\mathbf{y}}^T_{n-1} \quad \dots \quad \tilde{\mathbf{y}}^T_{n-N_v+1}\right)^T$, which implies a total of $S = M^{N_v+L_w-1}$ states. As in [9], a *per-survivor processing* (PSP) approach enables to estimate $\widehat{f}_D(\tilde{\mathbf{a}}^n_{n-N_D})$ based on $\tilde{a}_n$ and the partial sequence $\tilde{\mathbf{a}}^{n-1}_{n-N_D} = (\tilde{a}_{n-1} \ \dots \ \tilde{a}_{n-N_D})$ associated to the surviving path at state level at time $n-1$.

In Figure 2.1, we can see the windowing principle on a trellis example. Here, the dark blue section designate the current symbol to be decided. The metric $\lambda_n(\tilde{\mathbf{a}}_\mathbf{n})$ is calculated based on this symbol and the symbols included in the light blue window. However, the symbols needed to do the Doppler shift estimation $\widehat{f}_D(\tilde{\mathbf{a}}^n_{n-N_D})$ are stored at each current state based on previous decisions made following the PSP approach given a window designated by the yellow section. Metrics are therefore calculated for the red and green paths and then the decision is made. The decoding is then continued by sliding these windows by one symbol until the end of trellis.
Calculation of $\lambda_n(\tilde{\mathbf{a}}_\mathbf{n})$ implies that we have to wait until the N_v^{th} symbol in order to start the decoding. One question can be asked here regarding the initiation phase for the Doppler shift estimation in the case $N_D > N_v$ as indicated in Figure 2.1. Here, the solution we used is to do the Doppler shift estimation on just a window of length N_v (since symbols on this window are the only symbols available so far) and then we extend the length of this window to $N_v + 1$ based on the first decided symbol. We then do the estimation on the extended window and we

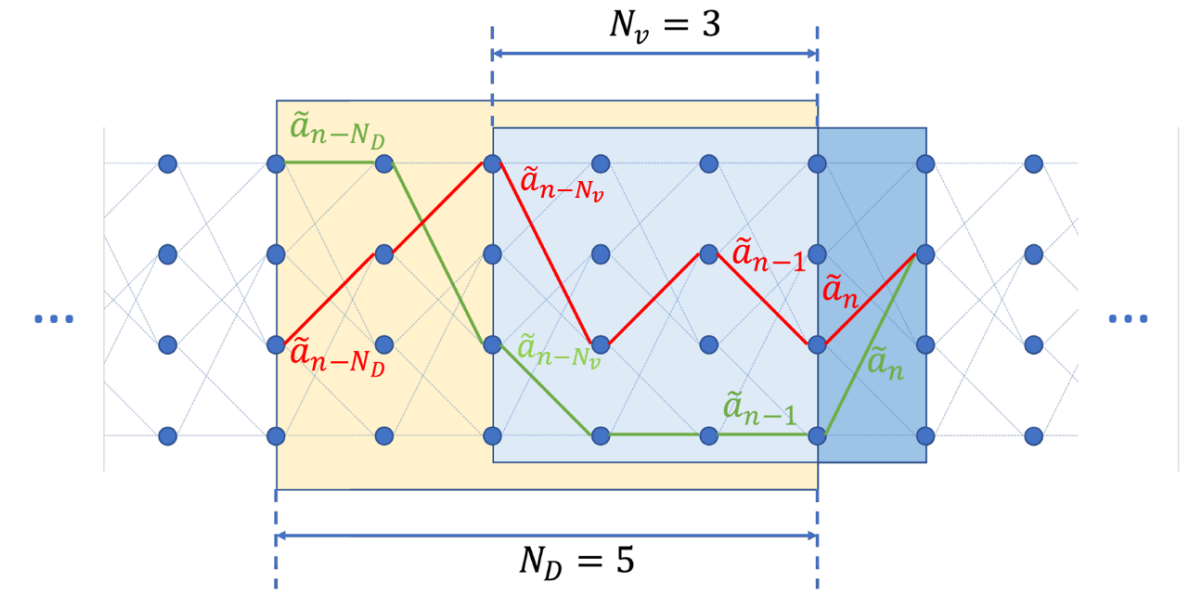

Figure 2.1 – Windowing principle of NSD with Doppler shift estimation technique on a trellis example with $N_v = 3$ and $N_D = 5$

continue therefore the same step up until we reach the desired length N_D.

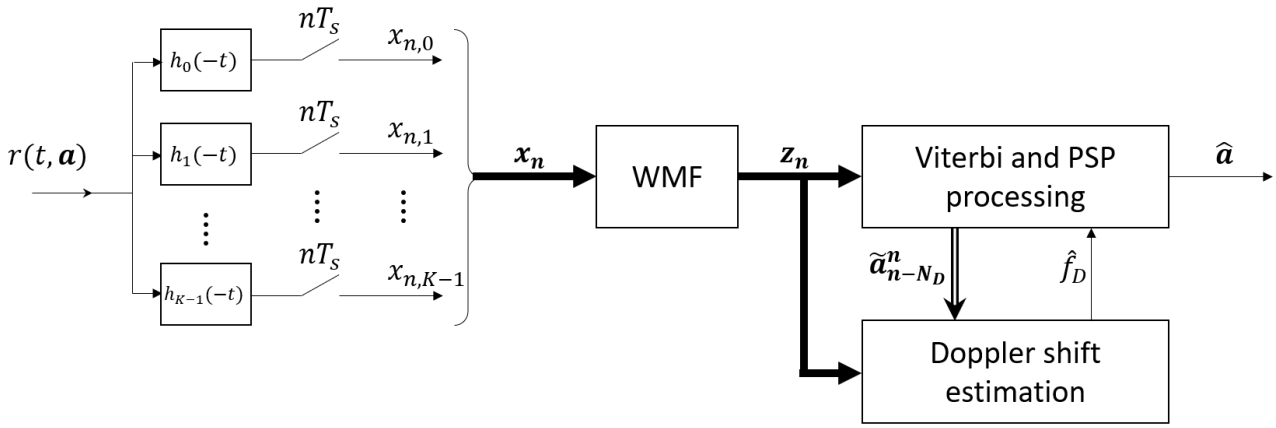

Figure 2.2 – Detector A architecture

To summarize, the detector A consists of a bank of filters matched to the principal components of the linear decomposition of the signal, followed by a sampler at the symbol rate and then a multidimensional whitening filter whose outputs are used as the input of the Viterbi processor as depicted in Figure 2.2.

2.1.2 Receiver B based on the exact expression of CPM

The purpose of this receiver is to keep performing at much higher frequency offset rates since the application we are aiming for could present substantial Doppler range. Considering the constant envelope of the CPM waveform, the likelihood function (2.3) becomes:

$$\Lambda(\tilde{\mathbf{a}}) = \Gamma(\tilde{\mathbf{a}}, \widehat{f}_D(\tilde{\mathbf{a}})) = \left| \int_{T_0} r(t, \mathbf{a}) s^*(t, \tilde{\mathbf{a}}) e^{-j2\pi \widehat{f}_D(\tilde{\mathbf{a}})t} dt \right|$$

Let $t_k = kT_s$ and let $v_n(t, \tilde{\mathbf{a}}) = r(t, \mathbf{a}) e^{-j2\pi \widehat{f}_D(\tilde{\mathbf{a}}_{n-N_D}^n)t}$. To reduce the complexity, we apply the iterative approximation of $\Lambda(\tilde{\mathbf{a}})$ under the same principles of windowing and of definition of the cumulative and branch metrics:

$$\lambda_n(\tilde{\mathbf{a}}) = \Gamma_n(\tilde{\mathbf{a}}) - \left| \int_{(n-N_v)T_s}^{(n-1)T_s} v_n(t, \mathbf{a}) s^*(t, \tilde{\mathbf{a}}) dt \right| \tag{2.10}$$

where $\Gamma_n(\tilde{\mathbf{a}}) = \left| \int_{t_{n-N_v}}^{t_n} v_n(t, \tilde{\mathbf{a}}) s^*(t, \tilde{\mathbf{a}}) dt \right|$. With the same reasoning, the search for the sequence maximizing the likelihood function (2.2) is done using a Viterbi algorithm executed on a trellis whose states at time n correspond to all the possible realizations of $s(t, \tilde{\mathbf{a}}_{n-N_v+1}^n)$. The estimation $\widehat{f}_D(\tilde{\mathbf{a}}_{n-N_D}^n)$ is done as for receiver A using the PSP approach on a window of length N_D.
The development of the first term of the equation (2.10) leads to:

$$\Gamma_n(\tilde{\mathbf{a}}) = \sqrt{\frac{2E_s}{T_s}} \left| \sum_{m=0}^{N_v-1} \int_{t_{n-m-1}}^{t_{n-m}} v_n(t, \tilde{\mathbf{a}}) e^{-j\theta(t, \tilde{\mathbf{a}})} dt \right|. \tag{2.11}$$

The term depending on $\theta(t, \tilde{\mathbf{a}})$ in the interval $[t_{n-m-1}, t_{n-m}]$ can be simplified:

$$\theta(t, \tilde{\mathbf{a}}) = 2\pi h \sum_{u=0}^{n-m-1} \tilde{a}_u q(t - uT_s) = \Theta(t, \tilde{\mathbf{a}}) + \pi h \sum_{u=0}^{n-m-L-1} \tilde{a}_u \tag{2.12}$$

with

$$\Theta(t, \tilde{\mathbf{a}}) = 2\pi h \sum_{u=n-m-L}^{n-m-1} \tilde{a}_u q(t - uT_s) \tag{2.13}$$

By replacing (2.12) in (2.11), and after some straightforward calculations, we come up with:

$$\Gamma_n(\tilde{\mathbf{a}}) = \sqrt{\frac{2E_s}{T_s}} \left| \sum_{m=0}^{N_v-1} e^{-j\pi h \sum_{u=n-N_v-L+2}^{n-m-L-1} \tilde{a}_u} I_m(\tilde{\mathbf{a}}) \right| \tag{2.14}$$

with

$$I_m(\tilde{\mathbf{a}}) = \int_{t_{n-m-1}}^{t_{n-m}} v_n(t, \tilde{\mathbf{a}}) e^{-j\Theta(t, \tilde{\mathbf{a}})} dt \tag{2.15}$$

We deduce that the computation of $\lambda_n(\tilde{\mathbf{a}})$ only depends on $[\tilde{a}_{n-1}, .., \tilde{a}_{n-N_v-L+2}]$. The Viterbi algorithm therefore applies to a trellis with $S = M^{N_v+L-2}$ states (number of realizations of $[\tilde{a}_{n-1}, .., \tilde{a}_{n-N_v-L+2}]$).

Hence, the detector B is a series of integrators followed by envelope detectors which calculate

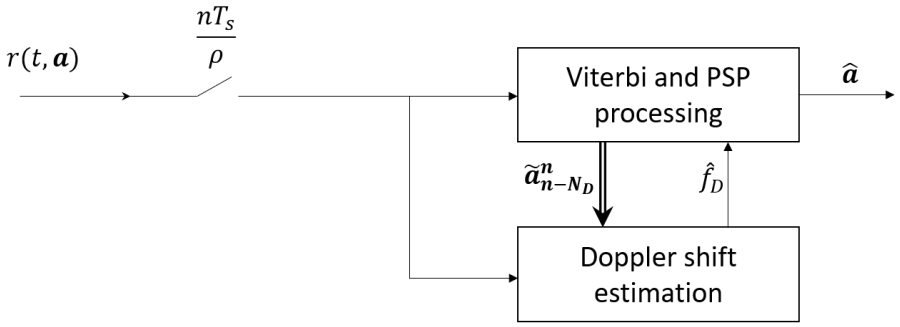

Figure 2.3 – Detector B architecture

the quantities that we will be using as an input of the Viterbi processor. The architecture of detector B is depicted in Figure 2.3.

2.2 Frequency estimation

An overview of the frequency estimation algorithm for PSK modulation can be found in [60]. While these algorithms are proposed for linear phase modulations, in particular for the PSK modulation family, we are interested only in the data-aided (DA) estimation model in which the modulation has been eliminated, so by using a DA operation on our CPM signal, we get the same estimation model and hence, the algorithms presented afterwards are easily applied to the CPM case to get $\widehat{f}_D(\tilde{\mathbf{a}}^n_{n-N_D})$.

The algorithm that we used is the same for both detectors A and B. The only difference is that in the first, we used one sample per symbol whereas for the second, we employed oversampling. Let (v_k) be the input samples sequence of the received signal for the frequency estimation block and let (c_k) be the hypothetical pilot sequence. The DA operation is given by :

$$u(k) = v_k c_k^* \tag{2.16}$$

where

$$\begin{cases} v_k = z_k \quad \text{and} \quad c_k = y_k, & \text{for Detector A} \\ v_k = r(k\frac{T_s}{\rho}, \tilde{\mathbf{a}}^n_{n-N_D}) \quad \text{and} \quad c_k = s(k\frac{T_s}{\rho}, \tilde{\mathbf{a}}^n_{n-N_D}), & \text{for Detector B} \end{cases} \tag{2.17}$$

The samples sequence $u(k)$ is the sequence used for the frequency estimation. The first algorithm presented is *Rife and Boorstyn* algorithm [61]. It is the algorithm that yields the maximum

likelihood estimate. The idea is that samples $u(k)$ after the DA operation will describe a sine wave at the frequency f_D and then the task is to estimate this frequency using a Fourier transform. Other algorithms are presented in [60] for the purpose of reducing the complexity. They are divided in two categories; *Least-Squared-Based* estimators and *Autocorrelation-Based* estimators. The main idea of the *Least-Squared-Based* estimators is that if we took the argument of samples $u(k)$, it can be considered as noisy samples of a straight line having a slope value $2\pi f_D T_s$. Then least squares method is used to estimate this slope. As for the *Autocorrelation-Based* estimators, the argument of the autocorrelation samples of the $u(k)$ samples is proportional to the frequency f_D and thus, using the mean or a weighted mean formula on these samples can lead to the desired estimate. For more details and analytic formulas on these algorithms, the reader can refer to [60] where a performance comparison between the algorithms is also presented.

2.3 Complexity estimation

We now propose to estimate the complexity of the two detectors. The complexity is assessed in terms of the number of trellis states (S), the number of multiplications for metric calculation (Q_M) per trellis section and the number of multiplications for Doppler Shift estimation per trellis section (Q_D). The complexity of the three detectors is summarized in the Table 2.1.

Table 2.1 – Comparison of the detectors in terms of complexity (number of states S, number of multiplications per trellis section for detection Q_M and number of multiplications per trellis section for Doppler estimation Q_D)

Label	Detector A	Detector B
S	$M^{N_v+L_w-1}$	M^{N_v+L-2}
Q_M	$(L_w+1)K_c^2 + N_v S M$	$\rho N_v S M$
Q_D	$\rho S(N_D+M-1) + MS\frac{N_{\text{FFT}}}{2}\log_2(N_{\text{FFT}})$	

Detector A based on Laurent's decomposition enables sampling at symbol time if the Doppler frequency shift remains moderate. The calculation of branch metrics amounts to $N_v M^{N_v+L_w}$ multiplications per trellis section, while the matched filtering involves $(L_w+1)K^2$ per trellis section.

In the case of detector B, the multiplications come solely from the branch metric calculations. The numerical calculation of the integral requires a discretization of the signal. Assuming it is done with ρ samples per symbol time, the total number of multiplications per trellis section is given by $\rho N_v M^{N_v+L-1}$.

Both detectors A and B use the Rife and Boorstyn [60] algorithm to blindly estimate the Doppler shifts. Its implementation uses *Fast Fourier Transform* (FFT) on a vector of ρN_D samples ($\rho = 1$ for detector A) obtained by multiplying the received signal with the complex conjugate of the signal reconstructed from the last N_D symbols using the PSP approach (amounting to $S\rho(N_D - 1) + MS\rho$ multiplications). Zero padding this vector up to N_{FFT} samples is used to increase the FFT resolution and thus the blind Doppler shift estimation resolution which affects the overall performance (amounting to $MS\frac{N_{\text{FFT}}}{2}\log_2(N_{\text{FFT}})$ multiplications).

2.4 Simulation results

In this paragraph, an evaluation in terms of simulated error rates is proposed for the two algorithms A and B. These performances will also be compared to differential detection presented in the previous chapter.

2.4.1 Performance with constant Doppler shift

In this section, bit error rates (BER) are estimated through Monte-Carlo simulations as a function of the ratio E_b/N_0 where E_b denotes the average information bit energy. To this aim, we take into account the overhead used for initialization and estimation in the calculation of E_b/N_0.
First we want to investigate the influence of window parameters N_v and N_D. To investigate the effect of the first one, we consider the case of absence of Doppler (or the same as if the Doppler shift is perfectly known to the receiver) since parameter N_v only influence the detection not frequency estimation. In such case, we have the same performance as in [10] since the problem becomes the same and $N_v = 5$ is shown there to be good enough. Then, to investigate the influence of N_D, we illustrate the error rate performance by considering the GMSK waveform with $BT = 0.25$ and $L = 2$ to transmit short frames of $N = 120$ symbols. The symbol duration is fixed to $T_s = 10^{-4}$s. We also consider small Doppler shift since in this case detector A and B should perform the same and fixed $N_v = 5$. The blind estimation of f_D used is the algorithm of Rife and Boorstyn [60]. For detector A, we proceed as in [53] by keeping only the first of the principal components resulting from the linearization of the GMSK leading to a one-dimensional whitening filter ($K_c = 1$) with $L_w = 2$. Figure 2.4 shows the obtained results only for detector A since the same impact of N_v and N_D is observed.

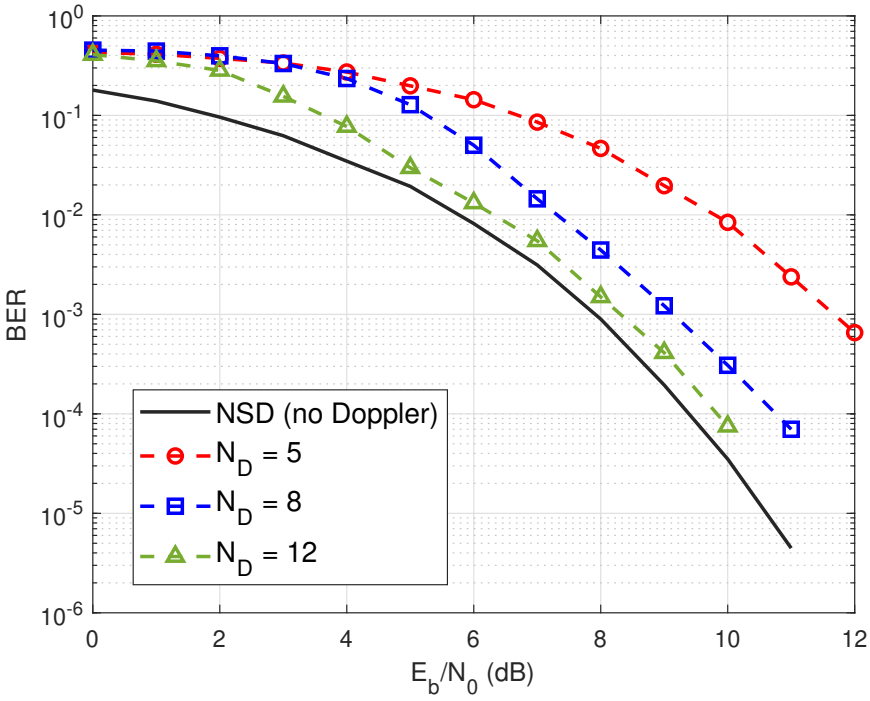

Figure 2.4 – Influence of N_D on the performance of detector A for GMSK with $N_v = 5$ and $f_D T_s = 0.01$

We can see that for frequency estimation, a window of $N_D = 8$ symbols presents a gain of almost 3 dB compared to a window of $N_D = 4$ symbols. This gain is only about 1 dB when we doubled again the size of the window to $N_D = 16$ symbols. Given these results and the increased complexity with size of the frequency estimation window, we choose to fix $N_D = 8$ as the best trade off between performance and complexity.

Next step is to compare the performance of detectors A and B in slightly increased Doppler orders. We start by considering the scheme 3RC with $h = 0.75$ in Figure 2.5. In this scheme, we also approximated the received signal by only its first principal components resulting from its linear decomposition with $L_w = 2$. For a small Doppler shift $f_D T_s = 0.075$, detectors A and B perform nearly the same with a loss of 1 to 1.5 dB compared to the NSD performance which correspond to the performance without any Doppler shift. When the Doppler shift is increased to $f_D T_s = 0.125$, the performance of detector A is degraded and a gap of 3 dB compared to the NSD is observed at a BER of 10^{-3}.

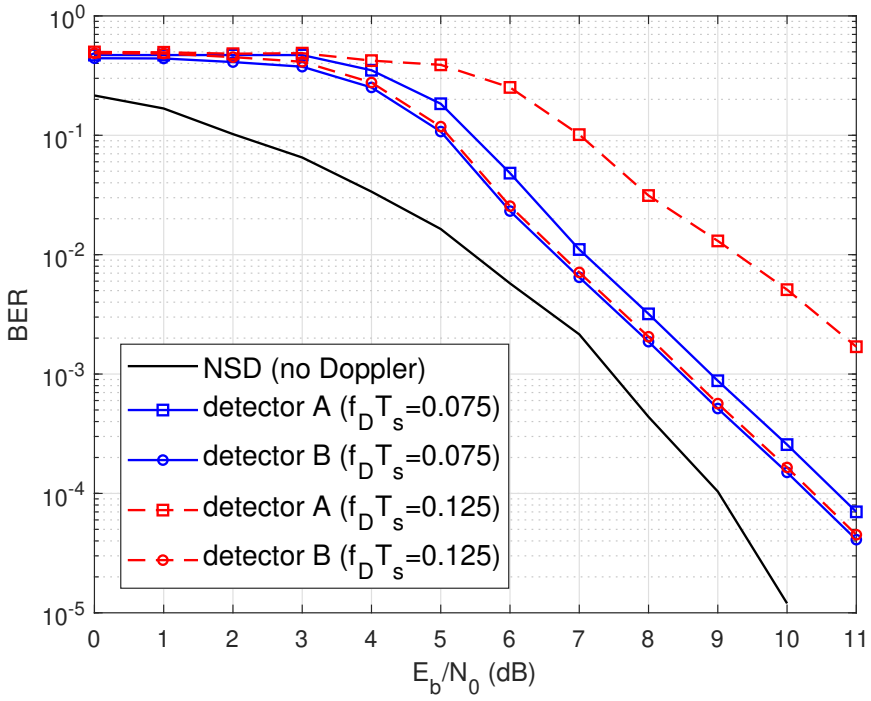

Figure 2.5 – BER comparison between detectors A ($\rho = 1$, $N_{\text{FFT}} = 32$) and B ($\rho = 8$, $N_{\text{FFT}} = 256$) for 3RC with $h = 0.75$, $N_v = 5$ and $N_D = 8$

For a multilevel scheme, we consider the Quaternary 2RC with $h = 0.25$. Again, for detector A, we proceed as in [53] by considering the first principal component and a second one which consist of an average of the next two since they are quite similar (see Figure 1.8). Therefore, the whitening filter is two-dimensional with $L_w = 1$ and N_v and N_D are kept the same. Simulation results are given in Figure 2.6.

This time we decreased a bit the Doppler orders. However, the same general behavior of both detectors is observed. For a small Doppler shift $f_D T_s = 0.05$, detectors A and B perform almost the same with a loss of 2 dB compared to the NSD performance and when the Doppler shift is increased to $f_D T_s = 0.1$, the performance of detector A is degraded and a gap of 2.5 dB compared to the NSD is observed at a BER of 10^{-3}. Indeed, when the Doppler shift increases, the assumption of sufficient statistics does not hold anymore. This is not the case with detector B whose performance is only limited by the capabilities of the Doppler shift estimation algorithm. In fact, with a perfect Doppler shift estimation, the detector B and NSD curves are superimposed.

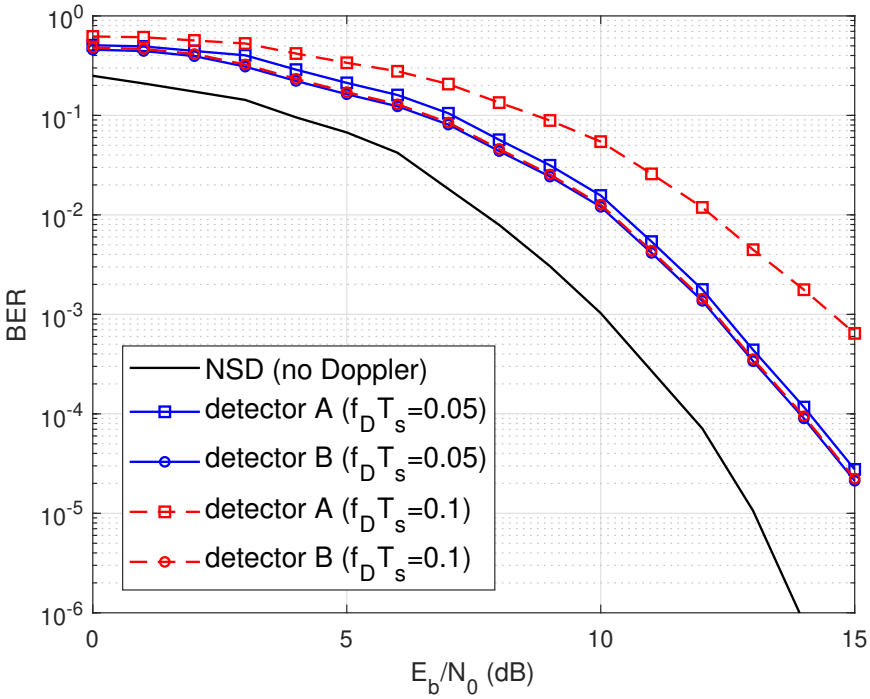

Figure 2.6 – Comparison of detectors A ($\rho = 1$, $N_{\text{FFT}} = 32$) and B ($\rho = 8$, $N_{\text{FFT}} = 256$) for Quaternary 2RC with $h = 0.25$, $N_v = 5$ and $N_D = 8$

2.4.2 Performance with variable Doppler shift

Although initially we made the assumption that the Doppler shift is constant, this could be relaxed for both detectors A and B since the usage of a sliding window to estimate the later all along the trellis enables the receivers to keep track of its variation provided that it does not vary so much across this window, a condition which is indeed met giving, not only, the Doppler rate profile presented in the first chapter, but also the fact that the size of the sliding window is relatively small (8 symbols) according to simulation results.
To assess the performance of detectors A and B in the case of variable Doppler, we consider the format 4RC with $h = \frac{2}{3}$. The size of the windows are kept the same with $N_v = 5$ and $N_D = 8$. In the simulation, we considered $f_D T_s = 0.05$ while also having a Doppler rate $f_R = 250$ Hz/s which again is the maximum theoretical rate encountered in our application.

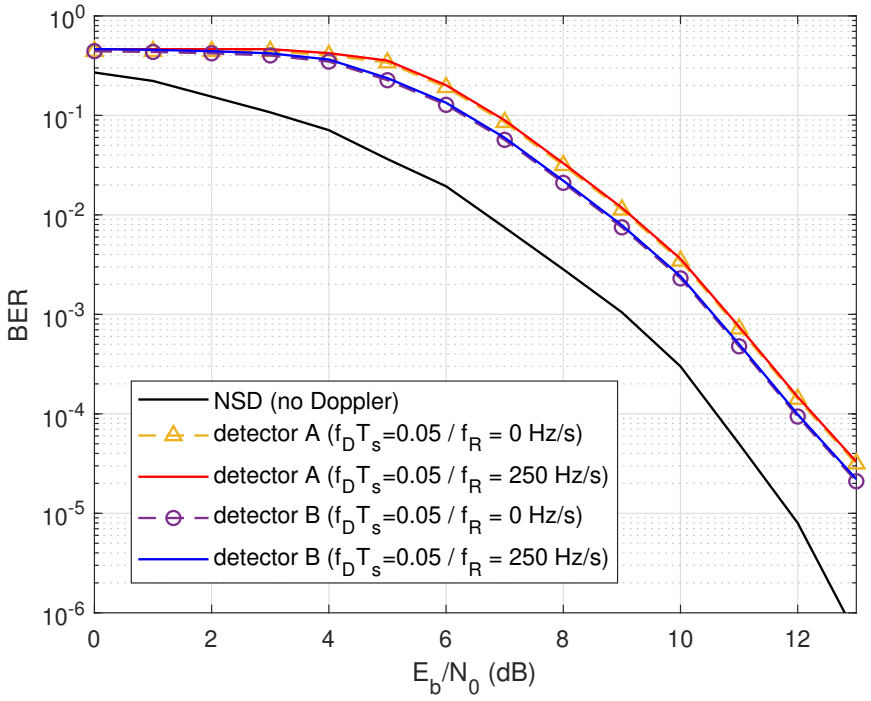

Figure 2.7 – BER comparison between detector A and B for 4RC with $h = \frac{2}{3}$ where $f_D T_s = 0.05$ in presence of Doppler rate $f_R = 250$ Hz/s with $N_v = 5$ and $N_D = 8$

We can see according to Figure 2.7 that even at the highest Doppler rate encountered, the performance of both detectors keeps exactly the same with no degradation. We can conclude that Doppler rate is not a problem for both detectors.

2.4.3 Performance limitation of the detectors

In developing the detector A, we worked under the assumption that the Doppler shift is moderate enough to simplify the problem and reduce the overall complexity. This assumption is necessary for both frequency estimation and sequence detection models. Therefore, detector A should theoretically keep performing as long as this assumption stands and this is what defines its performance limitation. As for detector B, since no approximations have been used, it is only limited by the performance of the frequency estimation algorithm. In our simulations, we used the ML estimation algorithm by Rife and Boorstyn [61]. This powerful algorithm uses the FFT for estimation and it is only constrained by the sampling rate. This means that as long as $|f_D| < \frac{f_{\text{samp}}}{2}$, where f_{samp} is the sampling frequency, the detector B should works fine. In our simulation, we used $f_{\text{samp}} = 80$ kHz which is good enough to estimate the maximum theoretical Doppler shift encountered in our application that is around 20 kHz as presented in the first chapter. Simple frequency estimation algorithms should work fine as well, nevertheless, they

present some degradation of performance compared to the ML estimation algorithm so we did not address their limitation here.
To illustrate these limitations, we consider again the same conditions of the GMSK presented earlier and this time we show performance evolution with $f_D T_s$ at 11 dB compared to the coherent detector.

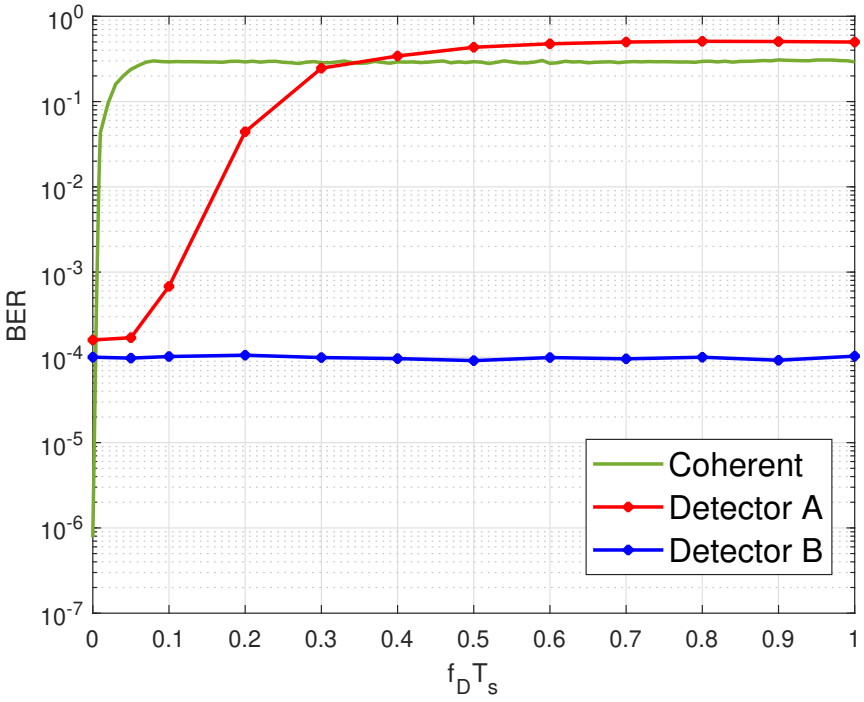

Figure 2.8 – BER evolution with $f_D T_s$ for detector A and B for the GMSK with $N_v = 5$ and $N_D = 8$ at 11 dB

Considering the GMSK format and compared to the coherent detector which is highly sensitive to Doppler effect, we can see that detector A can keep same performance up to $f_D T_s = 0.05$ and then starts to gradually decrease. On the other side, detector B keeps performing with no problem at much higher orders.

Complexity:

Table 2.2 and Table 2.3 summarizes the numerical values of S, Q_M and Q_D used in our simulations for the GMSK and the Quaternary 2RC respectively with $\rho = 8$ for detector B. $N_{\text{FFT}} = 32$ for detector A and $N_{\text{FFT}} = 32 \times \rho = 256$ for detector B so that the frequency resolution is the same. These numerical values further show the significant complexity reduction enabled by detector A but also highlights one of the limitations of the detector B which is the increased complexity of with different CPM schemes especially for the multilevel case.

Table 2.2 – Numerical values of S, Q and E for GMSK

Label	Detector A (N_{FFT}=32)	Detector B (N_{FFT}=256)
S	64	32
Q_M	643	2560
Q_D	10816	67840

Table 2.3 – Numerical values of S, Q and E for Quaternary 2RC

Label	Detector A (N_{FFT}=32)	Detector B (N_{FFT}=256)
S	1024	1024
Q_M	20512	163840
Q_D	338944	4284416

2.5 Conclusion

In this chapter, we proposed two CPM non coherent detectors robust to phase uncertainty, Doppler shift in a blind way. The first one (A) is adapted from a non-coherent CPM detection based on a linear decomposition of the CPM and the second one (B) is directly derived from the non-coherent detection criterion applied to the CPM waveform. The simulation results confirm the robustness of these detectors to small Doppler shifts, and to higher Doppler shifts for Detector B for which the only limitation is the performance of the blind Doppler shift estimator. The presented detectors are also perfectly robust to variable Doppler which makes them a solution to be considered in our targeted application given the rates encountered. If the Doppler shift is much higher, the detector B is the solution that offers the best overall Doppler robustness. Both detectors A and B are also robust against Doppler rate thanks to the sliding window. The general behaviour of detectors A and B is observed for the different considered CPM schemes. Depending on the available power onboard of the satellite, these detectors - although having good robustness to Doppler - may be considered to have a high complexity depending on the considered CPM scheme. In the next chapter, we want to come up with a lower complexity non coherent detector while keeping robustness against Doppler shift by elaborating on the differential detection.

Chapter 3

On the optimization of differential detection of CPM

Contents

As we have seen in the first chapter, differential detection offers some advantages which are solicited in our considered application. To this end, we were interested in this type of receivers and sought to improve the performance of the conventional differential reception technique of the CPM to get as close as possible to the optimal non coherent detection performance. Some works in the literature suggest that the usage of multiple symbols delay yields better performance in general, thus, we sought a method to optimize the delay value used.

We first present our detection strategy and then exploit the minimum Euclidean distance criterion to derive the delay optimization strategy. The performance of differential detection of some CPM schemes is analysed through bit error rate for different delay values for comparison. We then give the optimized delay values obtained for some CPM schemes. Finally, we assess the performance of our differential detector in presence of Doppler effect and compare it to the detectors presented in the previous chapter.

3.1 Description of the detection strategy

We begin by presenting the received signal model. We start by considering a Gaussian channel with phase offset. The Doppler shift is neglected at first stage and will be investigated later. Therefore, we consider uncoded CPM signal presented in Chapter 1 and given by Equation 1.12 transmitted over a Gaussian channel. The equivalent baseband received signal, denoted by $r(t)$, is given by Equation 1.27.

3.1.1 K-delay based differential receiver

At the receiver side, a differential signal denoted by $R_K(t)$ is obtained by multiplying the received signal $r(t)$ and the conjugate of its delayed version $r(t - KT_s)$. It can be decomposed as the sum of two signals:

$$R_K(t) = \frac{1}{2} r(t) r^*(t - KT_s) = S_K(t, \mathbf{a}) + N_K(t), \tag{3.1}$$

where the first term does not include any noise contribution:

$$S_K(t, \mathbf{a}) = \frac{1}{2} s(t, \mathbf{a}) s^*(t - KT_s, \mathbf{a}) = \frac{E_s}{T_s} \mathrm{e}^{j\Theta_K(t,\mathbf{a})} \tag{3.2}$$

with $\Theta_K(t, \mathbf{a}) = \theta(t, \mathbf{a}) - \theta(t - KT_s, \mathbf{a})$.
The second term, denoted by $N_K(t)$, consists of noise-only dependent components. It is decomposed as $N_K(t) = U_K(t) + W_K(t)$ with

$$\begin{aligned} U_K(t) &= \frac{1}{2} \left(s(t, \mathbf{a}) e^{j\psi} n^*(t - KT_s) + n(t) s^*(t - KT_s, \mathbf{a}) e^{-j\psi} \right), \\ W_K(t) &= \frac{1}{2} \left(n(t) n^*(t - KT_s) \right). \end{aligned} \tag{3.3}$$

The computation of its autocorrelation leads to the following expression:

$$E[N_K(t) N_K^*(t - \tau)] = (N_0^2 + A^2 N_0) \delta(\tau) \tag{3.4}$$

with $A = |s(t, \mathbf{a})| = \sqrt{\frac{2E_s}{T_s}}$ and $\delta(t)$ is the delta function. Details about this calculation can be found in Appendix C.1. Hence, we conclude that the random process $N_K(t)$ is wide-sense stationary with zero mean and constant power spectral density (PSD) equal to $(N_0^2 + A^2 N_0)$. From now on, it will be assumed to follow a Gaussian distribution as in [13].
We validated this assumption through computer simulations. We generated 1000 realizations of the complex differential noise $N_K(t)$ for different levels of SNR. Then, we can visualize the pdf of the real part and the imaginary part of the noise through histograms where the pdf have a variance equals to half that of $N_K(t)$. It is also easy to see that $E[N_K^2(t)] = 0$ which proves the

independence of the real and imaginary parts of $N_K(t)$.

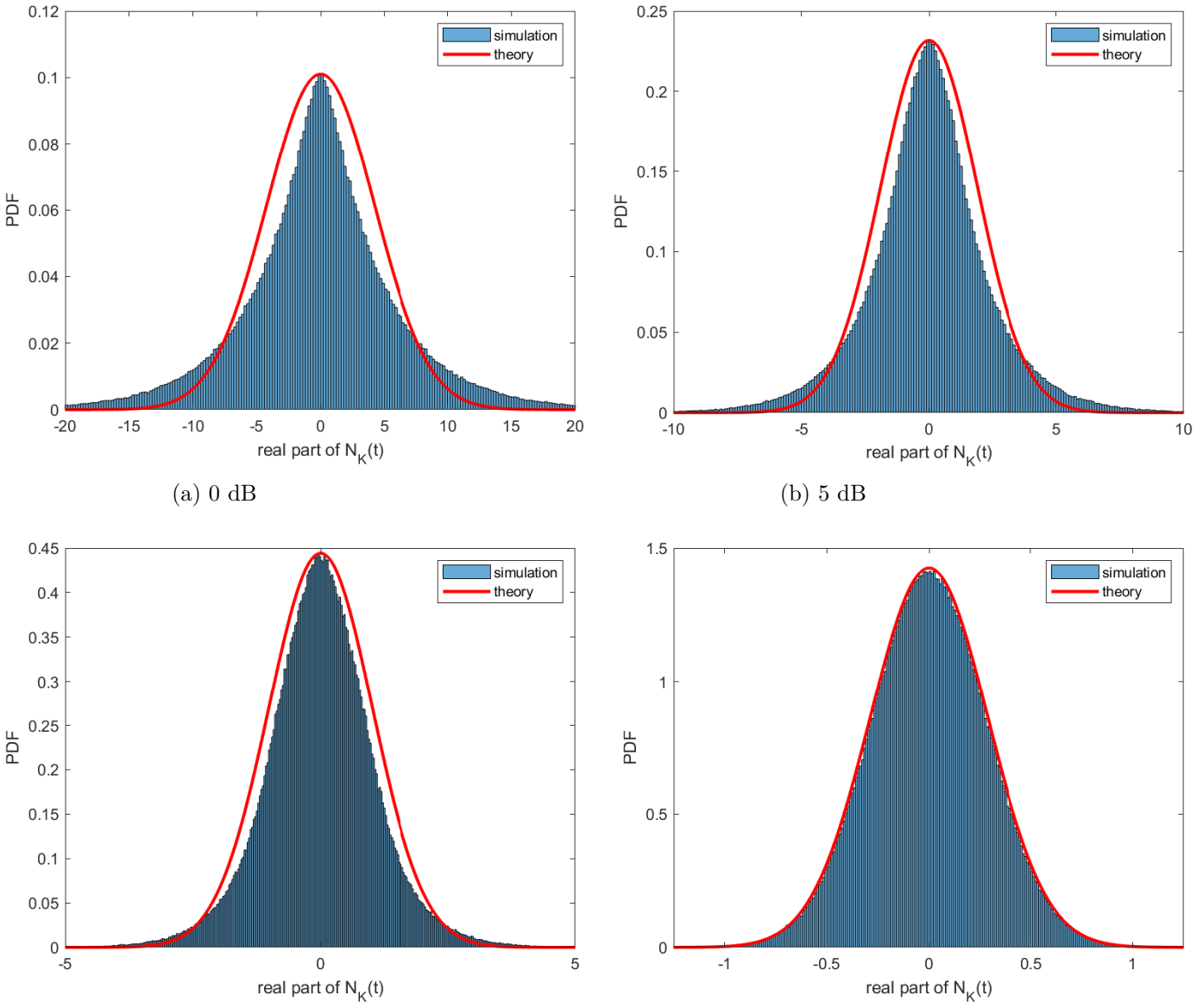

(a) 0 dB

(b) 5 dB

(c) 10 dB

(d) 20 dB

Figure 3.1 – Histograms of the pdf of the real part of the noise $N_K(t)$ over 1000 iterations for different levels of SNR compared to the pdf of normal distribution $N\left(0, \frac{(N_0^2+A^2N_0)}{2}\right)$

Figure 3.1 shows the obtained histograms for the real part (since the same result is obtained for the imaginary part) compared to an actual pdf of the normal distribution having zero mean and variance $\frac{(N_0^2+A^2N_0)}{2}$ in the considered simulation. We can see that the assumption is all the more accurate as the SNR is higher.

3.1.2 Phase trellis description

Let $t = \tau + nT_s$, with $0 \leq \tau < T_s$ and $n \in \{0, 1, \ldots, N-1\}$. Taking into account the properties of the frequency pulse given in (1.15), the phase introduced in (3.2) can be decomposed as the sum of a time-independent term and a time-dependent term:

$$\Theta_K(\tau + nT_s, \mathbf{a}) = \phi_n + 2\pi h a_n q(\tau) + \varphi_n(\tau), \tag{3.5}$$

with $\phi_n = \pi h \sum_{i=0}^{K-1} a_{n-L-i}$ and

$$\varphi_n(\tau) = \quad 2\pi h \sum_{i=1}^{L-1} (a_{n-i} - a_{n-K-i}) q(\tau + iT_s) - a_{n-K} q(\tau). \tag{3.6}$$

$\varphi_n(\tau)$ represents a time-dependent contribution which corresponds to the last L memory symbols of both the signal and its delayed version. The term ϕ_n represents the time-independent part. $\varphi_n(\tau)$ and ϕ_n are completely determined by the set of symbols $(a_{n-i})_{1 \leq i \leq L+K-1}$. As a consequence, ϕ_n doesn't need to be stored, contrary to the original CPM trellis description which comprises the cumulative phase as a defining state parameter. We can thus define the state $\Sigma_n = [a_{n-L-K+1}, ..., a_{n-1}]$ for the n-th section of the trellis representation of $\Theta_K(t, \mathbf{a})$. Note that there are M^{K+L-1} different possible states.

3.1.3 Maximum likelihood (ML)-based detection

The ML criterion is applied to detect the information symbols from $R_K(t)$. Given the constant amplitude property of CPM, it consists in maximizing the correlation between $R_K(t)$ and all possible realizations of $S_K(t, \mathbf{a})$. The inner product between $R_K(t)$ and a specific realization $S_K(t, \tilde{\mathbf{a}})$, denoted by $\Gamma_N(\tilde{\mathbf{a}})$, is defined as

$$\Gamma_N(\tilde{\mathbf{a}}) = \Re \left[\int_0^{NT_s} R_K(t) S_K^{\star}(t, \tilde{\mathbf{a}}) dt \right], \tag{3.7}$$

with $\Re(.)$ designating the real part operator and which can be recursively computed:

$$\Gamma_n(\tilde{\mathbf{a}}) = \Gamma_{n-1}(\tilde{\mathbf{a}}) + \Lambda_n(\tilde{\mathbf{a}}) \tag{3.8}$$

with

$$\Lambda_n(\tilde{\mathbf{a}}) = \Re\left[\int_{(n-1)T_s}^{nT_s} R_K(t) S_K^{\star}(t, \tilde{\mathbf{a}}) dt\right]. \tag{3.9}$$

The Viterbi algorithm is applied on the trellis. At the $n-$th section, it computes for each state the maximum cumulative metric (3.8) among all the paths arriving at this state. The total number of states is given by $S = M^{K+L-1}$. Figure 3.2 shows the architecture of the differential receiver.

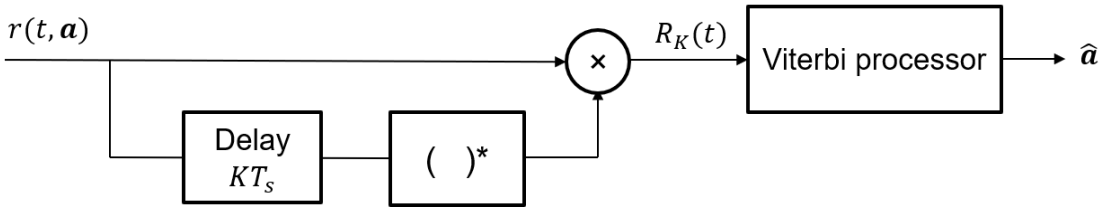

Figure 3.2 – Differential detector architecture

3.1.4 Influence of the delay on the detection performance

In this section, we propose to investigate the influence of the delay on the detection performance in an AWGN channel. First, we consider the CPM format 5RC with $h = 0.75$. The delay K takes on values in {1,2,3,4}. The Bit Error Rate (BER) is plotted as a function of E_s/N_0 in Figure 3.3. We observe that by increasing the delay value K, better performance can be achieved and for the receiver with $K = 4$ a gain of 2 dB is obtained compared to the receiver with $K = 1$ at BER 10^{-3}. Next, we consider the CPM format 3REC with $h = 0.75$ where the delay K takes on values again in {1,2,3,4} and the results are given in Figure 3.4. We observe that $K = 3$ is the delay that yields the best BER. A gain of 3 dB is obtained compared to the receiver with $K = 1$ and almost 1 dB compared to the receiver with $K = 2$ while the receiver with $K = 4$ exhibits a slight degradation of performance. These results and other results from several CPM format that we have tested showed that increasing the delay in the differential receiver can yield better performance but only up to a certain level beyond which the performance keeps the same or even worse, there might be some degradation. To this end, it is necessary to optimize the delay value which we will detail in the next section.

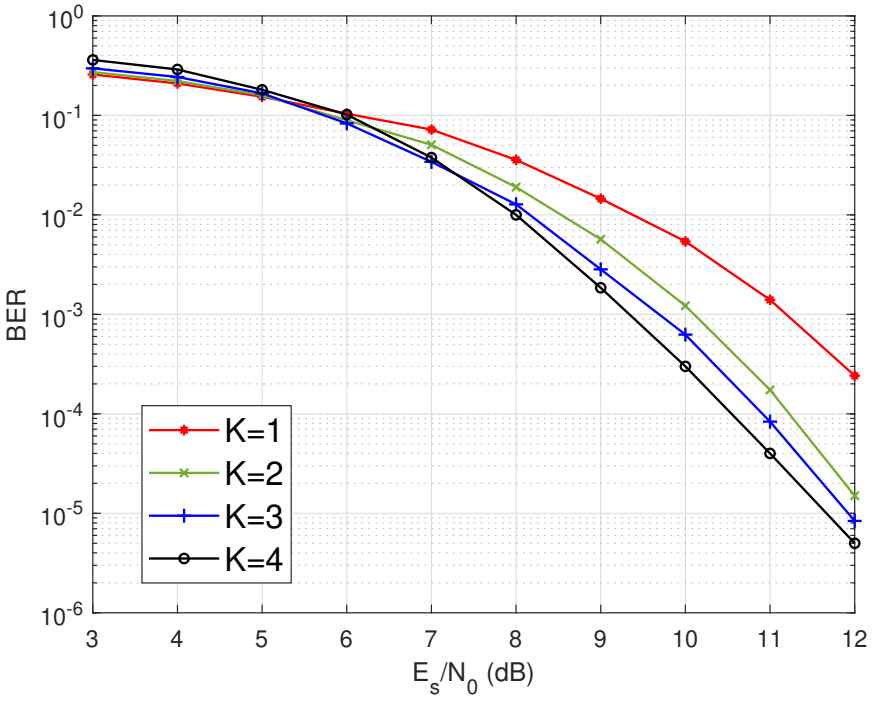

Figure 3.3 – BER of differential detection for the CPM scheme 5RC with $h = 0.75$ for different values of delay K

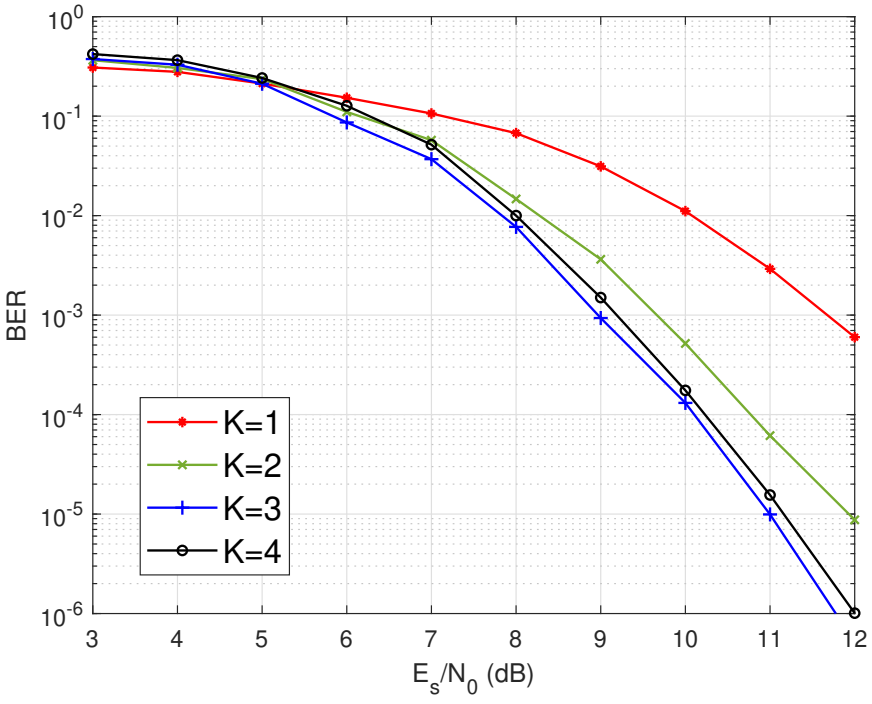

Figure 3.4 – BER of differential detection for the CPM scheme 3REC with $h = 0.75$ for different values of delay K

3.2 Delay optimization

In this section, we aim at tuning K to improve the detection error probability. Let us consider the following error event when $s(t,\mathbf{a})$ is transmitted, $s(t,\tilde{\mathbf{a}})$ is detected and $\mathbf{a} \neq \tilde{\mathbf{a}}$. Given the ML-based detection criterion and the independence between R_K and N_K, it means that:

$$\int_0^{NT_s} |R_K(t) - S_K(t,\tilde{\mathbf{a}})|^2 dt \leq \int_0^{NT_s} |R_K(t) - S_K(t,\mathbf{a})|^2 dt \tag{3.10}$$

which can be reformulated as:

$$Z_K \geq \frac{1}{2}\Delta_K^2(\mathbf{a},\tilde{\mathbf{a}}), \tag{3.11}$$

where

$$Z_K = \int_0^{NT_s} \Re\big(\left(S_K(t,\mathbf{a}) - S_K(t,\tilde{\mathbf{a}})\right) N_K^*(t)\big) dt, \tag{3.12}$$

and

$$\Delta_K(\mathbf{a},\tilde{\mathbf{a}}) = \sqrt{\int_0^{NT_s} \left|S_K(t,\mathbf{a}) - S_K(t,\tilde{\mathbf{a}})\right|^2 dt}, \tag{3.13}$$

$\Delta_K(\mathbf{a},\tilde{\mathbf{a}})$ is the Euclidean distance between the two differential signals $S_K(t,\mathbf{a})$ and $S_K(t,\tilde{\mathbf{a}})$ corresponding to the symbol sequences $\mathbf{a}$ and $\tilde{\mathbf{a}}$. Details about this calculation can also be found in Appendix C.2. Z_K has zero mean. Assuming that Z_K is Gaussian, the probability of an error event is given by

$$P_e(\mathbf{a};\tilde{\mathbf{a}}) = Q\left(\sqrt{\frac{\varepsilon_b}{2(N_0^2 + A^2 N_0)} d_K^2(\mathbf{a},\tilde{\mathbf{a}})}\right) \tag{3.14}$$

where Q is the $Q-$function and where $d_K(\mathbf{a},\tilde{\mathbf{a}}) = \frac{\Delta_K(\mathbf{a},\tilde{\mathbf{a}})}{\sqrt{2\varepsilon_b}}$ is the normalized Euclidean distance, ε_b denoting the average energy per information bit in the differential symbol sequence. Proceeding as in [14, Chapter 2, Paragraph 2.1.2], a union bound on the probability of error is obtained at reasonably high SNR. The error probability is thus approximated by

$$P_e \propto Q\left(\sqrt{\frac{\varepsilon_b}{2(N_0^2 + A^2 N_0)} d_{\min}^2(K)}\right) \tag{3.15}$$

where:

$$d_{\min}^2(K) = \min_{\substack{\mathbf{a},\tilde{\mathbf{a}} \\ a_0 \neq \tilde{a}_0}} \left(d_K^2(\mathbf{a},\tilde{\mathbf{a}})\right) \tag{3.16}$$

By applying the same reasoning as in [14], we obtain:

$$d_K^2(\mathbf{a},\tilde{\mathbf{a}}) = \frac{\log_2(M)}{T_s} \int_0^{NT_s} [1 - \cos\left(\Theta_K(t,\mathbf{e})\right)] dt \tag{3.17}$$

where $\mathbf{e} = \mathbf{a} - \tilde{\mathbf{a}}$ is the difference symbol sequence as defined in the first chapter. Further details on this computation of this formula is in Appendix C.3.
Finding the minimum Euclidean distance is done by searching over all possible pairs of sequences $\mathbf{a}$ and $\tilde{\mathbf{a}}$. In practice, these pairs are those whose respective paths on a phase tree diverge at time 0 and merge again as soon as possible. Proceeding as in [14], the phase difference tree is a good method to determine the difference symbol sequences to be considered and the corresponding pairs of symbol sequences.

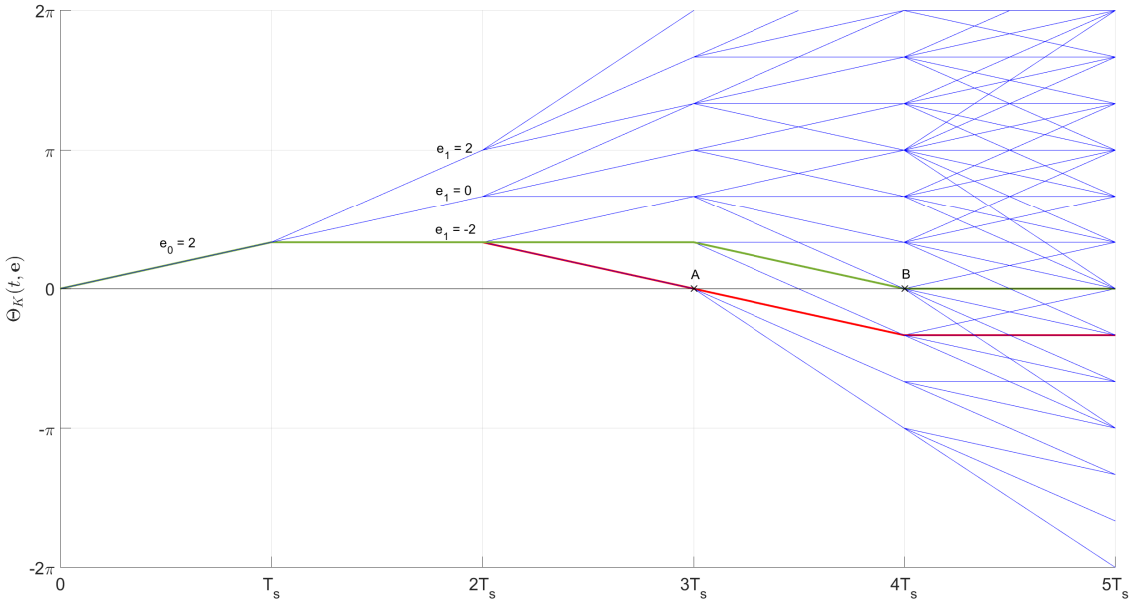

Figure 3.5 – Phase difference tree of the differential phase $\Theta_K(t, \mathbf{e})$ for the scheme binary 3REC with $h = 0.5$ and $K = 4$

Finding the pairs of sequences $\mathbf{a}$ and $\tilde{\mathbf{a}}$ to consider in the computation of minimum distance is equivalent to finding their difference sequence $\mathbf{e} = \mathbf{a} - \tilde{\mathbf{a}}$. The difference sequences to consider are those presenting an error in the beginning ($e_0 \neq 0$) and then merging with 0 phase axis. The phase difference tree is plotted in Figure (3.5) considering the binary 3REC scheme with $h = 0.5$ and the delay value $K = 4$ which is the optimized delay value. Note that the red path crosses the 0 phase axis first at point A. However, the difference sequence corresponding to the red path is not to be considered since this path then diverges from the 0 phase axis. Instead, the first merger occurs at point B so the difference sequence corresponding to the green path is the first sequence to consider in the computation of $d_{\min}$. For each value of the delay, we get a different phase tree and thus, we select the pairs of sequences to consider correspondingly. Hence, a corresponding value of the minimum Euclidean distance $d_{\min}$ is obtained for each value

of the delay considered in the optimization process. Since we are looking for minimizing the error probability, the best choice of the delay is the value that yields the highest $d_{\min}$.

3.3 Simulation results

In this section, we study different CPM formats. We focus on Satellite IoT which involves short frame communications over a non-frequency selective channel mainly disturbed by Doppler effects. In the simulation setup, we thus consider only an AWGN channel in the first place, to which we add Doppler shift in second place with the frame length being $N = 120$ which is a choice that does not affect the final conclusions.

3.3.1 Optimization of the delay from the minimum Euclidean distance criterion

Given a CPM format ($g(t)$, L, h), the optimization of K from the Euclidean distance computation in Equation (3.17) is run by Monte-Carlo simulations by considering several possible pairs of sequences yielding different possible realizations of $\mathbf{e}$. The optimized value of K is provided in Tables 3.1, 3.2, 3.3 for raised cosine (RC), rectangular (REC) and Gaussian (GFSK) frequency pulses respectively. We consider several modulation indices h and several frequency pulse lengths L. The consistency of the optimized delay has also been checked by BER simulations for all CPM formats. Note that when several values of K provide the same best error rate, then the displayed value is simply the lowest one to reduce the complexity of the decoder.

Table 3.1 – Optimized values of K for RC CPM

Freq. pulse length L	Modulation index $h = 1/3$	$h = 1/2$	$h = 3/4$
1	$K = 2$	$K = 2$	$K = 3$
3	$K = 3$	$K = 3$	$K = 3$
5	$K = 4$	$K = 4$	$K = 4$

Table 3.2 – Optimized values of K for REC CPM

Freq. pulse length L	Modulation index $h = 1/3$	$h = 1/2$	$h = 3/4$
1	$K = 2$	$K = 2$	$K = 4$
3	$K = 4$	$K = 4$	$K = 3$
5	$K = 5$	$K = 5$	$K = 5$

Table 3.3 – Optimized values of K for GFSK ($BT = 0.3$)

Freq. pulse length L	Modulation index $h = 1/3$	$h = 1/2$	$h = 3/4$
3	$K = 3$	$K = 3$	$K = 4$
5	$K = 3$	$K = 3$	$K = 4$

3.3.2 Comparison with some state-of-the-art receivers

In Figure 3.6, we show a comparison between the optimized differential receiver (K_{opt}), the conventional differential receiver ($K = 1$), and also the coherent receiver. This comparison is performed for 2 different CPM families: GFSK with $h = 0.5$ and $BT = 0.3$ (GMSK), and 5RC with $h = 0.5$. For GMSK, there is almost 4 dB between the coherent BER and the conventional differential detection ($K = 1$). Using the optimized $K = 3$ reduces this gap by almost 2 dB. For the 5RC CPM, using the optimized $K = 4$ delay reduces the gap to coherent BER from around 6 dB down to 2 dB. Note that the curves for the coherent and the optimized differential receivers are quasi-parallel which means that the diversity gain is almost the same and the difference between the two is mainly in the noise variance which is higher for the differential receiver.

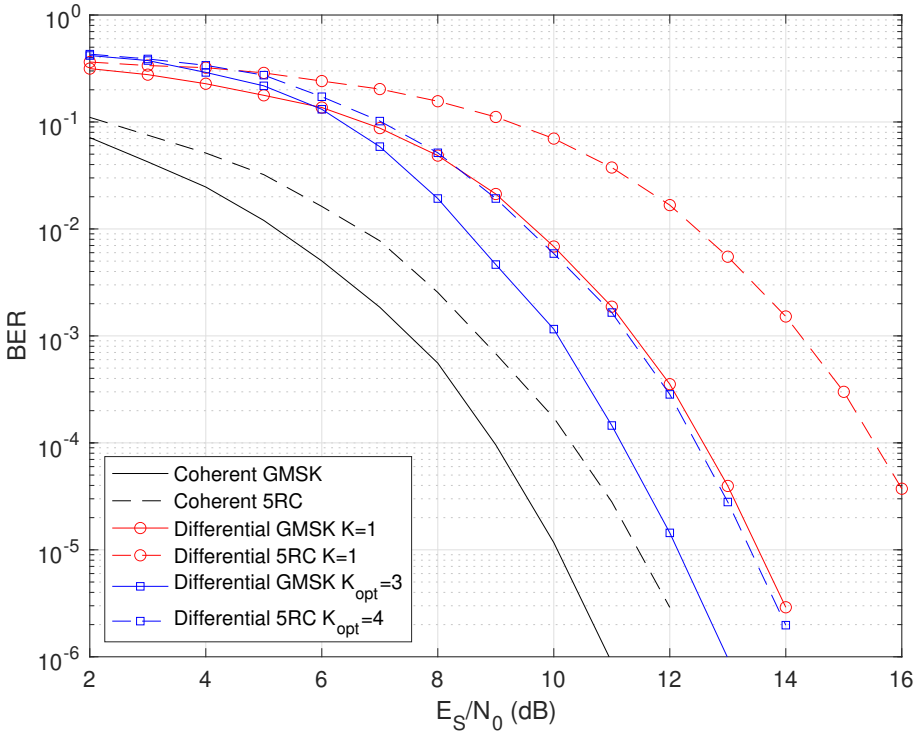

Figure 3.6 – BER comparison between coherent and differential detection for two CPM schemes: GMSK with $BT = 0.3$, and 5RC with $h = 0.5$

3.3.3 Performance in presence of Doppler

The differential detector could be especially interesting in applications where the Doppler shift affects the communication. Suppose in our model that we have a constant frequency shift due to Doppler that is denoted by f_D, thus the received signal will be given by Equation (2.1) This will result in a constant phase term in the differential signal $R_K(t)$ which is given by $\Psi = 2\pi K f_D T_s$. Note that in this term, the product $f_D T_s$ is what actually determines the rotation impact (since eventually $K = K_{opt}$). For this reason, we chose to present the results in this section as a function of $f_D T_s$.

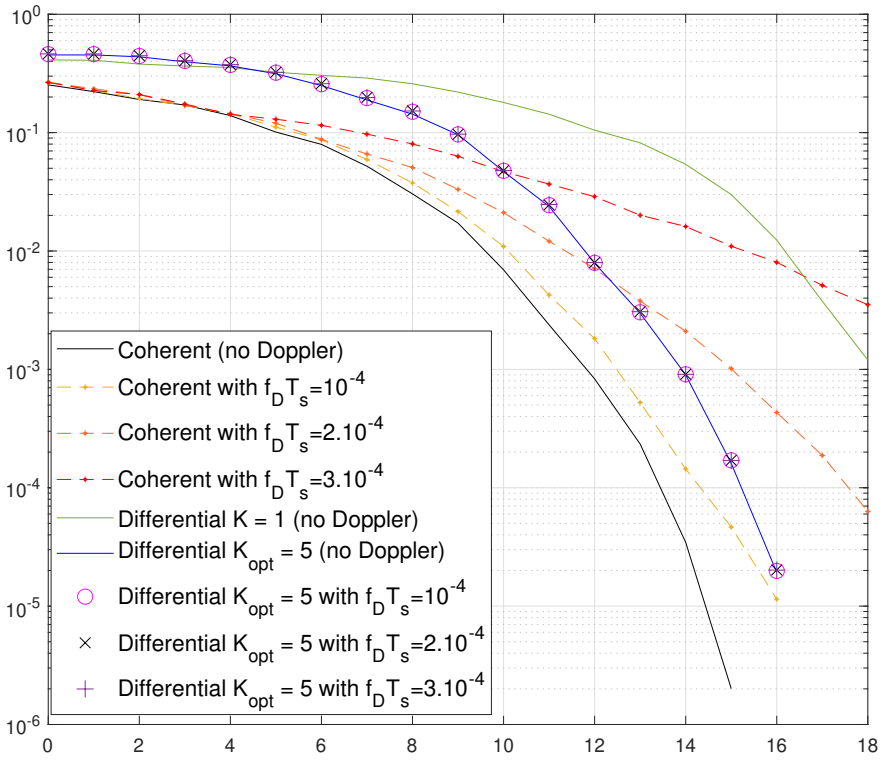

Figure 3.7 – BER comparison between coherent and differential detection for 5REC with $h = 0.5$ in the presence of a Doppler shift

It is known that coherent detection is highly sensitive to frequency shift and what we want to highlight here, is the robustness of our differential detector to Doppler shift. To that end, a performance comparison between the differential detector and the coherent one in terms of BER is illustrated in Figure 3.7 for the rectangular pulse with $h = 0.5$ and $L = 5$ in presence of a

small Doppler shift. We see a huge performance degradation for the coherent detector whereas the differential detector is not affected for the considered Doppler shift values.
To further investigate this robustness, in Figure (3.8), we consider the GMSK format and we show the performance of the differential detector at 11 dB in presence of a Doppler shift in comparison with the reference differential detection ($K = 1$) and the coherent one. We can see that the receiver is robust to the Doppler shift up to an order of 0.1 of $f_D T_s$ and then the performance starts slowly to decrease whereas the performance of the non optimized detector starts to decrease earlier and the degradation occurs for very small values of $f_D T_s$ for the coherent detector. The same behavior is observed in the case of other modulation format as $f_D T_s$ increase.

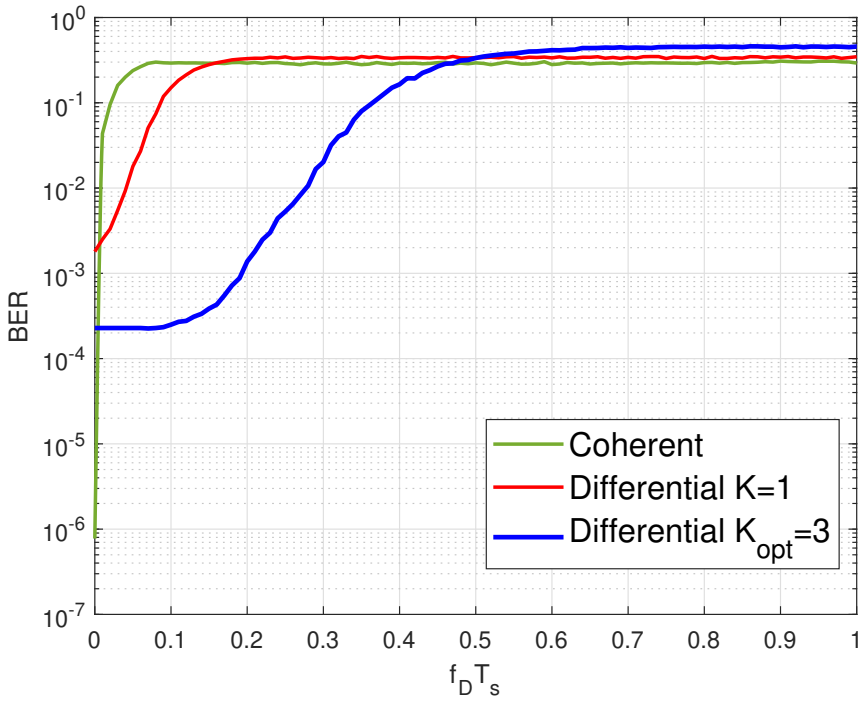

Figure 3.8 – Comparison of BER evolution with $f_D T_s$ for GMSK for the coherent detector, the differential detector for $K = 1$ and $K_{opt} = 3$ at 11 dB of SNR

One solution would be the phase offset estimation and compensation thanks to the use of pilot sequence known to the receiver (preamble). The differential detection is robust to phase offset whose values are lower than a threshold. A coarse estimation of the phase offset is thus sufficient. A limited number of pilot symbols is required and low-complexity data-aided estimation algorithms can be applied

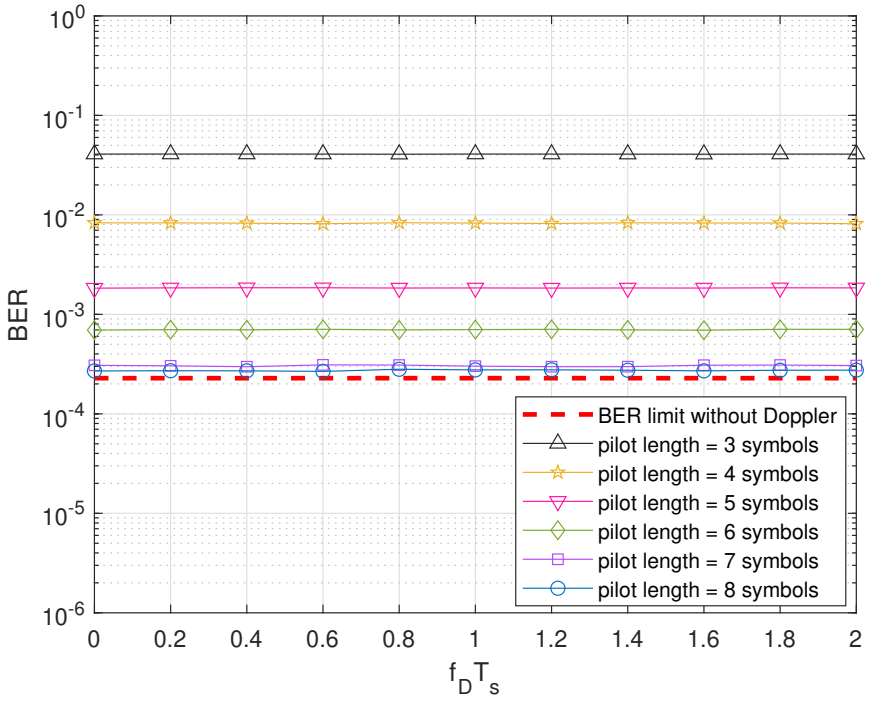

Figure 3.9 – Comparison of BER evolution with $f_D T_s$ for GMSK for the differential detector with $K_{opt} = 3$ at 11 dB of SNR using pilot sequence for frequency estimation

In Figure (3.9), we consider the same GMSK format as in Figure 2.7. We apply the simple Kay algorithm [62] [63] to estimate the Doppler shift from pilot symbols. We make the preamble size vary from 3 to 8 symbols and we observe that a size of 7 symbols is nearly enough to avoid the performance degradation due to the Doppler shift. This size corresponds to almost 6% of the considered frame.

In presence of a time-varying Doppler shift (Doppler rate different from zero), the differentiation operation transforms the variable Doppler shift into a variable phase offset given by :

$$\Psi_D(t) = 2\pi K f_D T_s - \pi f_R (K T_s)^2 + 2\pi K f_R T_s t \tag{3.18}$$

In practice, the Doppler rate should have a limited impact on the performance. First, K is limited and lower than 6. Then the data rate is in the range of some kbps, yielding rather low symbol period values. Taking into account the Doppler profile of LEO satellites as well as the small size of IoT packets on top of the previously listed properties, the phase offset due to f_R should not vary much within the frame. However as previously mentioned, it could be necessary to compensate the one due to f_D depending on the SatIoT system parameters.

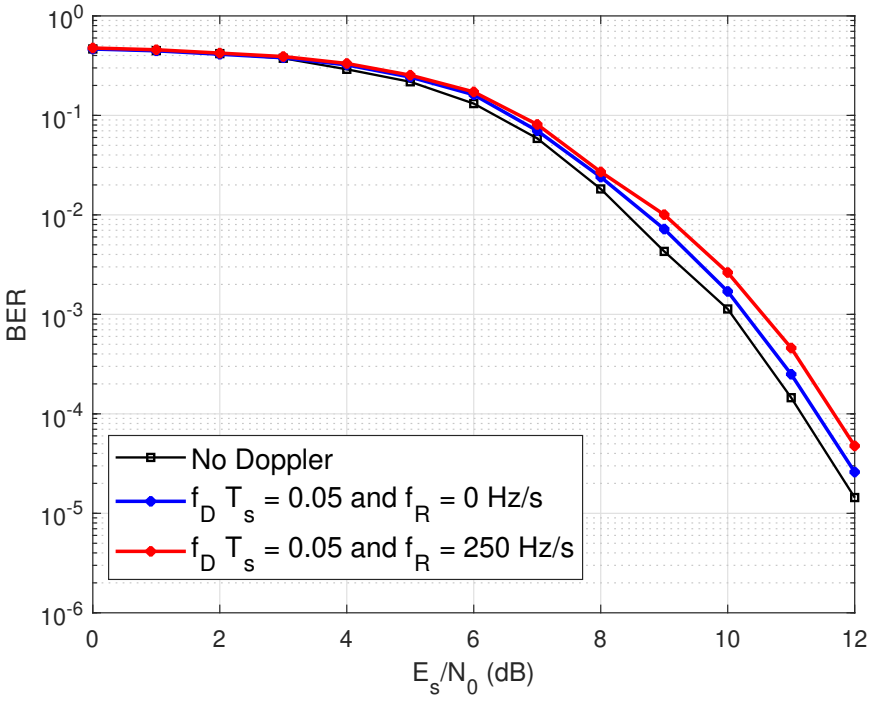

Figure 3.10 – BER comparison of GMSK with the differential detector with $K_{opt} = 3$ in presence of no Doppler, Doppler shift only and Doppler shift and rate

This observation is supported by the simulations reported in Figure 3.10. We consider the same GMSK format as in Figure 3.8 with $f_D T_s = 0.05$ and a Doppler rate of 250Hz/s which is the maximum theoretical rate encountered in our application. A very slight decrease in performance is observed.
Finally, based on these results, we can say that the differential detector is a good choice for the Satellite IoT application. It can resist the Doppler orders encountered at various altitudes in the LEO range given small symbol duration. However, when operating in the lowest altitudes, much higher Doppler orders are expected and thus, usage of few pilot symbols with low-complexity DA estimation is a simple solution to keep the same level of performance of the differential detector.

3.4 Comparison with detectors A and B

We propose in this section to compare the performance and complexity of optimized delay differential detector with that of detectors A and B. We consider the GMSK scheme again. We also consider two normalized Doppler shifts $f_D T_s = 0.05$ and $f_D T_s = 0.1$ for which the differential detector and detector B keeps performing at the same level whereas the performance of detector A starts decreasing for the higher value (as explained in the previous chapter).

Different parameters for both detectors A and B (N_v, N_D, N_{FFT} and ρ) are fixed as in Chapter 2 to produce the best trade off between performance and complexity. In Figure 3.11, we can see

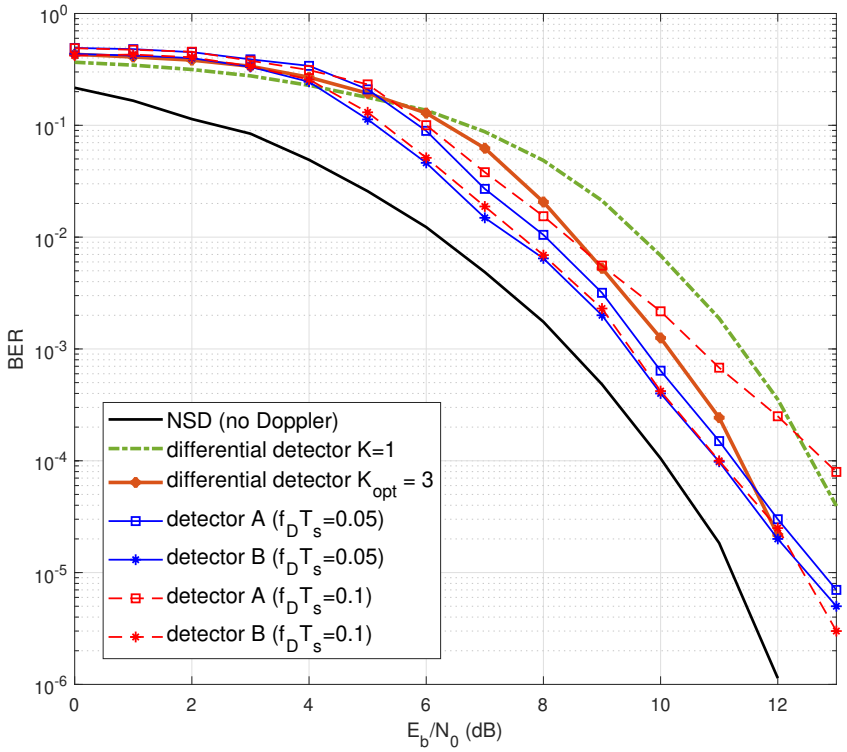

Figure 3.11 – Comparison of detectors A ($\rho = 1$, $N_{\mathrm{FFT}} = 32$) and B ($\rho = 8$, $N_{\mathrm{FFT}} = 256$) with optimized-delay differential detector for GMSK - $N_v = 5$, $N_D = 8$

that the performance of optimized delay differential detector rivals that detectors A and B with a loss of about 1 dB in the low / mid SNR regime. We observe that $f_D T_s = 10^{-1}$ is the threshold beyond which the BER curve of the differential detection with optimized delay crosses the BER curve of Detector B at a BER of 2.10^{-5}.

The error rate comparison between Detector B and differential detector for a 3REC CPM with $h = 0.75$ is illustrated in Figure 3.12a using the same Doppler shift estimation as for the previous GMSK case (same frequency resolution size). We observe that the gap to NSD is however higher (about 3 dB for a BER of 10^{-3}). We also observe that the performance of differential detection with optimized delay performs better below a BER of 10^{-2}. It is of course possible to reduce the gap between Detector B and NSD by improving the Doppler shift estimation, yielding a higher complexity. In the following, a complexity estimation is proposed to unveil the best performance-complexity trade-offs.

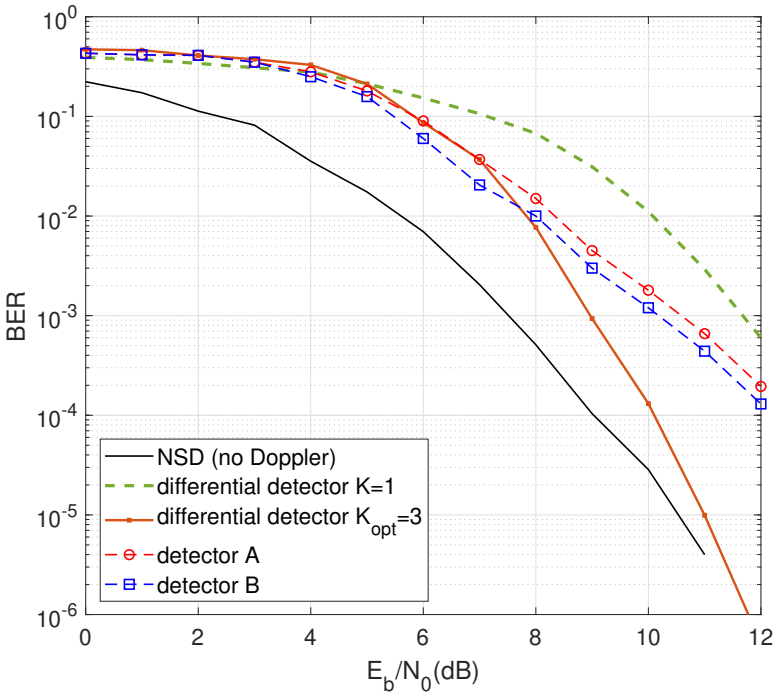

(a) $f_D T_s = 0.05$

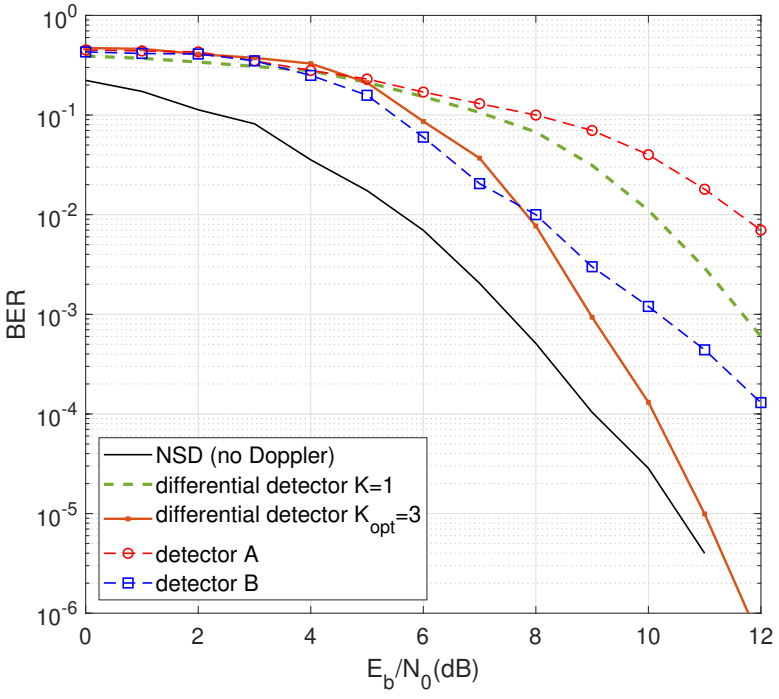

(b) $f_D T_s = 0.1$

Figure 3.12 – Comparison of detector B with optimized-delay differential detector in presence of Doppler for CPM 3REC with $h = 0.75$ - $N_v = 5$, $N_D = 8$, $\rho = 8$ and $N_{\text{FFT}} = 256$

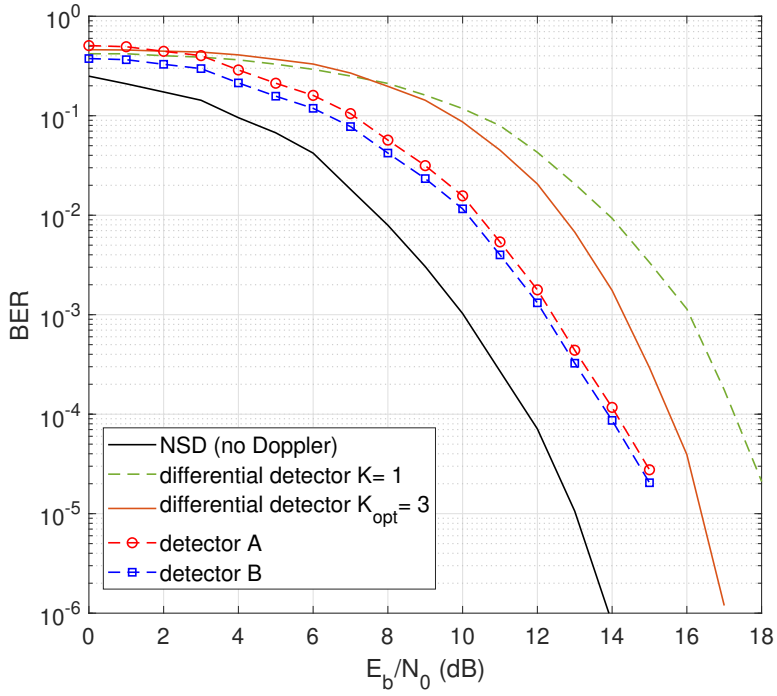

(a) $f_D T_s = 0.05$

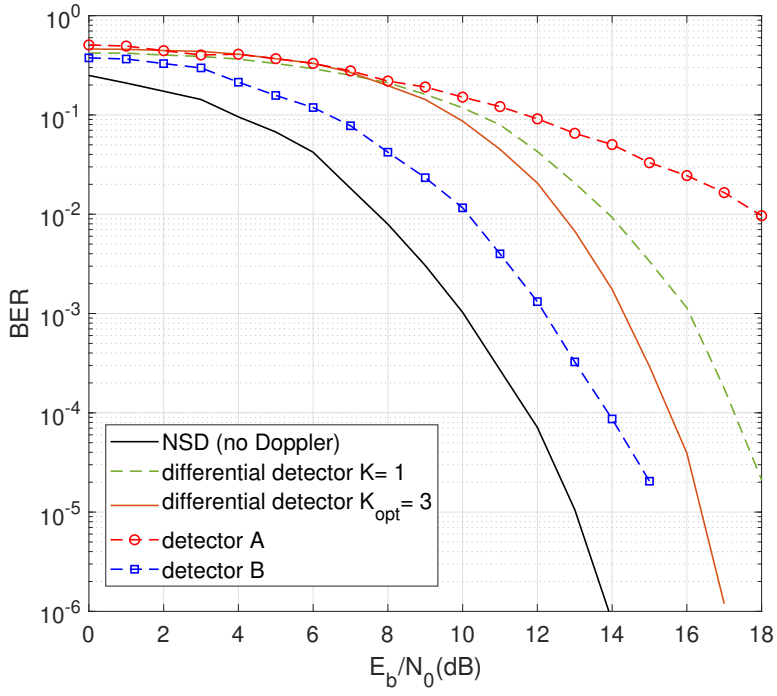

(b) $f_D T_s = 0.1$

Figure 3.13 – Comparison of detector A with optimized-delay differential detector in presence of Doppler ($f_D T_s = 0.05$) for Quaternary 2RC with $h = 0.25$ - $N_v = 5$, $N_D = 8$, $\rho = 1$ and $N_{\text{FFT}} = 32$

Table 3.4 – Numerical values of S, Q and E for GMSK

Label	Detector A (N_{FFT}=32)	Detector B (N_{FFT}=256)	Differential detector ($K_{opt} = 3$)
S	64	32	16
Q_M	643	2560	256
Q_D	10816	67840	NA

As an example of multilevel CPM, we consider the Quaternary 2RC with $h = 0.25$ where in Figure 3.13a, we compare the BER performance of detector A presented in Section 2.4.1 with the performance of differential detector. For this format, the optimal delay value is $K_{opt} = 3$. In the simulation, we considered $N_v = 5$, $N_D = 8$, $\rho = 1$ and $N_{\mathrm{FFT}} = 32$ for detector A.
In Figure 3.13a, we notice that the gap between the performance of detector A and the NSD is about 2.5 dB at BER of 10^{-4} but this gap is much higher (about 3.5 dB) compared to differential detector. However, performance of differential detector approaches even more that of NSD at much higher SNR and the gap is reduced to 2.5 db at approximately a BER of 10^{-6}.
In summary, we can see from Figures 3.11, 3.12 and 3.13, that performance difference between the differential detector and detectors A and B slightly depends on the considered scheme.

In terms of complexity, we already assessed the complexity of detectors A and B in terms of the number of trellis states (S), the number of multiplications for metric calculation (Q_M) per trellis section and the number of multiplications for Doppler Shift estimation per trellis section (Q_D).
The two first figures S and Q_M for the differential detector are given by :

— $S = M^{K_{opt}+L-1}$

— $Q_M = \rho SM$

Contrary to detectors A and B, there is no Doppler estimation each section for the differential detector. However, if very high Doppler is present, frequency estimation using a preamble can be considered to maintain performance. This operation is not repeated each section of the trellis, it is done once before start decoding and it accounts for $\frac{N_{\mathrm{FFT}}}{2}\log_2(N_{\mathrm{FFT}})$ multiplications to be added to the total number.
In Table 3.4, we present the numerical values of S, Q_M and Q_D for comparison between all three detectors for the GMSK. We can see that the differential detector presents low complexity compared to detectors A and B. If frequency estimation using a preamble is considered, a total of 1024 multiplications has to be added to the total number of multiplication but despite that, the differential detector still exhibits less overall complexity compared to detectors A and B.

Considering both complexity and error rates, we can state that differential detector with optimized delay is to be chosen in the high SNR regime or if low complexity is mandatory. If the constraint on complexity is a bit relaxed and lower SNR is considered, then detector A can be chosen if the Doppler shift is small. For larger Doppler shifts and low SNR, improved performance can be obtained close to the non-Doppler case with Detector B while increasing the complexity (both on the metric part and on the Doppler estimation part). The thresholds involved in this comparison do depend on the considered CPM parameters.

3.5 Conclusion

In this chapter, we have seen that the increase of the delay used in the conventional non-coherent differential detection of CPM has an impact on the error rate. We have therefore proposed to optimize this delay based on the minimum Euclidean distance between two differential signals.
This optimized delay ranges from 2 to 5 symbol periods depending on the considered CPM format. Simulations have confirmed the choice of the optimized delay value which offers a gain from 2 to 4 dB on the error rate performance compared to a single symbol duration delay. In presence of Doppler shift, the differential detector has shown a robustness up to a certain level. This robustness can be slightly maintained for higher levels using simple frequency estimation algorithm in conjunction with a small preamble. In the context of IoT communications with LEO satellites, the Doppler rate profile as well as the small packet size have accounted for a very slight performance degradation.
The differential detector is also compared to detectors A and B from the previous chapter. In the case of having a moderate Doppler shift, when an optimized delay is used and for a the considered Doppler orders, differential detection performs better in the high SNR / low error rate regime, while keeping a low complexity. As far as a lower SNR regime is concerned, provided that complexity is not an issue, Detector A for low Doppler shifts and Detector B otherwise offer better performances. After presenting the differential detector and a comparison with detectors A and B from Chapter 2, we propose in the next chapter to assess the performance of all these detectors in presence of interference from other communicating object.

Chapter 4

Performance in presence of interference in a LEO satellites link

Contents

This chapter is dedicated to evaluating the performance of the previously presented detectors (A, B and optimized-delay differential) under scenarios involving collision between received packets in satellite link conditions. First, we specify the reception scenarios.Then we investigate the performance of frequency estimator used in detectors A and B in presence of interference. Lastly, we present the performance of the three receivers in three possible scenarios.

4.1 Reception scenario

The coverage area of the satellite A_{sat} corresponds to the blue zone in Figure 4.1. Using the parameters presented in this figure, the surface of this area is given by :

$$A_{\text{sat}} = 2\pi R_e^2(1 - \cos(\beta)) \tag{4.1}$$

where the angle β can be expressed in terms of the minimum elevation angle γ by Equation (1.1). R_e is the radius of the Earth and H is the satellite altitude.

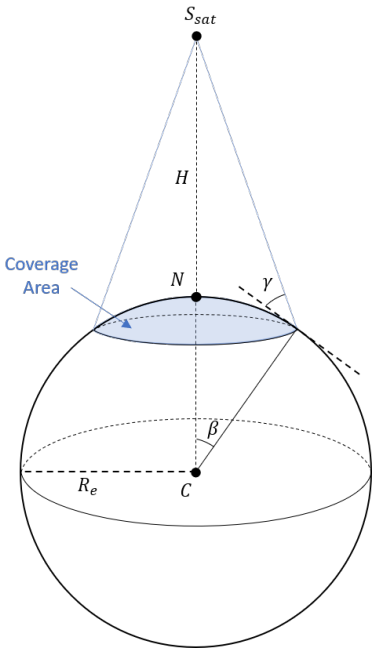

Figure 4.1 – Coverage area of the satellite

As an example, the coverage area for a satellite in the Iridium system constellation is almost 15.3 million km^2 which corresponds to an area with a footprint radius of 2209 km [22]. To put it into perspective, this area is enough to cover the whole European continent, and considering that the communicating objects are randomly accessing the channel, collisions between packets are likely to occur.
In the reception scenario that we consider, the object of interest is at the sub-satellite point (see Figure 1.1). This is the favorable case for the object of interest in terms of received signal power. Moreover, the interfering objects are assumed to be randomly distributed in the coverage area. We consider the coverage area example of the Iridium system. This means that the furthest interfering object is situated at almost 2200 km and this impacts two main parameters in the interfering signal, the received power and the Doppler shift.

The received power difference between the signal of interest and its interference can be studied by focusing on the free space loss solely as the other terms in Equation (1.7) do not depend on the object position. We fix the object of interest and make the position of the interfering source randomly vary within a sphere centered around the object of interest.

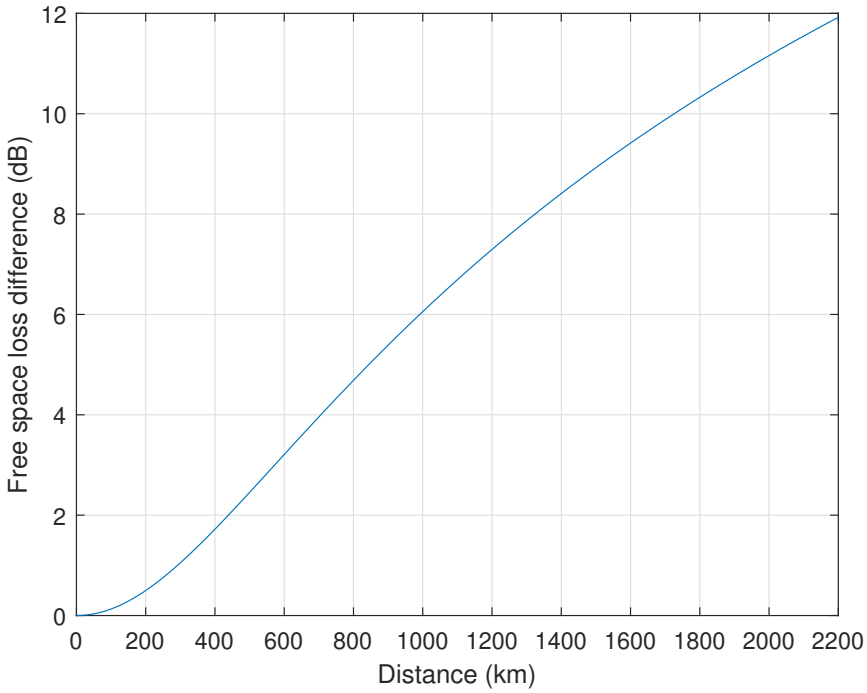

Figure 4.2 – Free space loss difference between the object of interest and an interfering object as function of the distance between both objects

In Figure (4.2), we present the expected free space loss difference between the object of interest and an interfering object within the radius of the coverage area. We can see that for objects separated by less than 200 km, their free space loss L_{space} difference is relatively low (less than 1 dB) and therefore, their respective signal powers are almost identical when received by the satellite.
A difference of Doppler shift can also be observed between the signals when received by the satellite. To highlight the Doppler effect difference expected, we take the example of 868 MHz ISM band. We can then define the Doppler shift difference in time as function of the distance between the object of interest and the interfering object. Their difference equals:

$$f_{D_{\text{diff}}}(t) = f_{D_{\text{obj}}}(t) - f_{D_{\text{inter}}}(t) \tag{4.2}$$

where $f_{D_{\text{obj}}}(t)$ and $f_{D_{\text{inter}}}(t)$ are the Doppler shift corresponding to the object of interest and

to the interfering object respectively. They are both computed using Equation (1.9). $f_{D_{\text{inter}}}(t)$ is computed for different values of the distance between the two objects.

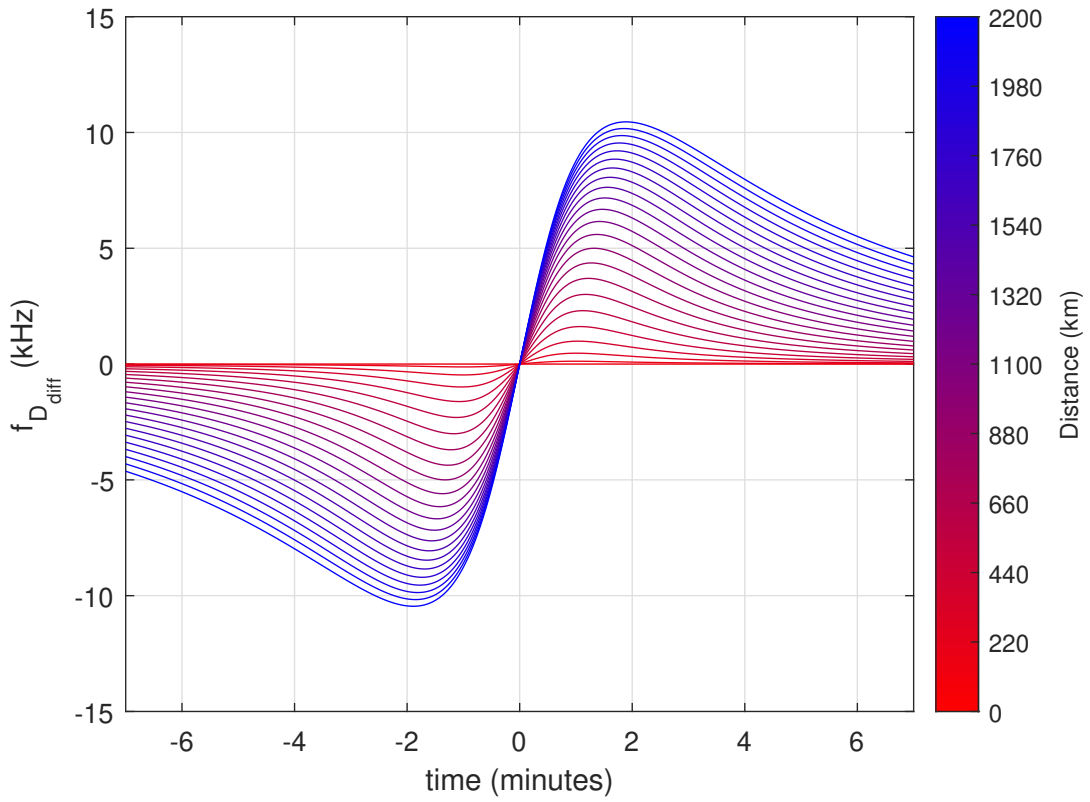

Figure 4.3 – Doppler shift difference profile between the object of interest and an interfering object as function of the distance between both objects

In Figure (4.3), we present the Doppler shift difference profile during the cross visibility time of both objects. We can see that for the frequency band considered, there is no much Doppler shift difference between both objects separated by less than 440 km. For a relative distance range from 660 to about 1320 between two objects, there is an expected frequency shift difference of 2 to 3 kHz during most of the satellite visibility time. Finally, for distance from about 1600 to 2200 km between both objects, a frequency shift difference from 5 to 11 kHz is expected depending on the reception instant during the satellite visibility time. In the following sections, we evaluate our three detectors (A, B and differential) in different relative distance configuration between the object of interest and the interfering object. We first need to investigate the performance of the frequency estimation algorithms that have to be used in detectors A and B.

4.2 Performance evaluation of frequency estimators

In this section we are considering the presence of interference from one object within the system and perfect synchronization with the signal of interest is also assumed. The model of the received signal at the satellite is given by:

$$r(t) = \sqrt{P_0}s(t, \mathbf{a}^{(0)})e^{j(2\pi f_{D_0}(t)t+\theta_0)} + \sqrt{P_1}s(t-\tau_u, \mathbf{a}^{(1)})e^{j(2\pi f_{D_1}(t)t+\theta_1)} + n(t) \tag{4.3}$$

where the term $\sqrt{P_0}s(t, \mathbf{a}^{(0)})e^{j(2\pi f_0 t+\theta_0)}$ corresponds to the signal of interest, the next term represent the interfering signal and $n(t)$ being the realization of a zero-mean wide sense stationary complex circularly symmetric Gaussian noise, independent of the signal, and with double-sided power spectral density $2N_0$. We also define the received signal to interference power ratio by :

$$I = 10\log_{10}\left(\frac{P_0}{P_1}\right) \tag{4.4}$$

As we have presented in Chapter 2, both detectors A and B use frequency estimation algorithms. Initially in their derivations, these algorithms did not consider the presence of interference. Therefore, in this section, we propose to investigate their performance within interference conditions. We consider two frequency estimation algorithms from [60], the ML estimation algorithm by Rife and Boorstyn (was already described and used in Section 2.2) and a simpler but less efficient algorithm referred to as the Kay estimator [63] as we want to investigate the influence of interference on algorithms with different level of complexity. The Kay estimator uses least-squares based method and the frequency estimation $\widehat{f_D}$ is given by :

$$\widehat{f_D} = \frac{1}{2\pi M T_s}\sum_{k=1}^{L_0-1}\omega_k \arg[u(k)u^*(k-1)] \tag{4.5}$$

where the samples $u(k)$ are given by Equation (2.16), L_0 is the total number of samples and $\{\omega_k\}$ are some weighting coefficients given by :

$$\omega_k = \frac{6k(L_0-k)}{L_0(L_0^2-1)} \qquad 1 \leq k \leq L_0-1 \tag{4.6}$$

Details on how to derive this estimator are given in [60] [63]. We then consider one interfering signal with a random delay and different levels of power. In the simulations, the delay settings are set to guarantee that the interference occurs at least on half of the frame of interest. As for power levels, we consider the power ratio I to be -3, 0, 3, 6 and 9 dB. For each of the considered level, we evaluate the performance of the two estimators in terms of the normalised root mean squared error of the estimator (NRMSE) based on 1000 realizations for different levels of SNR. We fix $N_{\text{FFT}} = 512$ for Rife and Boorstyn estimator and the number of samples $L_0 = 8$ for Kay

estimator. The simulation results are given in Figures 4.4 and 4.5.

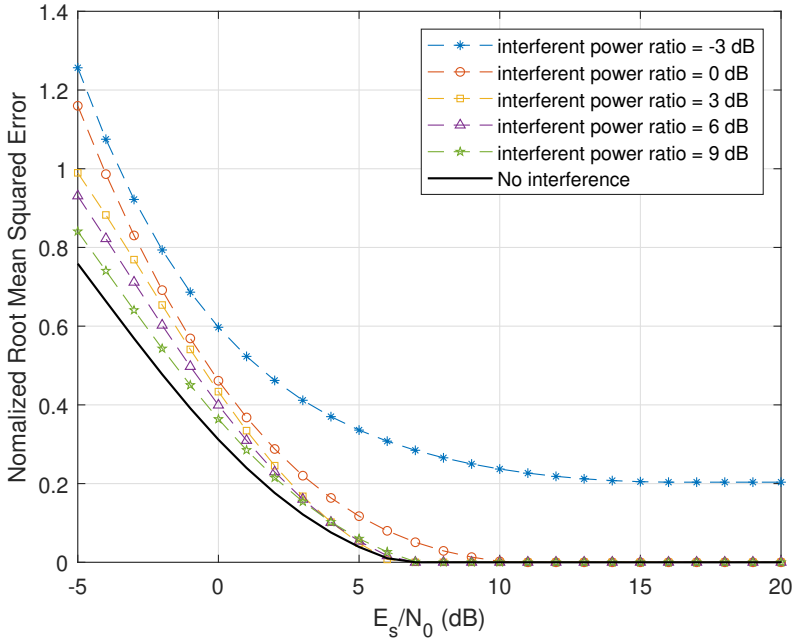

Figure 4.4 – NRMSE of Rife and Boorstyn estimator for different interferent power ratio levels

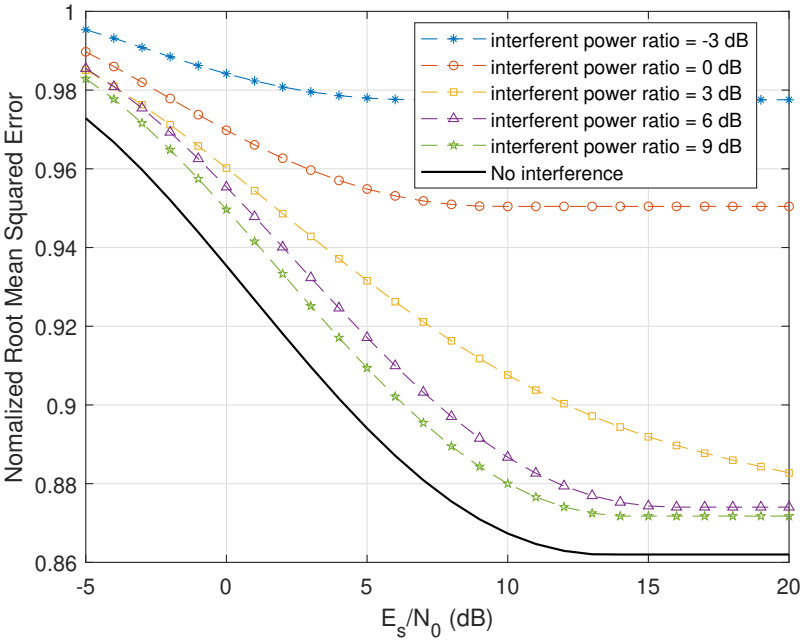

Figure 4.5 – NRMSE of Kay estimator for different interferent power ratio levels

From Figures 4.4, we can see that for Rife and Boorstyn estimator, interference impact on the estimation is only noticed at low levels of SNR for all values of interferent power ratio. However, beyon 5dB of SNR, the interference impact becomes negligible and the performance with received signal to interferent power ratio higher than 0 dB tends to the performance without interference.
On the other hand, we can see that interference impact is much more noticeable for Kay estimator and there is degradation of performance even at high levels of SNR for different levels of interferent power ratio.
These results show that Rife and Boorstyn estimator can still have very good performance even in presence of interference. Based on these results, we can conclude that the frequency estimation part of our detectors A and B should not be a problem when having interference if we use Rife and Boorstyn estimator provided that the interferent power level keeps below the power level of our signal of interest. In the next section, we present the performance of the overall performance of detectors A and B as well as the differential detector in presence of interference.

4.3 Performance evaluation of the proposed receivers

Performance of the three detectors are assessed in terms of BER estimated through Monte-Carlo simulations as a function of the ratio E_b/N_0. We have observed in Chapter 3 that the general behaviour of the three detectors is the almost the same with every different CPM formats. To make the comparison easy and without loss of generality, we only consider the GMSK in this section. The various simulation parameters are the same as presented in Section 2.4.1. We also consider short frame communication so Doppler shift is assumed to be constant over the duration of the frame with $f_D T_s = 0.05$ for the frame of interest.
Hereafter, three scenarios are defined with one interfering object positioned at three possible distances where its power and Doppler shift are adjusted as described in the previous section:

Table 4.1 – Considered interference scenarios for the simulation

Label	Distance between two objects (km)	Received signal to interference power ratio I (dB)	Doppler shift difference ($f_{D_{\text{diff}}} T_s$)
Scenario 1	500	3	0
Scenario 2	1000	6	0.25
Scenario 3	1500	9	0.5

In the simulations, the time delay of the interfering signal τ_1 is randomly chosen but it is configured to guarantee that interference is present at least on half of the frame. The simulation results are given in Figure 4.6.

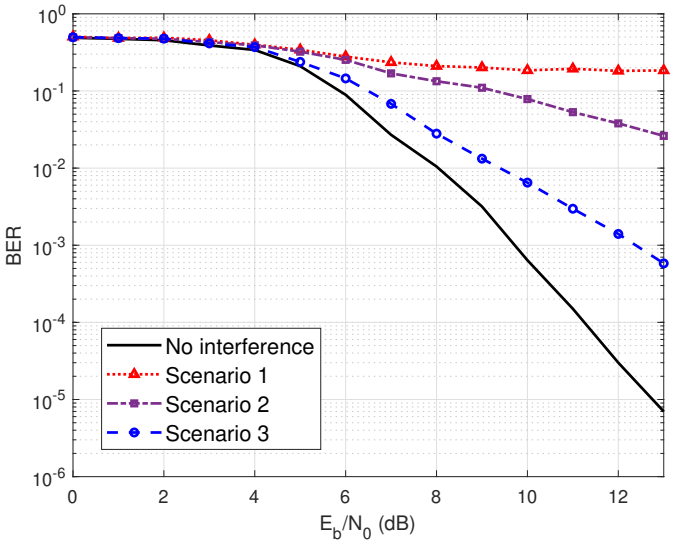

(a) Detector A

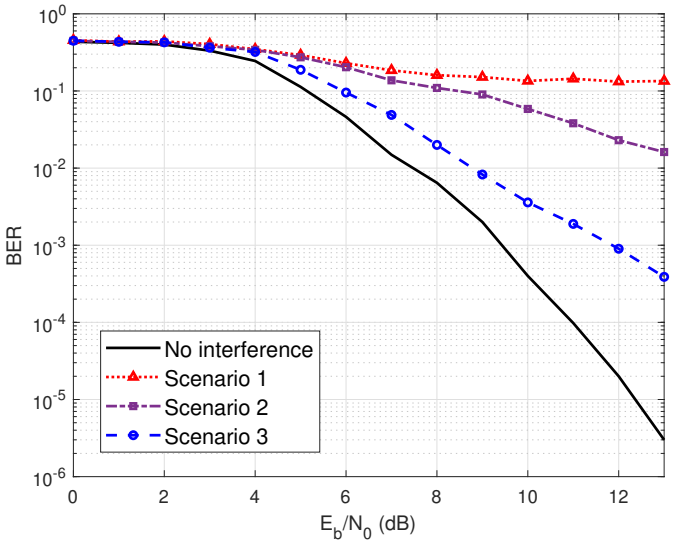

(b) Detector B

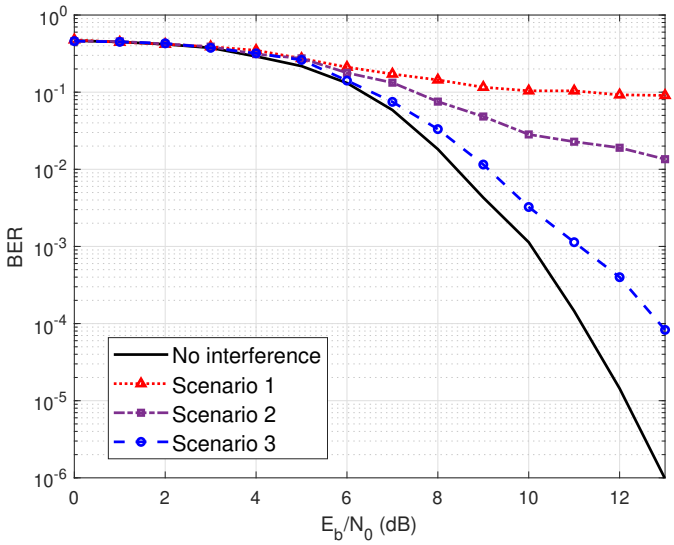

(c) Differential detector

Figure 4.6 – BER comparison of the three detectors for GMSK in the three described scenarios compared to their performance without interference with $f_D T_s = 0.05$ ($N_v = 5$ and $N_D = 8$ for detectors A and B while $K_{opt} = 3$ for the differential detector)

Simulation results for detector A and B show 3 dB of difference between the most favorable scenario (Scenario 3) and the performance in absence of interference at high SNR. This difference is reduced to about 2 dB for the differential detector.
Detection becomes more and more difficult as the interfering object gets closer to the object of interest and for relative distance of 1000 km (Scenario 2), BER barely gets to 10^{-2} in high SNR. Finally, we can see that if the interfering object is close the object of interest (Scenario 1), the detectors are unable to correctly retrieve the useful information and we observe an error floor.
We have also tested the case of two interfering objects and the degradation is much more noticeable. As a conclusion, the three detectors can detect the signal in presence of interference provided that the interfering object is distant enough from the object of interest. Otherwise it is necessary to design a receiver that takes into account the interference presence and processes it or a transmitter that makes the signal detection robust to interference.

4.4 Conclusion

This chapter was dedicated to present the performance of our three detectors when two uncoordinated users interfere in a LEO satellite link. We described the reception setup from the satellite perspective and defined three scenarios corresponding to three relative distance between users. Then, we assessed the performance of the frequency estimation algorithms that can be used in detectors A and B in presence of interference which stated that Rife and Boorstyn estimator is a good estimator choice in such conditions. Finally, we illustrated the performance of our detectors which showed 2 to 3 dB of degradation if the interfering object is distant enough. These results highlight the need to study new algorithms on transmitters or receivers to mitigate the problem of interference.

Conclusions and Perspectives

Conclusions

In this thesis, we were interested in the reception of Continuous Phase Modulation (CPM) signals in the context of Satellite IoT application where heavy Doppler effect is present. We have considered CPM to be a potential good candidate for this type of application because of its good power and spectral properties which result from its constant envelope and continuous phase. However, more aspects of CPM still needs to be investigated before we can confirm the choice of this waveform.

In Chapter 1, we introduced the important elements used to characterize the satellite channel and we studied the Doppler profile in order to evaluate the Doppler shift and Doppler rate to be expected. We also introduced the CPM. After the definition and description of mainly used formats, we gave the trellis representation which is necessary to study the performance (the minimum distance for instance) and to retrieve the symbols from the signal. We then focused on the used state of the art detection algorithms either coherent or non coherent. Taking into account the Satellite IoT context, we particularly dealt with non coherent detection with reduced complexity and we thus detailed Non-coherent Sequence Detection (NSD) and differential detection algorithms.

In Chapter 2, we addressed the problem of Doppler compensation in non coherent CPM detection which was not really addressed in the literature. We exploited the NSD detection criterion and coupled it with the generalized maximum likelihood method which enabled us to simplify the detection problem. Then, using a *Per Survivor Processing* (PSP) technique on the detection trellis, we were able to make a blind detection in presence of Doppler without pilot symbols. We finally derived two detectors with different levels of complexity, the first one (A) uses the linear Pulse Amplitude Modulation (PAM) decomposition of the CPM and the second one (B) uses the exact expression of the signal at the expense of a higher computation cost. Simulations confirmed the robustness of these detectors to small Doppler shifts, and to higher Doppler shifts for Detector B. Both detectors are also robust against Doppler rate thanks to the sliding frequency estimation window.

In Chapter 3, we tackled the problem of complexity together with the Doppler compensation at the reception side in a blind way. To this end, we proposed a delay-optimized differential detection algorithm. It is based on the product of the received signal by a delayed conjugate version of it. The originality is the use of a delay higher than one symbol period. We introduced the

modified trellis representation associated to the resulting differential signal. We also proposed an optimization criterion fr the delay value based on the minimum Euclidean distance between two differential signals. We gave the optimized delay value for different CPM formats and simulations assessed their accuracy. Finally, we evaluated the robustness of the proposed delay optimized differential receiver against Doppler effect. Simulations confirm that the optimized differential detector can withstand a range of Doppler shift and for extremely high orders, usage of few pilot symbols with low-complexity DA estimation can keep the performance at good level. The differential detector is also compared to detectors A and B from previous chapter in terms of performance / complexity. Simulations also showed that the differential detector performs better in the high SNR / low error rate regime, while keeping a low complexity.

In Chapter 4, we investigated the performance of our three detectors in presence of one interfering object in the neighborhood of the object of interest. We started this chapter by presenting the reception scenario. We studied the power and Doppler difference between the object of interest and the interfering object. We then assessed the performance of the frequency estimator used in detectors A and B in interference conditions. Simulations showed that the Rife and Boorstyn algorithm can still perform correctly even in presence of interference. We finally assessed the performance of our detectors and results have showed the importance of introducing a multiuser detection solution. Simulations proved that the three detectors behave the same in presence of an interfering object. Performance keeps satisfactory as long as the interfering object is distant enough from the target object but it severely degrades when it gets close. In this case, multiple access techniques either at the transmitter or the receiver (multiuser detection) should be applied to deal with interference.

Perspectives

In order to chose the most convenient detector for our considered application from all of the presented detectors, we should extend the comparison between them by adding adapted forward error correction (FEC) codes to each detector to further broaden the performance/complexity comparison and evaluate the gains that can be obtained.

On the other hand, performance results that we presented in Chapter 4 showed the importance of implementing a solution to mitigate the problem of interference as a short term prospect. In this context, a direct solution we can propose would be testing an iterative detection method like the Successive Interference Cancellation (SIC) algorithm [64] in conjunction with our receivers (A, B and optimized delay differential). Another approach is to go back to the detection criterion of every proposed receiver to take into account the interference model. We may also investigate the possibility of separating the signals coming from close objects within

a given geographical zone by creating some sort orthogonality between them (by varying the modulation index h for instance) or by scheduling their access to the channel while keeping in mind the constraint of complexity due to the limited power of the communicating objects. This include the usage of some optimized random access solutions where we can mention the Contention Resolution Diversity Slotted ALOHA (CRDSA) technique [65] and investigate its potential with CPM. We can also consider investigating the spread spectrum technique as well [66] to be used with CPM to mitigate the interference problem.

In the mid term perspective, a comparison between our CPM detectors and the newly emerging techniques in the context of Satellite IoT application, in terms of performance, complexity and bandwidth must be made to confirm the choice of CPM as an adequate solution to this application. These techniques include the optimized NB-IoT for LEO satellite usage [67] [68] or the newly released LR-FHSS standard by Semtech [8] [69] for the application of Satellite IoT.

Finally, in the long term, we highlight the importance of investigating the time synchronization problematic since it intervenes in every step of the detection especially if iterative algorithms are considered for the multiuser detection. Most of the efficient time synchronization solutions with CPM use data-aided method and require certain length of the pilot sequence like in [70]. However, pilot length is limited in our application and the influence of the time synchronization errors has to be investigated. We can also investigate the performance of blind time synchronization techniques (as in [71]) with our detectors.

List of publications

International Journal

- A. Jerbi, K. Amis, F. Guilloud and T. Benaddi, "Delay Optimization of Conventional Non-Coherent Differential CPM Detection," in IEEE Communications Letters, vol. 27, no. 1, pp. 234-238, Jan. 2023, doi: 10.1109/LCOMM.2022.3220326.

International Conference

- A. Jerbi, F. Guilloud, K. Amis and T. Benaddi, "Non-coherent CPM Detection under Gaussian Channel affected with Doppler Shift," 2022 IEEE 33rd Annual International Symposium on Personal, Indoor and Mobile Radio Communications (PIMRC), Kyoto, Japan, 2022, pp. 1338-1343, doi: 10.1109/PIMRC54779.2022.9978066.

National Conference

- Anouar Jerbi, Karine Amis, Frédéric Guilloud, Tarik Benaddi. Détection non-cohérente des modulations CPM en présence d'un décalage Doppler. GRETSI'22 : 28ème colloque du Groupement de Recherche en Traitement du Signal et des Images, Sep 2022, Nancy, France, Sep 2022, Nancy, France. hal-03758421f

Appendices

Appendix A

Low Power Wide Area Network technologies

Low Power Wide Area Network (LPWAN) seek to provide a service relating to a particular use of the Internet of Things [72] [73]: relatively low bit rate communication but unlike lower-coverage networks commonly used in home automation (Bluetooth Low Energy or ZigBee, for example), LPWANs are characterized by their scale of application. Terminals of LPWAN networks can benefit from a large coverage, going up to several tens of kilometers around the access point. In addition, these networks are optimized to limit the energy consumption of the terminals.

Various domains of applications can benefit from LPWAN technologies. This includes agriculture, transport and various *Smart* projects like *Smart Cities*, *Smart Grid*, *Smart Homes*, etc. In all these applications, we seek to provide access over a very long distance, in order to cover white areas for existing networks (areas difficult to access, basements, or sparsely populated countryside). By increasing the maximum possible distance between terminals and ground stations, it becomes easier for operators to cover a territory, and therefore to increase the number of potential customers while reducing the number of ground stations required.

Many LPWAN technologies exists today each having their advantages and drawbacks. Some technologies operates in the ISM bands (Industrial, Scientific and Medical), which are free to access under certain power transmission conditions, while other technologies operates in regulated bands. The free bands most used for the Internet of Things are located around 868 MHz and 2.4 GHz. In the following, we give an overview of some of the most used LPWAN technologies, SigFox, LoRa and NB-IoT. Table 2 summarizes some of the principal characteristics of these three LPWAN technologies.

— SigFox [74] : is a French company which operates an LPWAN network, and plays the role of access provider. Their technology also takes the name of the company. The information available is mainly taken from commercial presentations from SigFox. To date, the network is particularly developed in Europe. The technology used by SigFox is based on Ultra Narrow-Band (UNB), a proprietary solution in the 868 MHz free band. The bandwidth used in the transmissions is 100 Hz. The use of such a thin band limits the symbol rate to 100 Baud, but greatly increases the link budget, so that a large coverage is ensured without using coding. In order to ensure the demodulation of a message without the presence of interference, the messages are repeated three times, on three different central frequencies

considered as random. The use of the free band limits the maximum number of messages per terminal to 14 per day. A downlink from the central node to the terminals is also available.

— LoRa [75]: acronym for *Long Range*, is a technology based on frequency spreading using Chirp Spread Spectrum. Messages can be transmitted at different spreading factors (denoted SF, for Spreading Factor), ranging from 7 to 12, and on different carrier sizes, ranging from 125 to 500 kHz. A LoRa symbol, whose duration is inversely proportional to the carrier used, is represented by a continuous phase signal whose frequency varies linearly in the considered subcarrier [76]. An information bit is carried by SF LoRa symbols. Thus the greater the value of SF chosen, the lower the spectral efficiency. This reduces throughput and makes transmissions more robust to interference. Moreover, the modulation uses a coding whose rate can vary between 1/2 and 4/5. A link from the central gateway to the terminal is possible which consist of a reception window opened by the terminal after each transmission [77]. This modulation is coupled with the LoRaWAN communication protocol, open source, promoted by the LoRa Alliance, an open consortium that seeks to standardize the use of technology. Each user can administer their own LoRa network and make it compatible with that of other users, provided they purchase specific terminals and follow the protocol.

— NB-IoT [78]: arrived on the market much later than most LPWAN technologies, NB-IoT was proposed by the standardization organization 3GPP in its version 13 (3rd Generation Partnership Project, Release 13) as an extension of LTE in June 2016 [79] . This is a standard that is used by existing telecom operators on regulated frequency bands. To date, the network is operational in several European countries, as well as in Brazil, China and the United States [80]. This standard is based on a strong re-use of the technologies mastered in the previous versions of the 4G standard, both at the level of the terminals and the infrastructure network of the operators.

Table 2 – Main characteristics of some LPWAN technologies

	SigFox	LoRa	NB-IoT
Solution type	Privately owned	Open	Standardized
Key technology	Ultra Narrow-Band	Spread Spectrum	Narrow-Band
Modulation	DBPSK	CSS	BPSK / QPSK in SC-FDMA mode
Frequency band	ISM	ISM	Licensed
Bandwidth	100 Hz	125 to 500 kHz	3.75 to 180 kHz
Channel access	Unslotted ALOHA	Unslotted ALOHA	MF-TDMA
Available link budget	158 dB	154 dB	164 dB
Bitrate	100 b/s	0.3 to 40 kb/s	0.1 to 250 kb/s

APPENDIX B

Analytical expressions of $h_k(t)$ and $\alpha_{k,i}$:

The derivation of analytical expressions of the linear components $h_k(t)$ and pseudo symbols $\alpha_{k,i}$ could be found in [49]. Here, we present the final results expressions.
The signal $s(t, \mathbf{a})$ of Equation (1.12) is decomposed as :

$$s(t, \mathbf{a}) = \sqrt{\frac{2E_s}{T_s}} \sum_{k=0}^{K_T-1} \sum_{i=0}^{N-1} \alpha_{k,i} h_k(t - iT_s) \tag{B.1}$$

with $K_T = Q^P(2^P - 1)$ and $Q = 2^{L-1}$. As for P, it is the integer that verifies :

$$2^{P-1} < M \leq 2^P \tag{B.2}$$

If M is a power of 2, then $P = \log_2(M)$.
The functions $h_k(t)$ and the terms $\{\alpha_{k,i}\}_{\substack{0 \leq k \leq K_T-1 \\ 0 \leq i \leq N-1}}$ are given respectively by:

$$h_k(t) = \prod_{l=0}^{P-1} c^{(l)}_{d_{j,l}}(t + e^{(m)}_{j,l} T_s) \tag{B.3}$$

$$\alpha_{k,i} = \prod_{l=0}^{P-1} b^{(l)}_{d_{j,l}, i - e^{(m)}_{j,l}} \tag{B.4}$$

In both equations, integers j and m are related to counter k by the following equation :

$$k = m + \sum_{u=0}^{j-1} Y_u, \quad \text{with} \quad 0 \leq j \leq Q^P - 1, \quad 0 \leq m \leq Y_j - 1 \tag{B.5}$$

In equation (B.5), the terms Y_j are given by

$$Y_j = \prod_{l=0}^{P-1} D_{j,l} - \prod_{l=0}^{P-1} (D_{j,l} - 1) \tag{B.6}$$

with $D_{j,l}$ being the duration in symbols length of the Laurent component $c^{(l)}_{d_{j,l}}(t)$ present in (1.21) which is given by :

$$c^{(l)}_v(t) = \prod_{i=0}^{L-1} u^{(l)}(t + iT_s + \beta_{v,i}LT_s), \qquad 0 \leq m \leq Q-1 \tag{B.7}$$

$$u^{(l)}(t) = \begin{cases} \frac{\sin(2^{l+1}h\pi q(t))}{sin(2^l h\pi)}, & 0 \leq t \leq LT_s \\ u^{(l)}(2LT_s - t), & 0 < t \leq 2LT_s \\ 0, & \text{otherwise} \end{cases} \tag{B.8}$$

and having an indexes $\{d_{j,l}\}_{\substack{0\leq j\leq Q^P-1 \\ 0\leq l\leq P-1}}$ which are the coefficients of the radix-Q representation of the integer j, in other words they are obtained from the following equation:

$$j = \sum_{l=0}^{P-1} Q^l d_{j,l}, \qquad d_{j,l} \in \{0, 1, .., Q-1\} \tag{B.9}$$

The coefficients $\{\beta_{v,i}\}_{\substack{0\leq v\leq Q-1 \\ 0\leq i\leq L-1}}$ in equation (B.7) take on values 0 or 1 and are also obtained from the binary representation of v :

$$v = \sum_{i=0}^{L-1} 2^{i-1}\beta_{v,i} \tag{B.10}$$

Going back to the term $b^{(l)}_{d_{j,l},i-e^{(m)}_{j,l}}$ in the pseudo symbols equation (1.22), it is given by :

$$b^{(l)}_{v,i} = \exp\left(j2^l h\pi \left[\sum_{w=0}^{i} \gamma_{w,l} - \sum_{q=0}^{L-1} \gamma_{i-q,l}\beta_{v,i}\right]\right) \tag{B.11}$$

with the sequence $\{\gamma_{i,l}\}$ being derived from the original symbol sequence $\mathbf{a}$ using the following equation :

$$a_i = \sum_{l=0}^{P-1} \gamma_{i,l} 2^l \tag{B.12}$$

Finally, the terms $\{e^{(m)}_{j,l}\}$ also in the equation (1.22) are obtained by satisfying these equations :

$$0 \leq e^{(m)}_{j,l} \leq D_{j,l} - 1, \qquad 0 \leq l \leq P-1 \tag{B.13}$$

$$\prod_{l=0}^{P-1} e^{(m)}_{j,l} = 0 \tag{B.14}$$

APPENDIX C

C. 1. Autocorrelation of the noise term $N_K(t)$:

The calculation of the autocorrelation of the noise term $N_K(t)$ given by the equation (3.4) is detailed below :

$$\begin{aligned} E[N_K(t)N_K^*(t-\tau)] &= E\Big[\Big(U_K(t)+W_K(t)\Big)\Big(U_K^*(t-\tau)+W_K^*(t-\tau)\Big)\Big] \\ &= E[U_K(t)U_K^*(t-\tau)] + E[W_K(t)W_K^*(t-\tau)] + \underbrace{2\Re\Big(E(U_K(t)W_K^*(t-\tau))\Big)}_{=0 \text{ since } U_K(t) \text{ and } W_K(t) \text{ are uncorrelated}} \end{aligned}$$

and then let $A = |s(t,\mathbf{a})|$, thus the first term gives :

$$\begin{aligned} E[U_K(t)U_K^*(t-\tau)] &= E\Big[\frac{1}{2}\Big(s(t,\mathbf{a})e^{j\psi}n^*(t-KT_s) + n(t)s^*(t-KT_s,\mathbf{a})e^{-j\psi}\Big)\times\dots \\ &\quad \frac{1}{2}\Big(s^*(t-\tau,\mathbf{a})e^{-j\psi}n(t-\tau-KT_s) + n^*(t-\tau)s(t-\tau-KT_s,\mathbf{a})e^{j\psi}\Big)\Big] \\ &= \frac{1}{4}\underbrace{E[s(t,\mathbf{a})s^*(t-\tau,\mathbf{a})n(t-\tau-KT_s)n^*(t-KT_s)]}_{=2N_0A^2\delta(\tau)} \\ &\quad +\frac{1}{4}\underbrace{E[s(t,\mathbf{a})s(t-\tau-KT_s,\mathbf{a})e^{j2\psi}n^*(t-KT_s)n^*(t-\tau)]}_{=0} \\ &\quad +\frac{1}{4}\underbrace{E[n(t)n(t-\tau-KT_s)s^*(t-KT_s,\mathbf{a})s^*(t-\tau,\mathbf{a})e^{-j2\psi}]}_{=0} \\ &\quad +\frac{1}{4}\underbrace{E[n(t)n^*(t-\tau)s(t-\tau-KT_s,\mathbf{a})s^*(t-KT_s,\mathbf{a})]}_{=2N_0A^2\delta(\tau)} \\ &= N_0A^2\delta(\tau) \end{aligned}$$

and the second term gives :

$$\begin{aligned} E[W_K(t)W_K^*(t-\tau)] &= E\Big(\frac{1}{2}n(t)n^*(t-KT_s)\frac{1}{2}n^*(t-\tau)n(t-\tau-KT_s)\Big) \\ &= \frac{(2N_0)^2}{4}\delta(\tau) = N_0^2\delta(\tau) \end{aligned}$$

C. 2. Transition from equation (3.10) to equation (3.11) :

In the event of an error, we have the following inequality :

$$\int_0^{NT_s} |R_K(t) - S_K(t,\tilde{\mathbf{a}})|^2 dt \leq \int_0^{NT_s} |R_K(t) - S_K(t,\mathbf{a})|^2 dt$$

and the term $R_K(t)$ is given by $R_K(t) = S_K(t,\mathbf{a}) + N_K(t)$ with $N_K(t) = U_K(t) + W_K(t)$ so equation (3.10) translates into :

$$\begin{aligned}
\int_0^{NT_s} |S_K(t,\mathbf{a}) - S_K(t,\tilde{\mathbf{a}}) + N_K(t)|^2 dt &\leq \int_0^{NT_s} |N_K(t)|^2 dt \\
\int_0^{NT_s} 2\Re\Big(\Big(S_K(t,\mathbf{a}) - S_K(t,\tilde{\mathbf{a}}\Big)N_K(t)\Big) dt &\leq -\int_0^{NT_s} |S_K(t,\mathbf{a}) - S_K(t,\tilde{\mathbf{a}})|^2 dt \\
\int_0^{NT_s} \Re\Big(\Big(S_K(t,\mathbf{a}) - S_K(t,\tilde{\mathbf{a}}\Big)N_K(t)\Big) dt &\geq \frac{1}{2}\int_0^{NT_s} |S_K(t,\mathbf{a}) - S_K(t,\tilde{\mathbf{a}})|^2 dt
\end{aligned}$$

from there, let $Z_K = \int_0^{NT_s} \Re\Big(\Big(S_K(t,\mathbf{a}) - S_K(t,\tilde{\mathbf{a}})\Big)N_K^*(t)\Big) dt$ and the right hand side is known as the squared Euclidean distance which denoted as $\Delta_K^2(\mathbf{a},\tilde{\mathbf{a}})$, so finally we have :

$$Z_K \geq \frac{1}{2}\Delta_K^2(\mathbf{a},\tilde{\mathbf{a}})$$

C. 3. Calculation of the normalized squared Euclidean distance :

E_s denotes the average energy per information symbol in the CPM signal and E_b denotes the average energy per information bit and clearly, $E_s = \log_2(M)E_b$. On the other hand, ε_b denotes the average energy per information bit in the differential signal, and considering the equation of the differential signal (3.2), ε_b is given by :

$$\varepsilon_b = \frac{\log_2(M)E_b^2}{T_s}$$

The squared Euclidean distance is given by :

$$\begin{aligned}
\Delta_K^2(\mathbf{a},\tilde{\mathbf{a}}) &= \int_0^{NT_s} |S_K(t,\mathbf{a}) - S_K(t,\tilde{\mathbf{a}})|^2 \, dt \\
&= \left(\frac{E_s}{T_s}\right)^2 \int_0^{NT_s} \left|e^{j\Theta_K(t,\mathbf{a})} - e^{j\Theta_K(t,\tilde{\mathbf{a}})}\right|^2 dt \\
&= \left(\frac{E_s}{T_s}\right)^2 \int_0^{NT_s} 2\Big(1 - \cos\Big(\Theta_K(t,\mathbf{a}) - \Theta_K(t,\tilde{\mathbf{a}})\Big)\Big) dt \\
&= 2\left(\frac{E_s}{T_s}\right)^2 \int_0^{NT_s} [1 - \cos(\Theta_K(t,\mathbf{e}))] dt
\end{aligned}$$

where $\mathbf{e} = \mathbf{a} - \tilde{\mathbf{a}}$. The normalized squared Euclidean distance $d_K^2(\mathbf{a}, \tilde{\mathbf{a}})$ is $\Delta_K^2(\mathbf{a}, \tilde{\mathbf{a}})$ normalized by $2\varepsilon_b$ and therefore, it is given by :

$$\begin{aligned} d_K^2(\mathbf{a}, \tilde{\mathbf{a}}) &= \frac{\Delta_K^2(\mathbf{a}, \tilde{\mathbf{a}})}{2\varepsilon_b} \\ &= \frac{1}{\varepsilon_b}\left(\frac{E_s}{T_s}\right)^2 \int_0^{NT_s} [1 - \cos\left(\Theta_K(t, \mathbf{e})\right)] dt \\ &= \frac{\log_2(M)}{T_s} \int_0^{NT_s} [1 - \cos\left(\Theta_K(t, \mathbf{e})\right)] dt \end{aligned}$$

BIBLIOGRAPHY

[1] J. A. Fraire, S. Céspedes, and N. Accettura, "Direct-to-satellite IoT - a survey of the state of the art and future research perspectives," in *Ad-Hoc, Mobile, and Wireless Networks*. Springer Int. Publishing, 2019, pp. 241–258.

[2] P. Remlein, "Energy efficient continuous phase modulation signals for satellite intelligent transportation systems," *IET Circuits, Devices Systems*, vol. 8, pp. 406–411, 09 2014.

[3] S. Cioni, B. Beidas, U. Bie, A. Ginesi, R. Iyer-Seshadri, P. Kim, D. Oh, A. Noerpel, M. Papaleo, A. Vanelli-Coralli, and L. Lee, "Continuous phase modulation for broadband satellite communications: design and trade-offs," *International Journal of Satellite Communications and Networking*, vol. 31, 03 2013.

[4] R. Chaggara, M.-L. Boucheret, C. Bazile, E. Bouisson, A. Ducasse, and J. Gayrard, "Continuous phase modulations for future satellite communication systems," in *2004 12th European Signal Processing Conference*, 2004, pp. 1083–1086.

[5] R. Chaggara, M. Boucheret, C. Bazile, E. Bouisson, A. Ducasse, and J.-D. Gayrard, "Adaptive waveform based on continuous phase modulations design and performance," in *IEEE 5th Workshop on Signal Processing Advances in Wireless Communications, 2004.*, 2004, pp. 41–45.

[6] R. Chaggara, M. Boucheret, C. Bazile, E. Bouisson, A. Ducasse, and J. Gayrard, "Continuous phase modulation for future satellite communication systems in ka band," in *Proceedings. 2004 International Conference on Information and Communication Technologies: From Theory to Applications, 2004.*, 2004, pp. 269–270.

[7] D. B. A.-. (03/11), *DVB-RCS2 Lower Layer Satellite Specification.* DVB, Jul 2018.

[8] G. Boquet, P. Tuset-Peiró, F. Adelantado, T. Watteyne, and X. Vilajosana, "Lr-fhss: Overview and performance analysis," *IEEE Communications Magazine*, vol. 59, no. 3, pp. 30–36, 2021.

[9] G. Colavolpe, R. Raheli, and G. Picchi, "Detection of linear modulations in the presence of strong phase and frequency instabilities," in *IEEE Int. Conf. on Communications.*, vol. 2, 2000, pp. 633–637.

[10] G. Colavolpe and R. Raheli, "Noncoherent Sequence Detection of Continuous Phase Modulations," *IEEE Transactions on Communications*, vol. 47, no. 9, pp. 1303–1307, 1999.

[11] H. L. V. Trees, *Detection, estimation and modulation theory.* New York: John Wiley & Sons, vol. I, 1968.

[12] H. Meyr, M. Oerder, and A. Polydoros, "On sampling rate, analog prefiltering, and sufficient statistics for digital receivers," *IEEE Trans. on Commun.*, vol. 42, no. 12, pp. 3208–3214, 1994.

[13] D. Makrakis and K. Feher, "Multiple Differential Detection of Continuous Phase Modulation signals," *IEEE Transactions on Vehicular Technology*, vol. 42, no. 2, pp. 186–196, 1993.

[14] J. B. Anderson, T. Aulin, and C. Sundberg, *Digital Phase Modulation. Applications of Communications Theory.* Springer US, 1986.

[15] M. Simon and C. Wang, "Differential Versus Limiter - Discriminator Detection of Narrow-Band FM," *IEEE Transactions on Communications*, vol. 31, no. 11, pp. 1227–1234, 1983.

[16] S. Dodson., "The internet of things," https://www.theguardian.com/technology/2003/oct/09/shopping.newmedia, online press article 2003.

[17] "Recommendation itu-t y.4000/y.2060." June 2012.

[18] F. Delli Priscoli, "Network aspects relevant to the integration between the gsm network and a satellite system," in *Proceedings of 2nd IEEE International Conference on Universal Personal Communications*, vol. 1, 1993, pp. 339–343 vol.1.

[19] A. Zaidi and M. Suddle, "Global navigation satellite systems: A survey," in *2006 International Conference on Advances in Space Technologies*, 2006, pp. 84–87.

[20] S. D. Ilcev, "Low earth orbits (leo)," in *2010 20th International Crimean Conference "Microwave Telecommunication Technology"*, 2010, pp. 406–408.

[21] "Iridium satellite communications, network," https://www.iridium.com/network/.

[22] C. Fossa, R. Raines, G. Gunsch, and M. Temple, "An overview of the iridium (r) low earth orbit (leo) satellite system," in *Proceedings of the IEEE 1998 National Aerospace and Electronics Conference. NAECON 1998. Celebrating 50 Years (Cat. No.98CH36185)*, 1998, pp. 152–159.

[23] I. Ali, N. Al-Dhahir, and J. Hershey, "Predicting the visibility of leo satellites," *IEEE Transactions on Aerospace and Electronic Systems*, vol. 35, no. 4, pp. 1183–1190, 1999.

[24] "Satellite lithium-ion batteries," https://www.sciencedirect.com/topics/engineering/low-earth-orbit, available online.

[25] D. Barbarić, J. Vuković, and D. Babic, "Link budget analysis for a proposed cubesat earth observation mission," in *2018 41st International Convention on Information and Communication Technology, Electronics and Microelectronics (MIPRO)*, 2018, pp. 0133–0138.

[26] M. Bousquet. and G. Maral, *Satellite Communications Systems: Systems, Techniques and Technology.* Wiley Series in Communication and Distributed Systems., 2009.

[27] M. Conti, A. Guidotti, C. Amatetti, and A. Vanelli-Coralli, "Nb-iot over non-terrestrial networks: Link budget analysis," in *GLOBECOM 2020 - 2020 IEEE Global Communications Conference*, 2020, pp. 1–6.

[28] O. Kodheli, N. Maturo, S. Andrenacci, S. Chatzinotas, and F. Zimmer, "Link budget analysis for satellite-based narrowband IoT systems," in *Ad-Hoc, Mobile, and Wireless Networks.* Springer International Publishing, 2019, pp. 259–271. [Online]. Available: https://doi.org/10.10072F978-3-030-31831-4_18

[29] S. CLUZEL, *Système M2M/IoT par satellite pour l'hybridation d'un réseau NB-IoT via une constellation LEO.* PhD Thesis, 2019.

[30] H. Chougrani, S. Kisseleff, W. A. Martins, and S. Chatzinotas, "Nb-iot random access for nonterrestrial networks: Preamble detection and uplink synchronization," *IEEE Internet of Things Journal*, vol. 9, no. 16, pp. 14 913–14 927, 2022.

[31] "Eutelsat, satellite iot: A compliment to cellular," https://www.eutelsat.com/en/blog/satellite-iot-complementing-cellular.html, available online.

[32] I. Ali, N. Al-Dhahir, and J. Hershey, "Doppler characterization for leo satellites," *IEEE Transactions on Communications*, vol. 46, no. 3, pp. 309–313, 1998.

[33] M. Katayama, A. Ogawa, and N. Morinaga, "Carrier synchronization under doppler shift of the nongeostationary satellite communication systems," in *[Proceedings] Singapore ICCS/ISITA '92*, 1992, pp. 466–470 vol.2.

[34] A. O. Masaaki Katayama and N. Morinaga, "Earth satellite communication systems with low orbits, and effects of the doppler shift," *Electronics and Communications in Japan (Part I: Communications)*, 1994.

[35] E. Vilar and J. Austin, "Analysis and correction techniques of doppler shift for non-geosynchronous communication satellites," *International Journal of Satellite Communications*, 1991.

[36] T. Aulin and C. Sundberg, "Continuous phase modulation - part i: Full response signaling," *IEEE Transactions on Communications*, vol. 29, no. 3, pp. 196–209, 1981.

[37] T. Aulin, N. Rydbeck, and C.-E. Sundberg, "Continuous phase modulation - part ii: Partial response signaling," *IEEE Transactions on Communications*, vol. 29, no. 3, pp. 210–225, 1981.

[38] M. Geoghegan, "Description and performance results for a multi-h cpm telemetry waveform," in *MILCOM 2000 Proceedings. 21st Century Military Communications. Architectures and Technologies for Information Superiority (Cat. No.00CH37155)*, vol. 1, 2000, pp. 353–357 vol.1.

[39] A.-N. Premji and D. Taylor, "A practical receiver structure for multi-h cpm signals," *IEEE Transactions on Communications*, vol. 35, no. 9, pp. 901–908, 1987.

[40] E. T. . . V8.4.0, "Digital cellular telecommunications system (phase 2+); modulation (3gpp ts 05.04 version 8.4.0 release 1999)."

[41] A. Perotti, A. Tarable, S. Benedetto, and G. Montorsi, "Capacity-achieving cpm schemes," *IEEE Transactions on Information Theory*, vol. 56, no. 4, pp. 1521–1541, 2010.

[42] M. Geoghegan, "Implementation and performance results for trellis detection of soqpsk," 2001.

[43] B. Rimoldi, "A decomposition approach to CPM," *IEEE Transactions on Information Theory*, vol. 34, no. 2, pp. 260–270, 1988.

[44] P. Moqvist and T. Aulin, "Orthogonalization by principal components applied to cpm," *IEEE Transactions on Communications*, vol. 51, no. 11, pp. 1838–1845, 2003.

[45] Q. Zhao and G. Stuber, "Robust time and phase synchronization for continuous phase modulation," *IEEE Transactions on Communications*, vol. 54, no. 10, pp. 1857–1869, 2006.

[46] E. Perrins and M. Rice, "Optimal and reduced complexity receivers for m-ary multi-h cpm," in *2004 IEEE Wireless Communications and Networking Conference (IEEE Cat. No.04TH8733)*, vol. 2, 2004, pp. 1165–1170 Vol.2.

[47] M. P. Wylie-green, "A new pam decomposition for continuous phase modulation," in *2006 40th Annual Conference on Information Sciences and Systems*, 2006, pp. 705–710.

[48] P. Laurent, "Exact and approximate construction of digital phase modulations by superposition of amplitude modulated pulses (AMP)," *IEEE Trans. on Commun.*, vol. 34, no. 2, pp. 150–160, 1986.

[49] U. Mengali and M. Morelli, "Decomposition of M-ary CPM signals into PAM waveforms," *IEEE Trans. on Inf. Theory*, vol. 41, no. 5, pp. 1265–1275, 1995.

[50] G. Forney, "The viterbi algorithm," *Proceedings of the IEEE*, vol. 61, no. 3, pp. 268–278, 1973.

[51] L. Bahl, J. Cocke, F. Jelinek, and J. Raviv, "Optimal decoding of linear codes for minimizing symbol error rate (corresp.)," *IEEE Transactions on Information Theory*, vol. 20, no. 2, pp. 284–287, 1974.

[52] J. G. Proakis, *Digital Communications, Fourth Edition.* Mc Graw Hill Edition, 2001.

[53] G. Colavolpe and R. Raheli, "Noncoherent sequence detection," *IEEE Trans. on Commun.*, vol. 47, no. 9, pp. 1376–1385, 1999.

[54] N. Svensson and C.-E. Sundberg, "Performance evaluation of Differential and Discriminator Detection of Continuous Phase Modulation," *IEEE Transactions on Vehicular Technology*, vol. 35, no. 3, pp. 106–117, 1986.

[55] G. Kawas Kaleh, "Differential Detection of Partial Response Continuous Phase Modulation with index 0.5," in *IEEE 39th Vehicular Technology Conference*, 1989, pp. 115–121 vol.1.

[56] D. Makrakis and P. Mathiopoulos, "Differential Detection of correlative encoded Continuous Phase Modulation schemes using Decision Feedback," in *IEEE Int. Conf. on Communications*, 1990, pp. 619–625 vol.2.

[57] F. Jager and C. Dekker, "Tamed frequency modulation, a novel method to achieve spectrum economy in digital transmission," *IEEE Transactions on Communications*, vol. 26, no. 5, pp. 534–542, 1978.

[58] S. Miller and R. O'Dea, "Multiple symbol noncoherent detection of gmsk," in *ICC '98. 1998 IEEE International Conference on Communications. Conference Record. Affiliated with SUPERCOMM'98 (Cat. No.98CH36220)*, vol. 3, 1998, pp. 1676–1680 vol.3.

[59] A. Abrardo, G. Benelli, and G. Cau, "Multiple-symbol differential detection of gmsk for mobile communications," *IEEE Transactions on Vehicular Technology*, vol. 44, no. 3, pp. 379–389, 1995.

[60] M. Morelli and U. Mengali, "Feedforward frequency estimation for PSK: a tutorial review," *Eur. Trans. Telecommun.*, vol. 9, pp. 103–116, 1998.

[61] D. C. Rife and R. R. Boorstyn, "Single tone parameter estimation from discrete-time observations," *IEEE Trans. Inf. Theory*, vol. 20, pp. 591–598, 1974.

[62] S. Tretter, "Estimating the frequency of a noisy sinusoid by linear regression (corresp.)," *IEEE Transactions on Information Theory*, vol. 31, no. 6, pp. 832–835, 1985.

[63] S. Kay, "A fast and accurate single frequency estimator," *IEEE Transactions on Acoustics, Speech, and Signal Processing*, vol. 37, no. 12, pp. 1987–1990, 1989.

[64] P. Patel and J. Holtzman, "Analysis of a simple successive interference cancellation scheme in a ds/cdma system," *IEEE Journal on Selected Areas in Communications*, vol. 12, no. 5, pp. 796–807, 1994.

[65] E. Casini, R. De Gaudenzi, and O. Del Rio Herrero, "Contention resolution diversity slotted aloha (crdsa): An enhanced random access schemefor satellite access packet networks," *IEEE Transactions on Wireless Communications*, vol. 6, no. 4, pp. 1408–1419, 2007.

[66] A. Emmanuele, F. Zanier, G. Boccolini, and M. Luise, "Spread-spectrum continuous-phase-modulated signals for satellite navigation," *IEEE Transactions on Aerospace and Electronic Systems*, vol. 48, no. 4, pp. 3234–3249, 2012.

[67] O. Kodheli, N. Maturo, S. Chatzinotas, S. Andrenacci, and F. Zimmer, "Nb-iot via leo satellites: An efficient resource allocation strategy for uplink data transmission," *IEEE Internet of Things Journal*, vol. 9, no. 7, pp. 5094–5107, 2022.

[68] O. Kodheli, S. Andrenacci, N. Maturo, S. Chatzinotas, and F. Zimmer, "Resource allocation approach for differential doppler reduction in nb-iot over leo satellite," in *2018 9th Advanced Satellite Multimedia Systems Conference and the 15th Signal Processing for Space Communications Workshop (ASMS/SPSC)*, 2018, pp. 1–8.

[69] M. A. Ullah, K. Mikhaylov, and H. Alves, "Analysis and simulation of lorawan lr-fhss for direct-to-satellite scenario," *IEEE Wireless Communications Letters*, vol. 11, no. 3, pp. 548–552, 2022.

[70] E. Hosseini and E. Perrins, "Timing, carrier, and frame synchronization of burst-mode cpm," *IEEE Transactions on Communications*, vol. 61, no. 12, pp. 5125–5138, 2013.

[71] P. Bianchi, P. Loubaton, and F. Sirven, "On the blind estimation of the parameters of continuous phase modulated signals," *IEEE Journal on Selected Areas in Communications*, vol. 23, no. 5, pp. 944–962, 2005.

[72] U. Raza, P. Kulkarni, and M. Sooriyabandara, "Low power wide area networks: An overview," *IEEE Communications Surveys Tutorials*, vol. 19, no. 2, pp. 855–873, 2017.

[73] M. Centenaro, L. Vangelista, A. Zanella, and M. Zorzi, "Long-range communications in unlicensed bands: the rising stars in the iot and smart city scenarios," *IEEE Wireless Communications*, vol. 23, no. 5, pp. 60–67, 2016.

[74] “Sigfox,” http://www.sigfox.fr, website.

[75] Semtech, “Lora modem design guide: Sx1272/3/6/7/8,” 2013.

[76] O. Seller and N. Sornin, “Low power long range transmitter,” *US Patent 20140219329 A*, 2014.

[77] U. Noreen, L. Clavier, and A. Bounceur, “Lora-like css-based phy layer, capture effect and serial interference cancellation,” in *European Wireless 2018; 24th European Wireless Conference*, 2018, pp. 1–6.

[78] M. Chen, Y. Miao, Y. Hao, and K. Hwang, “Narrow band internet of things,” *IEEE Access*, vol. 5, pp. 20 557–20 577, 2017.

[79] “3gpp. standardization of nb-iot completed,” http://www.3gpp.org/news-events/3gpp-news/1785-nb_iot_complete., press Communication 22 june 2016.

[80] “Gsma, carte de déploiement des réseaux nb-iot,” https://www.gsma.com/iot/deployment-map/#deployments, 2018.

COLLEGES SCIENCES
BRETAGNE POUR L'INGENIEUR
LOIRE ET LE NUMERIQUE

IMT Atlantique
Bretagne-Pays de la Loire
École Mines-Télécom

Titre : Détection non-cohérente des modulations à phase continue pour les communications IoT par satellite en orbite basse affectées par un décalage Doppler

Mot clés : Modulation à phase continue, effet Doppler, Internet des objets, Communications par satellite, Détection de séquence non-cohérente, Détection differentielle

Résumé : S'appuyant sur des réseaux de communication, l'Internet des objets (IoT) permet d'interconnecter des objets, parmi lesquels un nombre croissant d'appareils, autonomes en énergie et pauvres en ressources matérielles. Leur accès au réseau nécessite une connexion radiofréquence à un concentrateur de données. Dans les zones où il est difficile d'installer des infrastructures au sol, les constellations de satellites à basse altitude (LEO) offrent une solution. Les modulations à phase continue (CPM) semblent alors pertinentes pour le lien de communication entre les objets et le satellite. Dans cette thèse, nous développons des récepteurs CPM non-cohérents et robustes au décalage Doppler qui affecte sévèrement les communications par satellites LEO. Nous commençons par proposer deux détecteurs basés sur le critère optimal de réception non-cohérente et incluant une estimation du décalage Doppler sans symbole pilote à l'aide de la technique de *per survivor processing* (PSP). Les taux d'erreur simulés montrent leur robustesse vis-à-vis de décalages Doppler de l'ordre de ceux rencontrés pour les constellations LEO. Cependant, leur complexité reste importante pour une embarcation à bord de satellites LEO restreints à de faibles charges utiles. C'est pourquoi nous étudions ensuite un détecteur différentiel, sans estimation préalable du décalage Doppler. Son signal d'entrée est le produit du signal reçu avec sa version décalée temporellement. Notre optimisation du décalage temporel basée sur un critère de distance minimale, appliquée à différents formats CPM, permet une diminution significative du taux d'erreur par rapport à la référence (décalage d'une durée symbole). Ses performances (taux d'erreur, complexité, robustesse au décalage Doppler) montrent sa pertinence pour un récepteur bord.

Title: Non-Coherent Detection of Continuous Phase Modulation for Low Earth Orbit Satellite IoT Communications affected by Doppler Shift

Keywords: Continuous Phase Modulation, Doppler effect , Internet of Things, Satellite communications, Non-coherent sequence detection, Differential detection

Abstract: Based on communication networks, the Internet of Things (IoT) enables the interconnection of objects, including a growing number of devices, which are energy autonomous and have limited hardware resources. Their access to the network requires a radio frequency connection to a data hub. In areas where it is difficult to install ground infrastructure, low orbit satellite constellations (LEO) offer a solution. Continuous phase modulations (CPM) seem to be relevant for the communication link between the objects and the satellite. In this thesis, we develop CPM receivers that are non-coherent and robust to the Doppler shift that severely affects LEO satellite communications. We first propose two detectors based on the optimal criterion of non-coherent reception and including an estimation of the Doppler shift without pilot symbol using the technique of *per survivor processing* (PSP). The simulated error rates show their robustness with respect to Doppler shifts of the order of those encountered in LEO constellations. However, their complexity remains important for a launch on board LEO satellites restricted to small payloads. This is why we then study a differential detector, without prior estimation of the Doppler shift. Its input signal is the product of the received signal with its time-shifted version. Our optimization of the time shift based on a minimum distance criterion, applied to different CPM formats, allows a significant reduction of the error rate compared to the reference (shift of one symbol duration). Its performances (error rate, complexity, robustness to Doppler shift) show its relevance for an on-board receiver.